UNIVERSITY OF CALIFORNIA
RIVERSIDE

Exploring Coherent Spin Dynamics in Insulating Antiferromagnetic Systems

A Dissertation submitted in partial satisfaction
of the requirements for the degree of

Doctor of Philosophy

in

Physics

by

Shirash Regmi

September 2024

Dissertation Committee:

Dr. Igor Barsukov, Chairperson
Dr. Jing Shi
Dr. Shan-Wen Tsai

The Dissertation of Shirash Regmi is approved:

Committee Chairperson

University of California, Riverside

Acknowledgments

Graduate school has been both challenging and incredibly fulfilling. It's been a time of personal growth, forging friendships, and seizing countless learning opportunities. None of this would have been possible without the persistent support of the people who stood by me throughout this journey.

I want to extend my deepest thanks to my advisor, Prof. Igor Barsukov. His steadfast support, invaluable guidance, and insightful feedback have been instrumental in my academic and personal growth. His genuine commitment to his students' success speaks volumes about his character and dedication. I feel fortunate to have had him as my advisor, and I'll always cherish the profound impact he's had on my life.

I would also like to thank Prof. Jing Shi and Prof. Shan-Wen Tsai for serving in my defense committee, and for the time and effort in reviewing my dissertation.

I want to thank Dr. Bassim Arkook, who was my mentor during my initial days in the lab. His patient teaching and guidance in measurement and data analysis were invaluable to me.

I'd like to extend my gratitude to Dr. Arezoo Etesamirad, Rodolfo Rodriguez, Rundong Jiang and Alexandra (Sasha) Korotneva for creating a supportive and collaborative work environment. Their technical expertise and shared enthusiasm for our research have made my time here both productive and enjoyable.

I would also like to thank my other labmates: Allison Tossounian, Sarah Sabawi, Audrey Ng, Trevin Lee, Alex Hernandez, Jenika Santiago, Travis Crumpton, Eric Hagen,

Henry Woodington, Joshua Bocanegra, and Diego Camacho for their resourceful presence in the lab and the interesting projects we shared to work on.

The past six years in Riverside have been incredibly meaningful, shaping me both academically and personally. First and foremost, I want to express my deepest gratitude to my parents, Hari Prasad Regmi and Sita Regmi. Their unwavering love and support have been my anchor, especially during the toughest times in my academic journey. Even though we're miles apart, I carry your love and support with me always. Thank you, mom and dad, for everything. Next, a special thanks to my brother, Shikhar Regmi. I'm grateful to have you in my life, always offering your love and encouragement, no matter how small it might seem.

Finally, a big thank you to my wife, Pratikshya. Your support and encouragement have been crucial during my PhD journey. Your understanding and patience mean the world to me, and I'm truly grateful for everything. I couldn't have reached this milestone without you by my side. I love you!

In the love of Physics.

ABSTRACT OF THE DISSERTATION

Exploring Coherent Spin Dynamics in Insulating Antiferromagnetic Systems

by

Shirash Regmi

Doctor of Philosophy, Graduate Program in Physics
University of California, Riverside, September 2024
Dr. Igor Barsukov, Chairperson

Spin-based electronics or spintronics bear the potential to become an alternative paradigm to the traditional transistor-based electronics that is currently facing significant challenges related to energy efficiency, heat management and speed limitations. Understanding spin dynamics is essential for functionalizing spintronic devices. Frequency of operation of spintronic devices is in the range of GHz for ferromagnetic (FM) systems, and potentially THz for anti-ferromagnetic (AFM) systems.

A segment of my research examines bilayer nanostructures comprising YIG and Ni for potential application in energy-efficient spintronic devices. Microwave emission spectroscopy performed on these hybrid magnetic nanodevices in perpendicular geometry showed the presence of auto-oscillatory mode driven by the spin-Seebeck effect – an effect that re-uses waste heat in the nanodevice to operate it. We further observed a substantial non-linear frequency shift at low magnetic fields. This work establishes a proof of concept for utilizing spin-based mechanisms in the pursuit of energy-efficient spintronics solutions.

To push the boundaries of spin-based applications, AFM have been proposed. AFM operates in sub-terahertz to terahertz frequency range compared to FM at gigahertz frequency range. AFMs are also robust to external magnetic perturbations because of their zero net magnetization. In this dissertation, I translate the techniques and knowledge from FM systems to AFM systems and study the coherent spin dynamics in the bulk insulating antiferromagnetic systems. The magneto-resistive (MR) method is used to detect antiferromagnetic resonance (AFMR) in bulk Cr2O3 and Pt micro-structure device of size $10\,\mu\text{m} \times 200\,\mu\text{m}$. The successful detection of MR-AFMR set up the path to dive into the nanoscale AFM system. We achieved electrical detection of antiferromagnetic resonance signal in a nanodevice of dimension $200\,\text{nm} \times 200\,\text{nm}$. Additionally, we are also able to electrically detect the AFMR signal in Fe2O3/Pt AFM system. The analysis of the study of the AFMR signal and the angle between the microwave current flow and the c-axis of the anti-ferromagnetic device suggest that the resonance signal is dominated by the spin-torque excitation rather than inductive/Oersted excitation. The results of this work pave the road toward nanoscale AFM spin-torque devices and applications.

As a prospect, we evaluate an alternative approach that relies on inductive excitation of AFM spin dynamics but is less restrictive to the miniaturized device size. We propose and develop integration of omega-shaped planar micro-resonator with micro-scale AFM structures. This work explores alternative pathways for hybrid AFM-superconductor systems and will broaden the experimental palette for the studies of AFM spin dynamics.

Contents

List of Figures

Chapter 1

Introduction

1.1 Motivation

The overarching theme of this dissertation is to explore the physical phenomena that may lead to next generation spin-based computation devices [1, 2]. Conventional computational electronics are based on transistors, which face challenges related to energy efficiency due to energy loss from moving charges. Additionally, transistor operation speeds are limited by band-structure and interfacial effects in semiconductor materials, as well as inherent impedance problems.

On the other hand, spin dynamics is an inherently low energy and low dissipation phenomenon. Thus, spin dynamics is energy efficient and reduces heat management issue which is one of the bottleneck in conventional electronics. Furthermore, the frequency of operation of spin based devices is in the range of GHz for ferromagnetic (FM) systems, and potentially THz for anti-ferromagnetic (AFM) systems. Spin based devices are potentially more versatile because of the rich, partially yet to explore physical phenomena.

Spin based devices have the potential for unconventional computation schemes beyond the binary logic operations. For examples, information transported by spin waves can be encoded through multiple parameters of the spin wave such as frequency, amplitude, phase, as well as time domain parameter like modulation. There have been experimental realizations of reservoir computing with spin based systems by using metastable spin states under thermal fluctuations [3, 4, 5]. In addition, spin based neural networks based on magnetic microscale devices have also been experimentally realized [6, 7]. These proofs of principle give direction for the advancement of computational technology via spin based route in the foreseeable future. Furthermore, recent theoretical and experimental works on spin based quantum computation using magnetic materials reveal the potential of magnet based quantum information system [8, 9].

The advancement of spin-based computation technologies would benefit greatly from the exploration of spin dependent physical phenomena that can lead to the development of hybrid magnetic devices. These devices could leverage the efficiency of thermal spin current injection, a promising approach to address the energy consumption challenges faced by conventional electronics. Furthermore, transferring expertise and ideas from ferromagnetic spintronics to antiferromagnetic systems is crucial for expanding the scope and capabilities of spin-based technologies, potentially unlocking new avenues for innovation and breakthroughs in the field. With recent advancements in both understanding and experimental methods, I would like to tackle some of the research topics.

To study energy efficiency, I develop the hybrid magnetic device of ferri/ferro magnetic system. Using microwave emission spectroscopy, I demonstrate a thermal spin

current driven oscillator, showing the potential for waste heat management & recycling in conventional ferromagnetic spintronics. On the other hand, I extend the ideas of ferromagnetic spintronics to antiferromagnetic systems. I devise, design, and fabricate an antiferromagnetic spintronics system to study the coherent spin dynamics. I employ the electrical detection technique which is crucial for advancing towards nanoscale antiferromagnetic spintronics. This sets the groundwork towards ultra-fast spintronics applications based on antiferromagnetic systems. In addition, I also set the preliminary work to study spin dynamics in antiferromagnet using the planar micro-resonators. This parallel approach might become useful to potentially allow for exploration of AFM magnon coupling with the superconducting circuitry of quantum information systems.

1.2 Outline

This dissertation is structured as follows:

Chapter 2 discusses the background relevant to this dissertation.

Chapter 3 explores a hybrid device consisting of a nanoscale bilayer of a ferri/-ferromagnetic systems. Using microwave emission spectroscopy, I detect thermally driven auto-oscillation in a perpendicular geometry. This result is particularly important from the standpoint of energy efficiency because the device effectively harnesses waste heat to induce a persistent oscillations.

Chapter 4 discusses the development of a novel spectrometer designed for magnetic resonance at low temperatures and high magnetic fields. The probe is specifically tailored for microwave spectroscopy measurements of antiferromagnetic systems. The devel-

opment of this probe progresses in multiple stages, utilizing both machined and 3D-printed components. Careful design considerations were made to ensure the probe can withstand thermal stress at extremely low temperatures. Through testing with control samples, we confirm the probe's effectiveness, paving the way for future studies on spectroscopy of antiferromagnetic systems.

Chapter 5 focuses on antiferromagnet-based systems, which are gaining attention due to their spin dynamics in the THz regime, promising ultrafast operational speeds for spintronics applications. Additionally, the zero magnetic moment characteristic of antiferromagnets offers robust protection against external magnetic disturbances. Transferring the ideas from ferromagnetic system to antiferromagnetic system, I investigate the coherent spin dynamics in microscale antiferromagnetic system using magnetoresistive methods. The successful electrical detection paves the way for exploring spin dynamics at the nanoscale, advancing towards practical applications of antiferromagnetic systems. Ultimately, I detect the antiferromagnetic resonance signal in a nanocross device.

Chapter 6 introduces preliminary work aimed at measuring antiferromagnetic spin dynamics using an omega-shaped planar micro-resonator. While antiferromagnetic thin films typically exhibit limited magnetic moment dynamics, the planar omega resonator offers an innovative approach to enhance inductive detection capabilities for antiferromagnetic resonance. Our initial work will involve integrating antiferromagnetic micro-structures onto the resonator and utilizing electrical circuitry for potential spin current biasing. This chapter outlines the experimental design, device fabrication, omega shaped micro-resonator fabrication, and device-resonator integration as foundational steps. Upon successful vali-

dation, we aim to explore the cavitronic effects through the hybridization of magnons and photons using superconducting planar resonators.

Chapter 7 This chapter is a summary of the dissertation.

Chapter 2

Background

An electron's spin is a fundamental quantum property and a type of angular momentum. The flow of angular momentum in a material without net charge transport generates a spin current [10, 11]. Among the mechanisms driving spin current generation, the spin Hall effect stands out prominently. In the spin Hall effect, an electric current induces a transverse spin current due to spin-orbit coupling, a relativistic interaction between a particle's spin and its motion [12, 13]. Similarly, the anomalous Hall effect involves the spin-orbit coupling of electrons in magnetic materials, resulting in spin current generation [14, 15, 16]. Additionally, the spin Seebeck effect demonstrates that a temperature gradient across a magnetic material can induce a spin current [17, 18, 19]. Moreover, the inverse spin Hall effect provides a mechanism to convert this spin current back into charge current [20, 21, 22].

In a distinct avenue of spin-charge based phenomena, magnetoresistance, spin pumping and spin transfer torque play crucial roles. Magnetoresistance describes the dependence of the electrical resistance of a magnetic system on the direction of its magneti-

zation with respect to the direction of current flow [23]. Thus, magnetoresistance provides a convenient method to access both static and dynamic magnetization (or more generally order parameter) in the magnetic system. Spin pumping involves the injection of spin angular momentum from a magnetic material into an adjacent material [24, 25, 26]. Spin torque refers to the transfer of angular momentum into the magnetic layers and its subsequent interaction with magnetization [27, 28]. This transferred angular momentum into the magnetic layer interacts with the spins in the magnetic layer that can drive the spin precession or spin wave dynamics [29]. All mechanisms are integral to understanding and manipulating spin dynamics and spin charge based phenomena.

I will briefly review magnetic systems as they will be essential for understanding the intricate behaviors and interactions within spin-based phenomena. Additionally, I will review the concepts of spin waves – also known as magnons and the magnetization dynamics, as these topics form the foundational basis of this dissertation.

2.1 Magnetic system

A ferromagnetic material possesses the ability to be magnetized or generate a magnetic field. At the atomic level, these materials exhibit magnetic moments due to the intrinsic spin and orbital motion of electrons. Generally, the alignment of these magnetic moments give rise to various magnetic behaviors, such as paramagnetic, ferromagnetic, ferrimagnetic, and antiferromagnetic. Magnetic materials undergo phase transitions between different magnetic phases. Such transitions are characterized by specific critical temperatures. Below these critical temperatures, the material demonstrates spontaneous

magnetization, where the magnetic moments align in a ground state configuration. In the subsequent sections, we will discuss some of the key magnetic ground states pertinent to this dissertation.

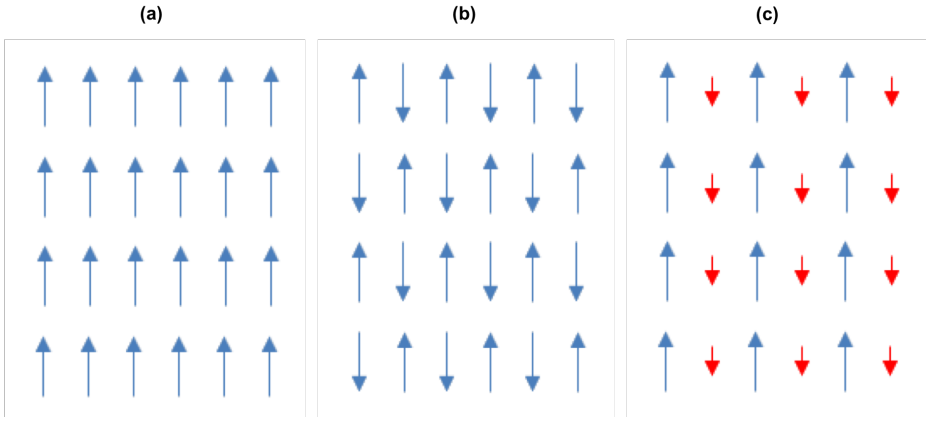

Figure 2.1: A simplified schematic of the magnetic ground states on a 2-dimensional plane. (a) Ferromagnetic ground state. All the magnetic moments are parallel. (b) Antiferromagnetic ground state. The neighboring magnetic moments align anti-parallel to one another resulting in a zero net magnetization. (c) Ferrimagnetic ground state. The net magnetic moment isn't zero.

2.1.1 Ferromagnetism

Figure 2.1 (a) is a ground state configuration of a ferromagnet. A ferromagnet has a spontaneous magnetization even in the absence of an applied external magnetic field. All the magnetic moments align parallel and form the ground state configuration. This effect is due to the exchange interaction between the neighboring spins of electrons. A material is ferromagnetic below the Curie temperature. Iron, cobalt, nickel, permalloy are some of the ferromagnetic materials.

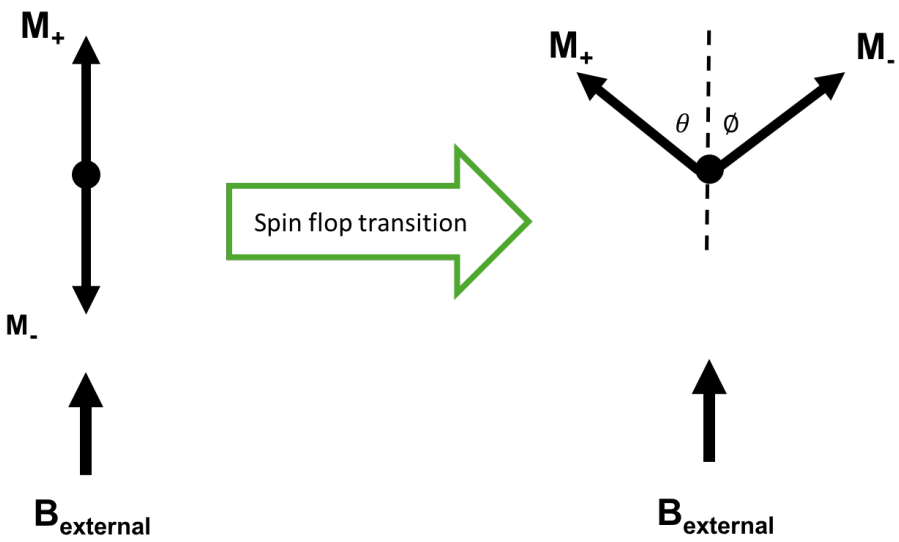

Figure 2.2: Adapted from [30]. A layout of spin flop transition in an antiferromagnet. At some threshold magnetic field, the magnetizations of two sub-lattices make a transition to the canted state known as spin-flop state.

2.1.2 Antiferromagnetism

Figure 2.1 (b) is a simplified ground state configuration of an antiferromagnet. In antiferromagnets, the neighboring spins of electrons align anti-parallel such that the net magnetization is zero. If the exchange interaction [31] between neighboring spins of electrons is negative, it is favorable for nearest neighbor magnetic moments in different atoms to be in anti-parallel state resulting in antiferromagnetism. Many antiferromagnetic system can be interpreted with two sub-lattices of opposite magnetization. Since the net magnetic moment is zero, the quantity known as staggered magnetization is defined in such system. Staggered magnetization is the difference of the magnetization in each sub-lattice. A material is antiferromagnetic below the Néel temperature (T_N).

In the case of magnetic field applied parallel to the magnetizations, an interesting case known as spin flop occurs at the critical field known as spin-flop field in easy-axis

antiferromagnets. At the spin-flop field, the system snaps into a different configuration as shown in Figure 2.2. This is known as spin-flop transition.

Some examples of antiferromagnets are: Cr_2O_3, $\alpha - Fe_2O_3$, MnF_2, MnO, NiO.

2.1.3 Ferrimagnetism

In ferrimagnets, the magnetization of two sub-lattices is not equal but it is opposite such that the material will have a net magnetization. Figure 2.1 (c) is the ground state configuration of a ferrimagnet. It looks similar to an antiferromagnet, but the two sub-lattices are not equivalent.

Some examples of ferrimagnets are: $Y_3Fe_5O_{12}$, Fe_3O_4, $NiFe_2O_4$.

2.2 Spin waves and magnon

Spin waves are collective excitation of electrons spins in a magnet [32, 33]. Instead of individual spins acting on their own, they work together in a coordinated way, causing these waves to propagate through the material without carrying any electric charge. This collective behavior makes spin waves a key player in how spin information moves around in magnetic materials.

Understanding spin waves and magnons is important in areas like spintronics and magnonics [34, 35]. These fields focus on using spin to process and store information. By studying how spin waves work, we could develop new ways to make better, more efficient spintronic devices, potentially leading to advancements in areas like computing and data storage [36].

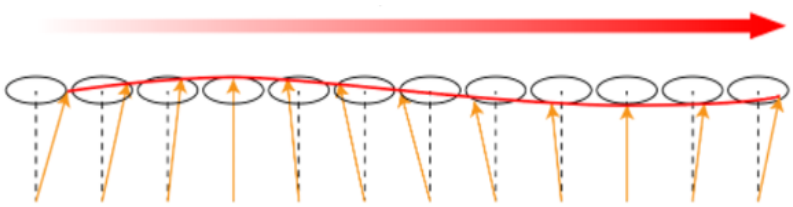

Figure 2.3: Schematic of a spin wave.

2.3 Magnetization dynamics

Magnetization dynamics refer to a process in which the local magnetization vector in a magnetic material evolves over time in response to any external stimulus or internal interaction. The magnetization vector typically precesses around an effective magnetic field [37]. This rotation can be influenced by means of external magnetic fields, spin currents, or thermal fluctuations, leading to various dynamic behaviors such as oscillations, domain wall motion, and magnetization reversal. Understanding the magnetization dynamics is crucial for predicting and controlling the behavior of magnetic materials in technological applications, from data storage to spintronic devices.

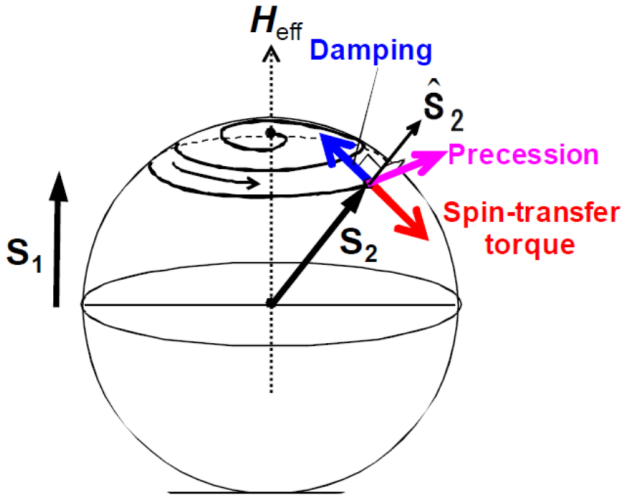

Figure 2.4: Adapted from [38]. Direction of torques presented in the magnetic system.

The study of magnetization dynamics encompasses a range of phenomena and mechanisms, including spin waves, spin transfer torque, and damping mechanisms. Spin wave is a collective excitation of electron spins that can propagate through the material, influencing the magnetization dynamics. Spin torque, on the other hand, refers to the transfer of angular momentum to magnetic layers, which can induce changes in the magnetization orientation and drive dynamic magnetic behaviors. Additionally, damping mechanisms play a role in dissipating the energy of magnetization dynamics, affecting the stability and lifetime of dynamic magnetic states. Together, these elements form the foundation for understanding and manipulating magnetization dynamics in magnetic materials and systems.

The magnetization dynamics in the presence of spin transfer torque can be described by Landau-Lifshitz-Gilbert equation [39, 40, 41] including an extra term for the spin torque (Slonczewski term) [42]:

$$\frac{d\mathbf{m}}{dt} = \gamma(\mathbf{H_{eff}} \times \mathbf{m}) + \alpha\mathbf{m} \times \frac{d\mathbf{m}}{dt} + J_{eff}(\mathbf{m} \times (\mathbf{m} \times \sigma))$$

Where H_{eff} is the total effective field, α is the damping constant, σ is the polarization of the incident spin current, and m is the normalized magnetization. The first term describes the precessional motion of magnetization m which is called field torque. The second term is the damping torque which characterizes the energy dissipation. It points toward the equilibrium direction of the magnetization, so that the magnetization tends to relax back to the equilibrium. The third term is spin-transfer torque. If the polarization of the spin current is parallel to the equilibrium magnetization then it exerts an anti-damping spin torque (Slonczewski-torque). It effectively reduces the damping of the system. The effects of this damping reduction can be categorized into three types: damping, switching and auto-oscillations as shown in Figure 2.5.

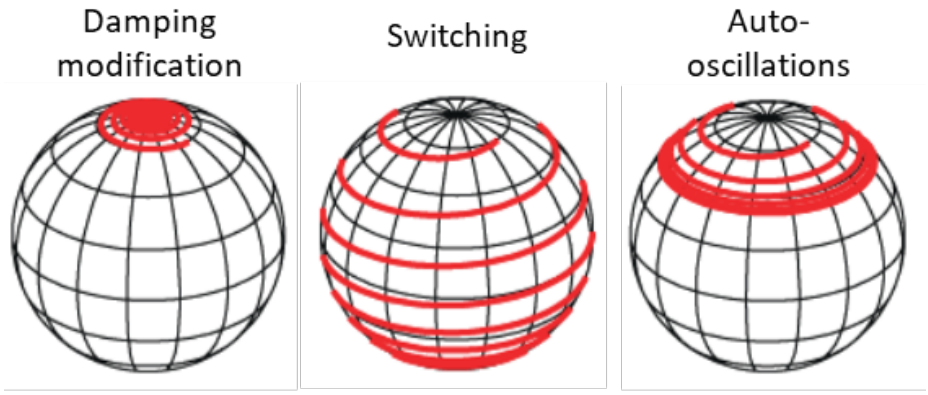

Figure 2.5: Adapted from [28]. Spin torques leading to different configurations: Damping modification, triggering switching at high-damping current, and causing auto-oscillation at critical current.

Chapter 3

Auto-oscillations in two-magnet hybrid nanodevices

3.1 Introduction and motivation

Spin torque driven spin dynamics [43] is an important functionality in the modern spintronic applications [44, 45, 46] such as spin-torque memory [47, 48, 49] and spin-torque oscillators [50, 51]. Spin torque memory is a non-volatile magnetic memory device that has the potential to become an extremely high-performance memory. Spin torque oscillators are used in microwave assisted magnetic recording and as neurons in magnetic neural networks [52]. For neuromorphic computing it is important to develop spin torque oscillators with strong and tunable nonlinearities [53].

There are several instances when the spin-torque driven auto-oscillations have been realized [51, 54, 55, 56]. Figure 3.1 (a) is a system of bilayer of ferrimagnetic insulator YIG

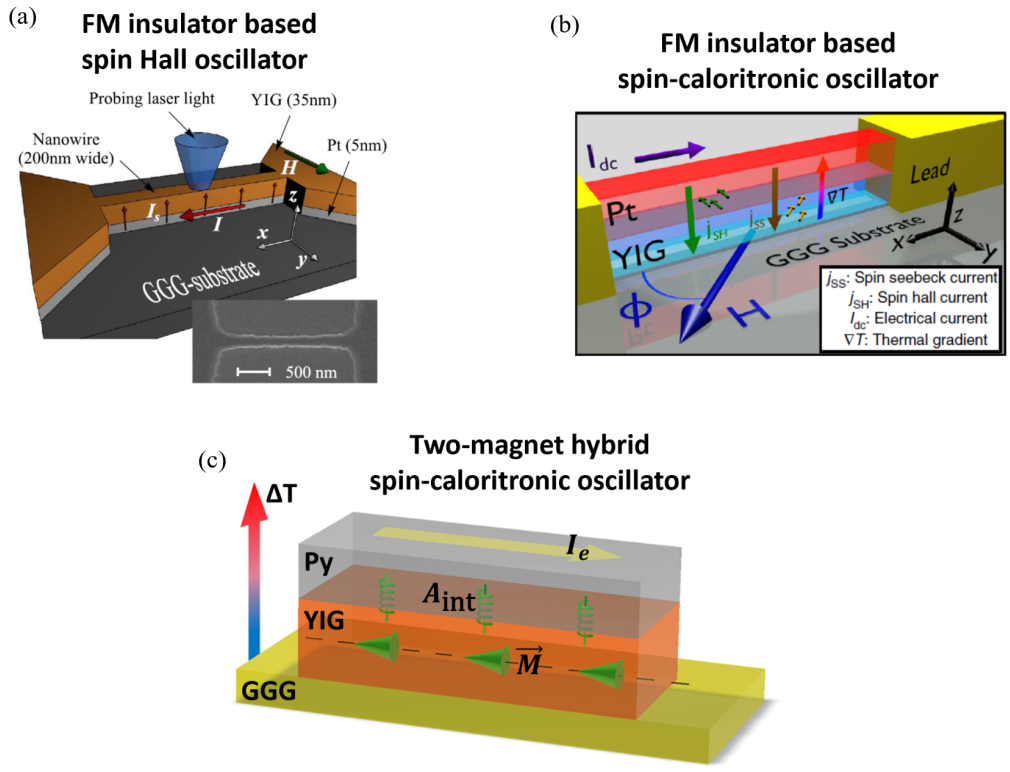

Figure 3.1: (a) Adapted from [54], Spin Hall effect driven spin torque oscillator in a bilayer system of YIG and Pt. The YIG layer sits on the top surface. (b) Adapted from [55], Spin Seebeck effect driven spin caloritronic oscillator in a bilayer system of Pt and YIG. The Pt layer sits on the top surface. (c) Adapted from [56], Spin Seebeck effect driven spin caloritronic oscillator in a bilayer system of YIG and Py. The Py layer sits on the top.

and a non-magnetic metal Pt. In this system, auto-oscillations have been shown by means of spin Hall effect in Pt [54]. Figure 3.1 (b) is a similar system as in Figure 3.1 (a), except this system has Pt layer on the top instead of YIG layer as in 3.1 (a). In this system as well, the auto oscillatory modes have been shown. However, in this system the auto-oscillations are driven by spin Seebeck torque. This result is particularly important because the waste heat is being recycled that opens the door to achieve energy efficiency [55]. Figure 3.1 (c) is a bilayer hybrid system of ferrimagnet YIG and ferromagnet Py. In this system also the

spin Seebeck torque driven auto oscillations have been shown [56]. In this chapter, I would like to show our hybrid system of YIG and Ni as a spin torque oscillator. This architecture may increase the functionality and performance, and open up the avenues for new physics.

We systematically perform the magnetoresistance (MR), spin torque ferromagnetic resonance (ST-FMR), and microwave emission spectroscopy experiments. But first, I would like to introduce the materials and nano-fabrication procedures.

3.2 Materials of choice and nano-fabrication procedure

3.2.1 Introduction to materials

For this experiment, our choice of materials is Yttrium Iron Garnet ($Y_3Fe_5O_{12}$ or YIG) and Nickel (Ni). YIG is a ferrimagnetic insulator that has a Curie temperature of about 560 K and an extremely low magnetic damping in the order of about 10^{-5} range [57, 58, 59, 60]. Nickel is an elemental ferromagnetic metal. It has a Curie temperature of about 628 K. The substrate used for the device preparation is Gadolinium Gallium Garnet ($Gd_3Ga_5O_{12}$ or GGG) with (111) surface orientation.

3.2.2 Nanodevice fabrication

The nanodevices are fabricated through a multi-step process:

The YIG thin films were provided by Prof. Jing Shi's group. The growth of YIG of about 20 nm was carried out on a single crystal substrate GGG (111 surface orientation) using pulsed laser deposition technique [61, 62, 63]. After the YIG deposition [64], annealing

procedure was performed at around 820 °C. We can see the great crystallographic and epitaxial order in the transmission electron microscopy (TEM) image in Figure 3.2 (a) for the GGG/YIG interface.

This step was followed by the deposition of 5 nm of Ni on top of the YIG film in the room temperature setup. The deposition was done using RF magnetron sputtering with 4 mTorr of Argon gas pressure, and 10^{-7} Torr system pressure. The growth rate of Ni is about 0.6 Å/s at 75 Watts DC power. Then the Ni was capped with a thin layer (2 nm) of Aluminum oxide to prevent oxidation of Ni.

As a next step the device structure was patterned on the surface. The fabrication of the nanodevices was carried out using the electron beam lithography (EBL). After the thorough cleaning of the specimen with acetone and isopropanol, the YIG/Ni bilayer film was first coated with the negative resist MAN-2401 of around 100 nm thickness. The spin coating was performed at the rate of 3500 rpm for 45 seconds. The resist was soft baked on a hot plate for 1 minute at 90 °C.

The resist was patterned into nanowires and leads using EBL with the nanometer pattern generation system (NPGS) software. The typical write current was 15 pA and area dose of about 200 - 300 μC/cm^2. The center to center distance and line spacing were set to 1 nm. After the EBL writing, the developer (maD-525) was applied for 60 sec, and the sample was rinsed with HPLC water for 3 min.

After defining the patterns, the sample was ion-milled at an incident angle of 65 deg for several minutes (according to calibration such that YIG/FM material is etched down to the substrate: YIG etching rate was 3.7 nm/min). Duty-cycling and water cooling

of the sample was used during the ion milling to prevent the sample from overheating. The remaining resist was removed using sonication in acetone.

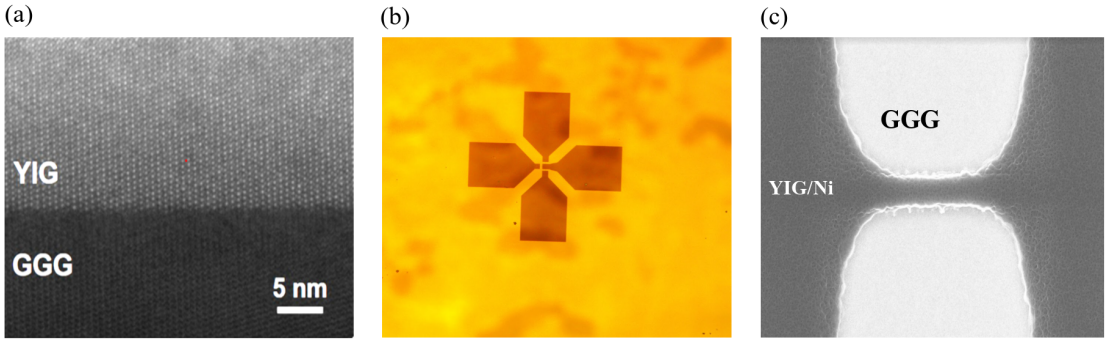

Figure 3.2: (a) Transmission electron microscopy image showing the crystallographic and epitaxial order of the GGG and YIG interphase. (b) Optical microscopy image of the YIG/Ni bilayer device system. There are three nanowires in the picture. (c) Scanning electron microscopy image of a single YIG/Ni nanowire's active region. The dark shade is the nanowire active region. The bright shade is the GGG substrate.

Figure 3.2 (b) shows the microscopy image of the device, and Figure 3.2 (c) shows the scanning electron microscopy image of the active region of the device. The developed device is a nanowire. There are two sizes of the device: $900\,\text{nm} \times 4\,\mu\text{m}$ and $900\,\text{nm} \times 7\,\mu\text{m}$.

3.3 Magnetoresistance (MR) measurement

The change in resistance of a material under an applied magnetic field is known as magnetoresistance (MR) [23]. In ferromagnetic metals, the resistance depends on the direction of its magnetization with respect to the direction of electric current flow in the material. This effect is known as anisotropic magnetoresistance (AMR) [65]. The magnetoresistance phenomenon provides a convenient method to access the magnetization vector in a magnetic

system. This method can be employed for read out of both static magnetization and spin dynamics [66]. In this section, I present the systematic study of the magneto-transport phenomenon in the parallel and perpendicular directions of applied magnetic field with respect to the plane of the device.

3.3.1 Magnetoresistance with in-plane magnetic field

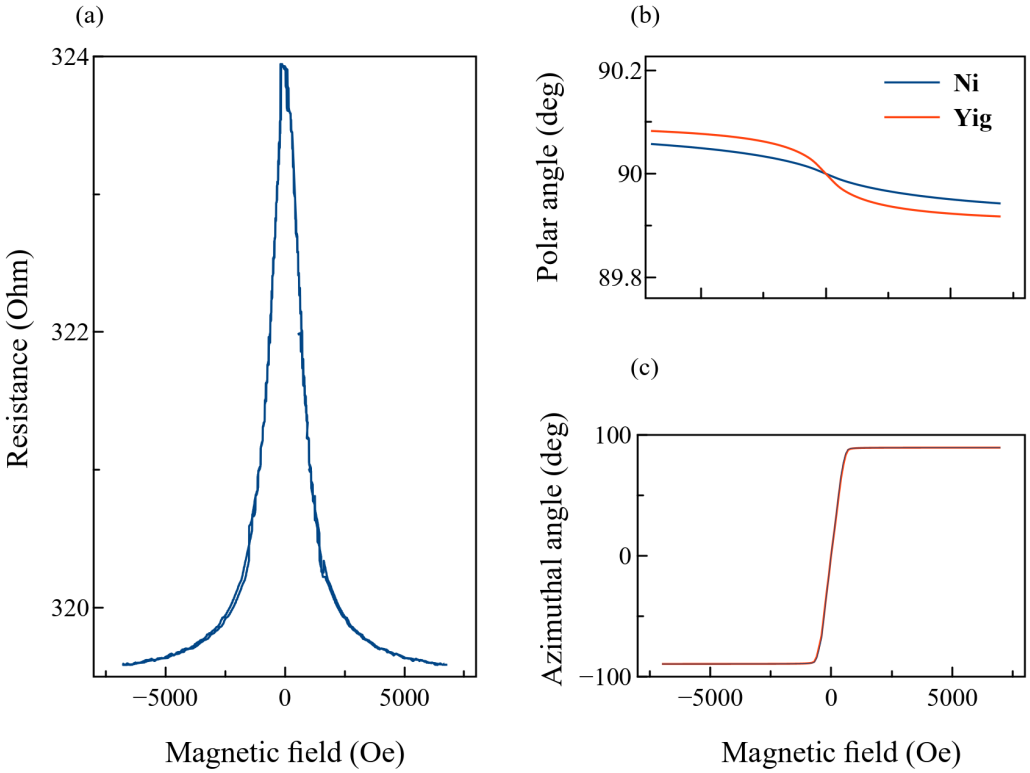

Figure 3.3: (a) The experimental result of the magnetoresistance measurment of a YIG/Ni bilayer nanowire when external magnetic field is applied in the device plane but transverse to the nanowrie axis. (b) The micromagnetic simulated result for the nanowire. It shows the polar angle dependence of magnetization as a function of applied external magnetic field. The blue curve is the magnetization of Ni and the red curve is the magnetization of YIG. (c) The micromagnetic simulated result for the nanowire. It shows the azimuthal angle dependence of magnetization as a function of applied external magnetic field. The blue curve is the magnetization of Ni and the red curve is the magnetization of YIG.

We apply a magnetic field within the plane of the device but transverse to the nanowire axis. The field is swept from -6000 Oersted to +6000 Oersted. Figure 3.3 (a) is the resistance of a device as a function of the applied external magnetic field. We observe that there is a decrease in the resistance as the external magnetic field increases, which is

consistent with the anisotropic magneto-resistance (AMR) of a Ni [65, 67, 68]. If we consider ϕ to be the angle between magnetization and electric current direction, the AMR can be written as:

$$\rho_{\mathrm{xx}}(\phi) = \rho_{\mathrm{para}} + (\rho_{\mathrm{para}} - \rho_{\mathrm{perp}}) \cdot \cos^2(\phi)$$

where the variation of the longitudinal resistivity ρ_{xx} is called the anisotropic magnetoresistance as a function of the angle ϕ. The ρ_{para}, and ρ_{perp} are the resistivities for $\phi = 0$ and 90 deg respectively.

Alongside the experiment, we also run the micromagnetic simulations based on finite element approach. The simulations are carried out using MuMax^3 [69] software package that shall be discussed in section 3.4.3 in detail. The simulation results presented in Figure 3.3 (b), (c) are also consistent with the experimental result. We observe similar behavior of magnetoresistance in both cases. This may be coming mostly from the shape anisotropy of the nano-wire. In addition we see some jumps like behavior, which look like Barkhausen-like noise, and which is not consistent with the uniform coupling of the layers.

3.3.2 Magnetoresistance with out-of-plane magnetic field

We run the measurements with magnetic field out of the device plane. In Figure 3.4 (a), we again see the behavior that is consistent with the anisotropic magnetoresistance. However, in this case we need a larger field to saturate the magnetization of Ni to out-of-plane. We also perform the micromagnetic simulation. We see the saturation behavior of YIG and Ni in the simulated Figure 3.4 (b), (c). At the intermediate fields, we see the

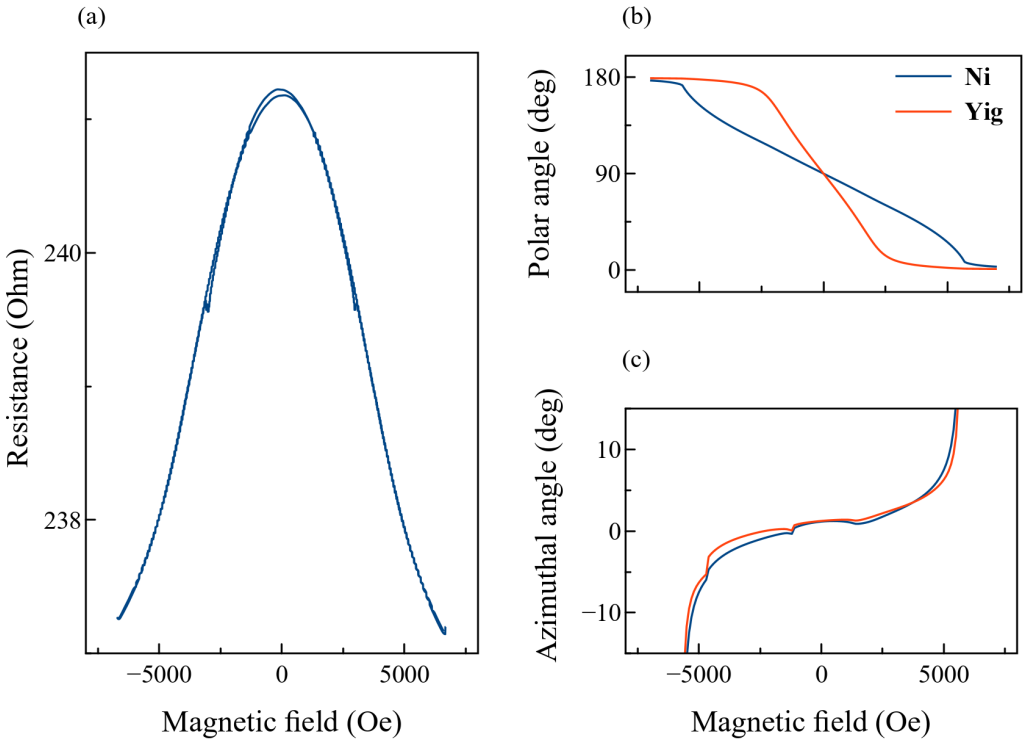

Figure 3.4: (a) The experimental result of the magnetoresistance measurment of a YIG/Ni bilayer nanowire when external magnetic field is applied perpendicular to the device plane. (b) The micromagnetic simulated result for the nanowire. It shows the polar angle dependence of magnetization as a function of applied external magnetic field. The blue curve is the magnetization of Ni and the red curve is the magnetization of YIG. (c) The micromagnetic simulated result for the nanowire. It shows the azimuthal angle dependence of magnetization as a function of applied external magnetic field. The blue curve is the magnetization of Ni and the red curve is the magnetization of YIG.

snapping of YIG magnetization that is partially reproduced in the micromagnetic simulation as well. Based on the experimental results and the micromagnetic simulations that we have run, we can conclude that there is a non-uniform interlayer exchange coupling between the YIG and nickel that goes beyond the dipolar coupling in this nano-structure.

3.4 Magnon Spectroscopy

We explore magnon modes in our YIG/Ni bi-layer nano-structure. Here we observe the spin torque ferromagnetic resonance (ST-FMR) [70, 71, 72] responses as a function of applied microwave and external magnetic field. We use the microwave signal generator to source the driving current at microwave frequency. Besides the generation of oscillating Oersted field, the microwave current also generates the spin current in a transverse direction to the flow of microwave current and the spin polarization of microwave current carriers. The spin current is then transferred across the interphase of Ni and YIG. These transferred spins act as a torque and generates the coherent magnetization precession at the GHz frequency. Magnetization precession in response to such excitation leads to resistance oscillations due to the magnetoresistive effects. Since both the current and resistance oscillations are at the same microwave frequencies, they can mix and result in a rectified voltage. This voltage is proportional to the resistance oscillations and thus to the oscillations of the magnetization (or more generally magnetic order). In addition to this so-called photovoltage effect, another effect exists – photoresistance refers to difference of the sample resistance in and out of the resonance due to the magnetoresistance under a DC current.

$$\mathrm{V_{photovoltage}} = \langle \mathrm{I(t)} \cdot \mathrm{R}(\mathbf{M}(\mathrm{t}))\rangle \propto \langle \mathrm{I_0 R_0} \cos(\omega \mathrm{t}) \cos(\omega \mathrm{t} + \eta)\rangle_t$$

$$\mathrm{V_{photoresistance}} = \langle \mathrm{I_{DC}} \cdot [\mathrm{R}(\mathbf{M}(\mathrm{t}))_{(\mathrm{in-resonance})} - \mathrm{R}(\mathbf{M}(\mathrm{t}))_{(\mathrm{out-of-resonance})}]\rangle_t$$

Here, we present the study done on different configurations of external magnetic field vs the device axis.

The schematic for the ST-FMR experimental setup is presented in Figure 3.5 [73]. Microwave generator generates the high frequency current that travels through the microwave cables to the device under test. Bias-tee is used to separate high and low frequency signals that come out of the device. Low frequency signals are collected in the lock-in amplifier. We use the field-modulation technique to modulate the magnetic field at a small frequency [74]. The modulation frequency is used as a reference frequency for the lock-in amplifier.

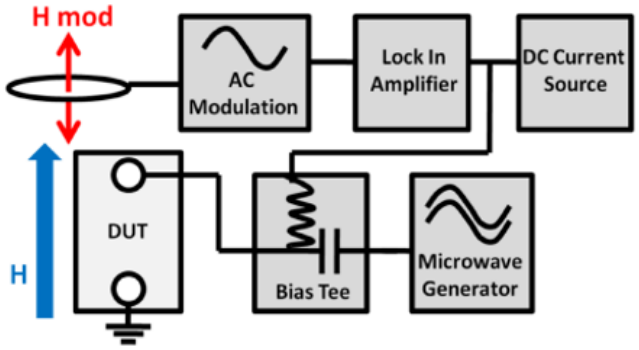

Figure 3.5: Adapted from Ref. [73]. Schematic representation of a spin torque ferromagnetic resonance (ST-FMR) measurement setup. A magnetic device or device under test (DUT) is wire-bonded to the coplanar waveguide (CPW) and sits in between the pole pieces of electromagnet. The CPW board is designed to include a SMA connector, which is connected to the microwave generator and a DC current source via the microwave port of the bias-tee. This setup implements the use of magnetic field modulation.

3.4.1 Magnon spectroscopy with in-plane magnetic field

The magnetic field is applied in the transverse direction of the nanowire device that sits on the plane of the substrate. The measurement is done at zero direct current. We observe that the spin waves emerge from about 2 GHz. The rectified voltage disappears at about 1 kOe. From MR plot in Figure 3.3, this is approximately the region where YIG

magnetization starts to saturate along the direction of the external magnetic field. We only observe the modes where YIG is continuously saturating.

Now we carry out the same measurement but in the presence of a finite direct current. In this case, the ST-FMR signal consists of both rectified voltage and photo-resistance. However, the photo-resistance contribution does not allow us to observe the signal beyond 1 kOe magnetic field. This observation is quite unusual and different from the previously done study on the hybrid magnetic system of YIG/Py bilayer nanostructure [56].

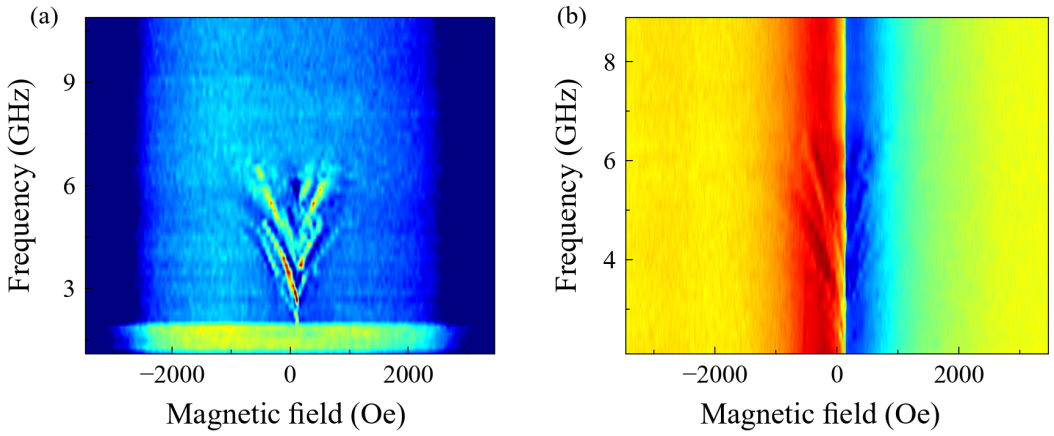

Figure 3.6: Color plot of ST-FMR measurement in a YIG/Ni bilayer nanowire at 77 K. The external magnetic field is applied in the device plane and transverse to the device axis. (a) with zero direct bias current, (b) with finite direct current bias.

3.4.2 Magnon spectroscopy with out-of-plane magnetic field

We apply the magnetic field perpendicular to the nanowire device plane. We observe multiple modes. However, the signal is very weak. Now we change the direction of the field sweep. Comparing both of the directions' sweep results, hysteretic-like behavior is

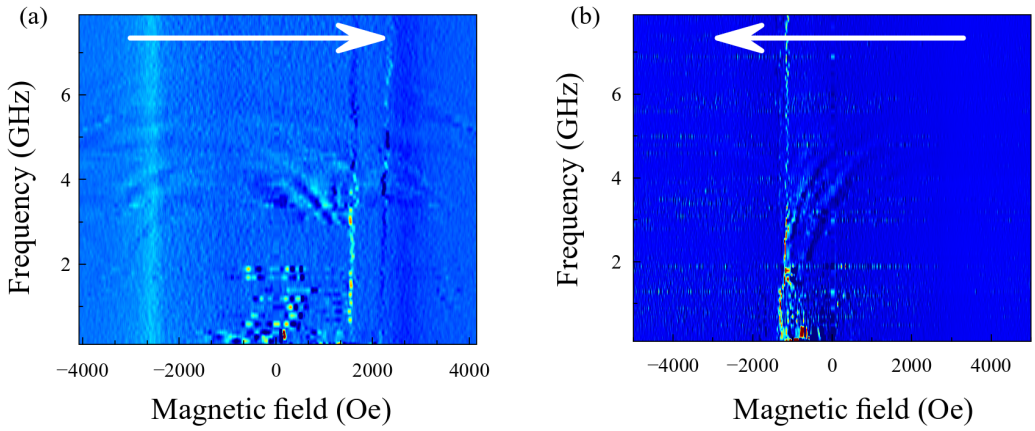

Figure 3.7: Color plot of ST-FMR measurement in a YIG/Ni bilayer nanowire at 77 K and zero direct bias current. The external magnetic field is applied perpendicular to the device plane. (a) External magnetic field swept from -4000 Oe to +4000 Oe. (b) External magnetic field swept from +4000 Oe to -4000 Oe.

observed. Based on the FMR responses of in-plane and out-of-plane applied magnetic field configurations, there is an indication of a weakly coupled spin system with a very unusual magneto-resistance.

3.4.3 Micromagnetic simulations for out-of-plane magnetic field

To further support our experimental results, we also perform the micromagnetic simulation based on finite element approach. The simulations were carried out using MuMax^3 [69] software package, running on high performance GPUs on a computer. In these simulations, the time-dependent solution of the magnetization vector field is calculated. A model of a magnetic device is first created and divided in cells (meshing procedure). For each cell, Landau-Lifshitz equation is solved. The effective field is the combination of exchange field, dipole field, externally applied field, magnetic anisotropy field, and thermal fluctuation field. The dipole field and the exchange field in one cell depend on the magne-

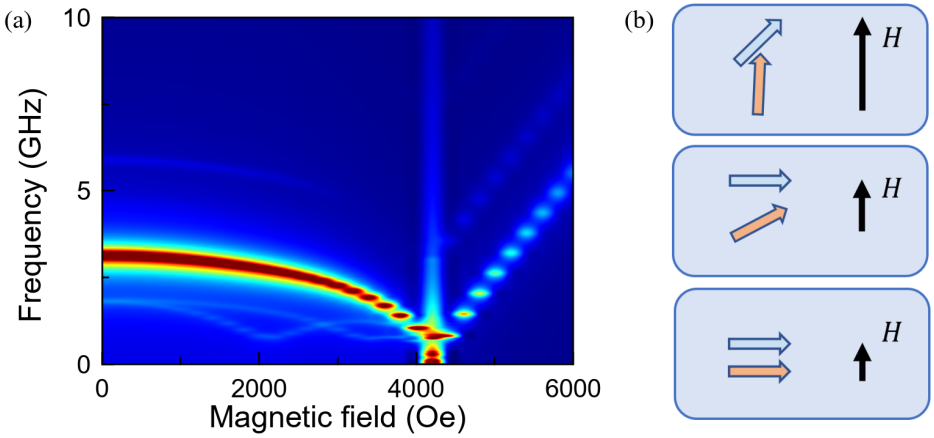

Figure 3.8: (a) Color plot of micromagnetic simulation of ST-FMR in a YIG/Ni bilayer nanowire at 77 K and zero direct bias current. The external magnetic field is applied perpendicular to the device plane. The field is swept from 0 to 6000 Oe. The red colored mode that is visible in between 0 to 4000 Oe is a non-aligned mode. (b) The schematic representation of magnon modes in the presence of external magnetic field (H). The orange color is YIG magnetic moment and blue color is Ni magnetic moment. The YIG and Ni have different magnetic moments. So, they require different amount of magnetic fields to align them together. A non-aligned mode is when the magnetic moment and external magnetic field are not parallel.

tization orientation of other cells (via nearest-neighbor exchange, and via long-range dipole interaction), and thus couple the Landau-Lifshitz equations for all the cells.

We run the simulations for the out-of-plane external magnetic field. The simulation shows the presence of both aligned and non-aligned modes. Aligned modes appear when the external magnetic field and the magnetization vector are parallel to each other. On the other hand, non-aligned modes appear when the equilibrium magnetization direction and the external magnetic field are not parallel to each other. In Figure 3.8 (b), we can see the equilibrium magnetization direction in the presence of different magnetic field magnitude.

3.5 Microwave emission spectroscopy and auto-oscillations

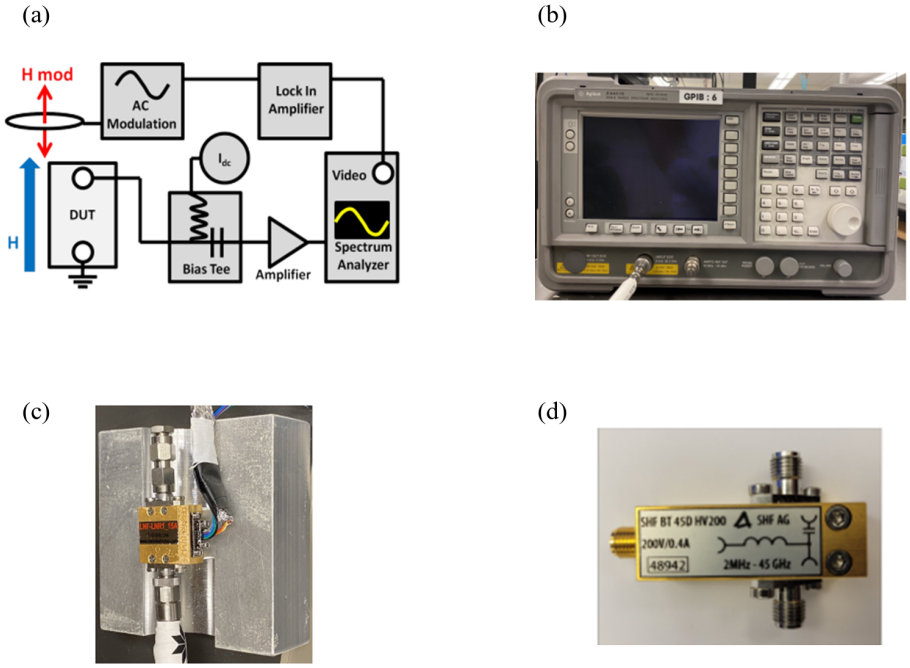

Figure 3.9: (a) Adapted from [73], Schematic of field modulated microwave emission spectroscopy. (b) Spectrum Analyzer, operating range: 9 kHz to 26.5 GHz. (c) Ultra low-noise microwave amplifier, operating range: 1-15 GHz. (d) The bias tee offers the ability or detect DC current in a bias microwave circuit operating in the range of 2 MHz-45 GHz.

When a spin current is injected into the ferromagnetic material, it can exert anti-damping spin torque to the magnetization and lead to auto-oscillations. When the anti-damping torque compensates the effective damping torque of the magnetic material, a GHz range persistent auto-oscillation dynamics can be excited [51, 54, 55, 56, 75, 76]. These magnetization oscillations translate into resistance oscillations due to magnetoresistive effects. The oscillating resistance translates into RF voltage signals under a DC electric current

supplied to the sample. We measure this RF voltage signal using a Spectrum Analyzer (SA) setup.

The schematic of the microwave emission spectroscopy is presented in Figure 3.9 (a) [73]. The generated RF voltage signals are small. These signals are pre-amplified (Figure 3.9 c) before being sent to the spectrum analyzer. The filters and mixers on the spectrum analyzer are adjusted to pick up on a single frequency. The signal is then sent to the lock-in amplifier, where the magnetic field modulating frequency is used as a reference frequency.

Figure 3.10 is a microwave emission spectroscopy performed for a short nanowire at a constant frequency of 3.2 GHz. In microwave emission spectroscopy, we supply the DC current, apply the magnetic field and look at the microwave emitted from the nanowire through the spectrum analyzer. The magnetic field is applied perpendicular to the device plane. At low current we do not observe any signal. At about 7 mA we observe a sudden onset of microwave emission. These are the clear signatures of auto oscillations. In fact, we see multiple auto-oscillatory modes that correspond to non-aligned modes. One of the modes that passes through the zero field region is interesting, which corresponds to a strong nonlinear frequency shift [53].

Now we take a long nanowire. We observe the auto-oscillation at a much lower critical current as shown in Figure 3.11. This is associated with Ohmic heating. In the long nanowire, more heat is confined than in the short nanowire that results in lower threshold of supplied DC current. However, our device's top layer is a ferromagnetic metal that has an intrinsic spin charge conversion effect. We also know that the spin-orbit torque driven by spin charge effect mechanism is an odd function of electric current. So, we do the

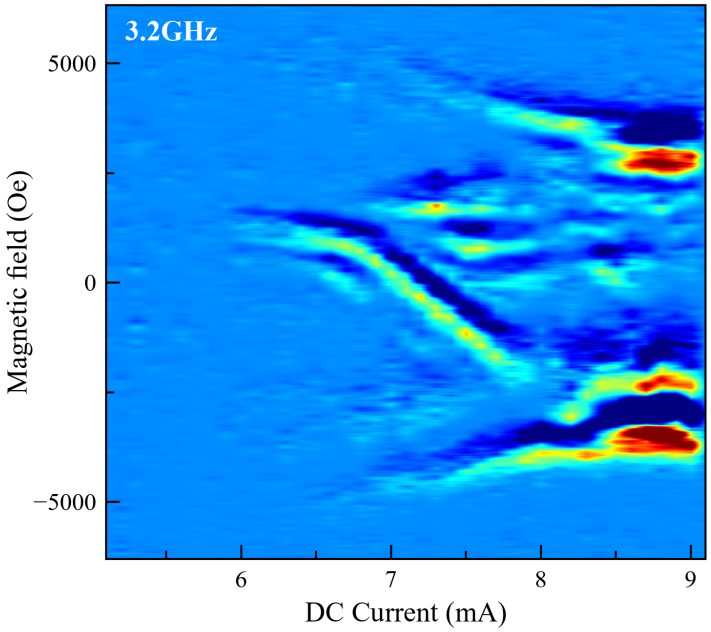

Figure 3.10: Color plot of a microwave emission spectroscopy of a short (900 nm × 4 μm) nanowire of YIG/Ni bilayer at 3.2 GHz microwave frequency and 77 K. The magnetic field is applied perpendicular to the device plane, and is swept from -6000 Oe to +6000 Oe. At about 7 mA, we observe a sudden onset of microwave emission – auto-oscillation mode.

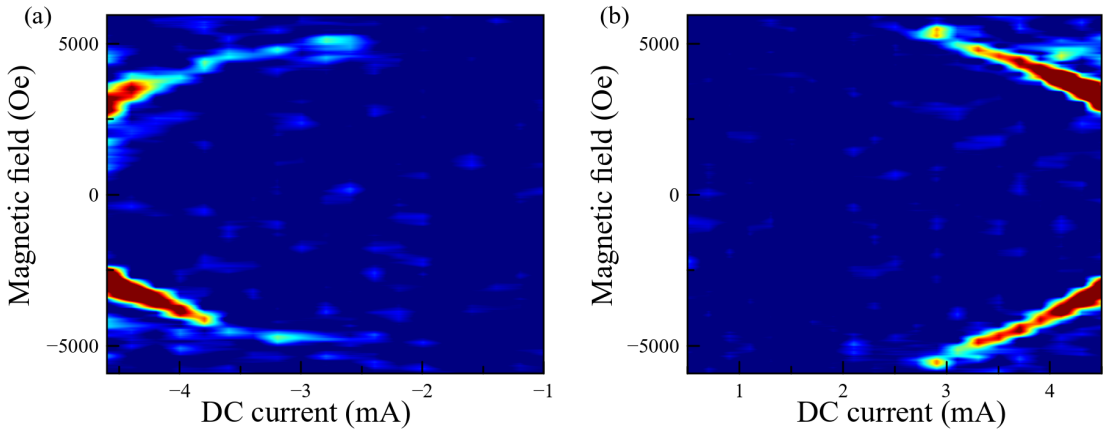

Figure 3.11: Color plot of a microwave emission spectroscopy of a long (900 nm × 7 μm) nanowire of YIG/Ni bilayer at 3.2 GHz microwave frequency and 77 K. The magnetic field is applied perpendicular to the device plane, and is swept from -6000 Oe to +6000 Oe. At about 3 mA, we observe a sudden onset of microwave emission – auto-oscillation mode. The auto-oscillation is driven by spin-Seebeck effect.

measurement under the reverse polarity of the current. We observe the symmetric modes at both positive and negative magnetic fields, and DC current. We also can verify that the auto-oscillation modes threshold current is about the same in both current polarities. This is a strong indication that the auto-oscillation generated in the system is from spin-Seebeck torque [55, 56] as it is independent of the polarization of electric current and only depends on the temperature gradient between the magnetic hetero-structures.

3.6 Summary and outlook

In summary, we have fabricated and studied two magnet hybrid nano-structures. We found weak but complex interfacial coupling that leads to weakly hybridized magnon modes. We observe auto-oscillation when the direction of magnetization of Nickel is oblique, and the YIG magnetization is nearly saturated in the out-of-plane configuration. We observe a strong non-linear frequency shift of the auto-oscillation near zero field. We conclude that the auto-oscillations observed in our two magnet hybrid nano-structure are driven by spin-Seebeck effect. A strong nonlinear frequency shift might be particularly important for the neuromorphic system. Furthermore, our work shows the proof of concept that energy efficient thermally driven auto-oscillations can be achieved and give room for further increase in functionality of two magnet hybrids, and for merging the spin-orbitronic and spin caloritronic concepts.

Chapter 4

Development of low-temperature high-magnetic field insert

4.1 Motivation

Low temperature environment serves as a home to a lot of interesting physics. They are also crucial for spintronic applications [36]. At low temperatures, thermal fluctuations are reduced, which helps maintain the coherence of electron spins. Low temperature minimizes scattering mechanisms that can disrupt the orientation and transport of electron spins, thus leading to a longer spin lifetime and more controlled spin dynamics. Low temperature conditions facilitate efficient spin injection and detection due to reduced thermal fluctuations.

On the other hand, high magnetic fields are of great importance as well to reach various magnetic phases such as spin flop phase transition in some antiferromagnets. We

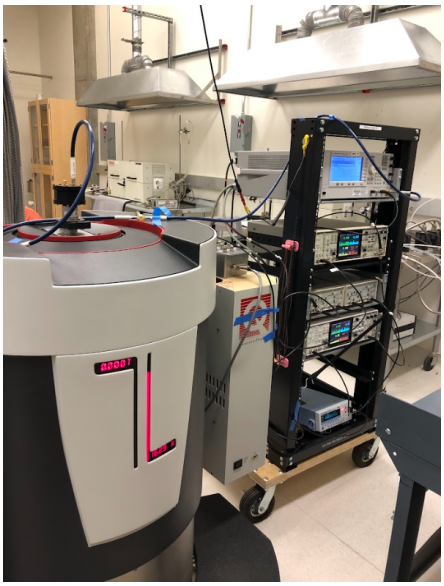

Figure 4.1: Physical property measurement system (PPMS) Dynacool.

may need a high magnetic field to overcome high anisotropy field [77] and the exchange interaction.

We need magneto-transport measurements to access spin transport through magnetoresistance (MR) effect [23]. Microwave spectroscopy helps us evaluate magnetic properties like anisotropy, damping, and inhomogeneity. For the microwave spectroscopy experiments, we'll use both inductive and electrical methods, such as spin pumping [26] or magnetoresistive techniques. Ultimately, we need to integrate magnetotransport with inductive and electrical microwave spectroscopy for our research.

We use the Physical Property Measurement System (PPMS) Dynacool by Quantum Design available that provides the magnetic field 0-14 T and temperature range 1.5 K-400 K. In a series of self-designed inserts, commercial insert, custom-designed parts and adaptations, and software adaptation, we have achieved this goal.

4.2 Design of insert

The PPMS system has a cylindrical bore of 1 inch diameter and 36 inches length. To fit inside the PPMS bore, multi-component probe insert was developed as a multi-step process. The design encompasses a structural layout consisting of a rod with a bracket at its lower end that is attached with a puck that establishes electrical connectivity with the PPMS. Using the SolidWorks software, the general assembly, bracket, coil bobbins, coplanar waveguide (CPW) holder, and a new peg were designed. While the bracket underwent precise machining, the other components were crafted through 3D printers in the lab.

The insert was optimized prioritizing non-magnetic mechanical parts. A rubber was also used to address thermal stress concerns. The objective was to engineer a measurement solution that integrated 3D printed plastics and metallic elements. The final insert was an assembly that fits perfectly and works well with the PPMS system.

4.3 Design of Coplanar Waveguide

The coplanar waveguides (CPW) are designed [78] for a wide range of techniques with a specific measurement of a central line width on a 30 mil standard Rogers 4350 board. They're made of a mix of Copper and Gold (Cu/Au). These coplanar waveguides are 50 Ω impedance-matched and over 40 GHz bandwidth that can support the signals ranging from a few hundred megahertz to tens of gigahertz.

Figure 4.4 (a,b) are the pictures of broadband coplanar waveguide; (a) is the waveguide suitable for inductive or spin pumping type of measurements, and (b) is the

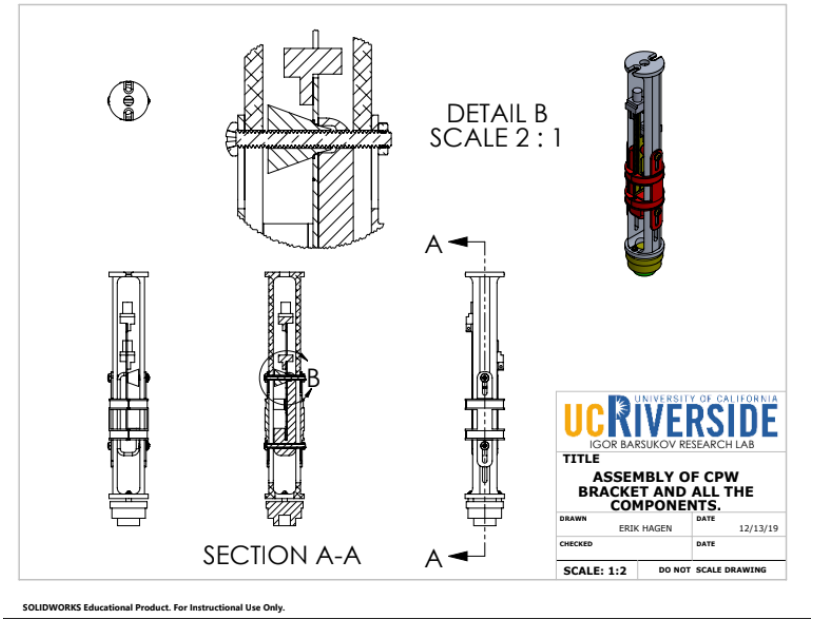

Figure 4.2: The sketch of general assembly of the bracket. The bracket is the bottom part of the insert where coplanar waveguide and all the components sit together in a compact setting. The drawing was created by my lab-mate Erik Hagen.

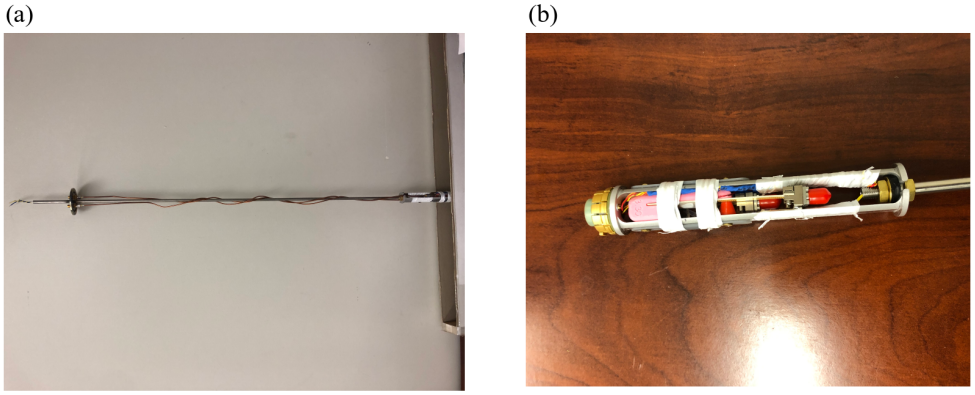

Figure 4.3: The final version of low-temperature high-magnetic field insert developed for PPMS Dynacool. (a) The overview of the insert from top to bottom. (b) A machine shopped sample holder bracket where multi-components including the coplanar waveguide sit compactly.

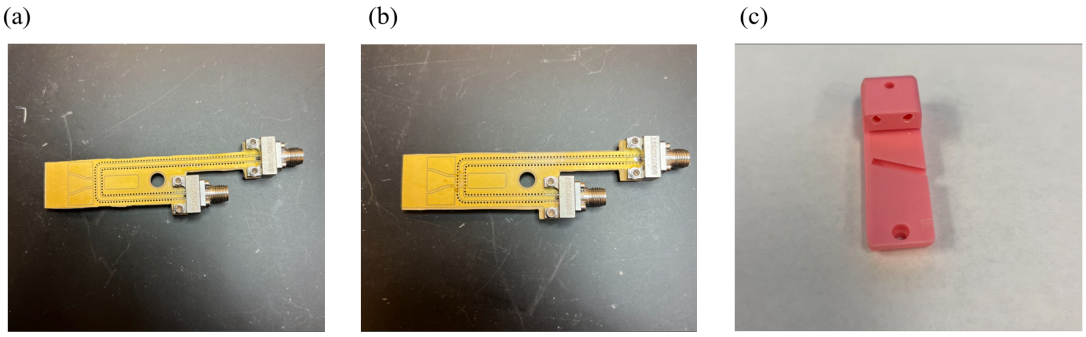

Figure 4.4: (a) Image of a coplanar waveguide for inductive or spin pumping type of measurements. This waveguide has a continuous central conducting channel between two SMA ports. (b) Image of a coplanar waveguide for spin torque type of measurements. This waveguide has a discontinuity in the central conducting channel between two SMA ports. (c) Image of a coplanar waveguide holder that sits inside the bracket. At the central region of the holder a slanted trench is designed to fit the temperature sensor. The holder is locked in place with a peg.

waveguide that has a discontinuity in the central conducting channel, thus making it suitable for spin torque type of measurements. Figure 4.4 (c) is a 3D printed waveguide holder for the probe insert. The waveguide holder has a temperature sensor placing area built within it.

4.4 Microwave and low-frequency connections

The cryogenic insert for the PPMS system incorporates specialized microwave components tailored for operating in low-temperature environments. These components encompass microwave connectors, low and high-frequency current circuitry deliberately engineered to function optimally under cryogenic conditions and high magnetic fields. To facilitate seamless connectivity from the interior to the exterior of the PPMS bore, an RF

feedthru is utilized on a KF-40 flange as shown in Figure 4.5 (c). Moreover, implementation of semi-rigid cables within the insert enables microwave transmission up to 40 GHz.

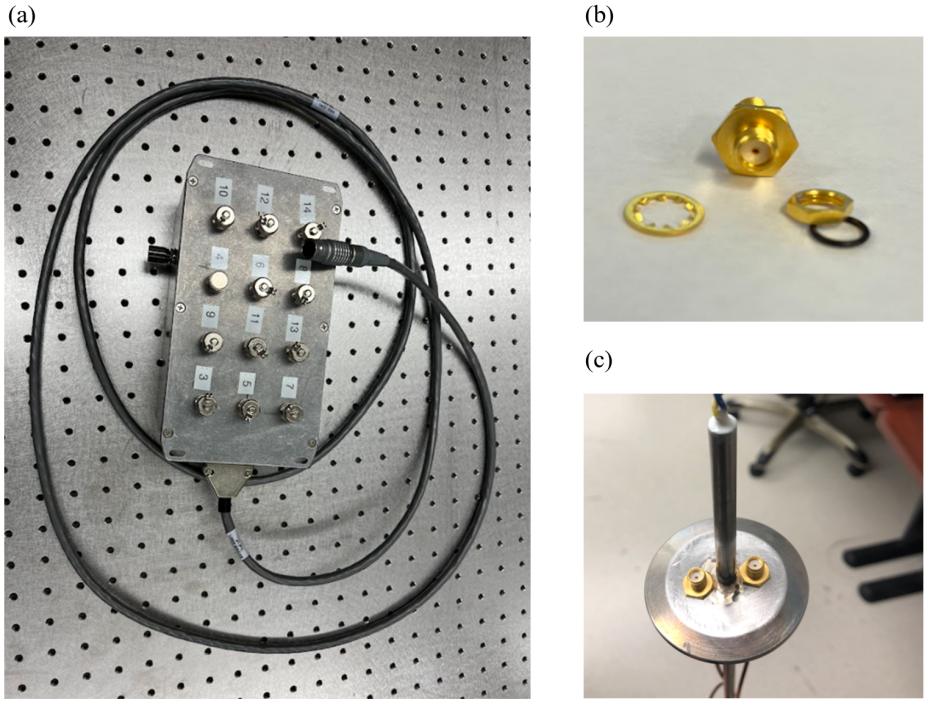

Figure 4.5: (a) Low frequency connection breakout box. The box has BNC connectors. These connectors are connected with low-frequency cables. One end of the breakout box is connected to the PPMS system, and the BNC ports are used to connect to our measurement equipments. (b) RF-feedthru used for microwave transmitting between the interior and exterior of the PPMS bore. (c) RF-feedthru utilized on a KF-40 flange.

For the low frequency connections, I assemble the breakout box from a metallic enclosure as shown in Figure 4.5 (a). The BNC connectors are added on the breakout box. These BNC connectors are wired with low frequency cables. The breakout box serves as a

bridge between PPMS and measurement equipments for the low frequency channel. I tested the performance of the breakout boxes with a signal generator and an oscilloscope. All these components and parts collectively form a robust system, enhancing the insert's capacity for microwave transmission and establishing a reliable means of uninterrupted measurements and signal transference from the cryogenic environment of the PPMS system. Choosing and combining these components show the detailed planning needed to make a specialized insert that works well in the desired cryogenic and high magnetic field environment.

4.5 Magnetic field modulation

The magnetic field modulation technique [74] is a reliable way to obtain the signal free of non-magnetic background noise. In this method, the external magnetic field is modulated using the coils made out of copper wire. The lock-in amplifier sources us the required output AC voltage that is transmitted to the sound amplifier that amplifies the AC voltage.

Figure 4.6 (b) shows modulation coil assembled in the insert. It is very important to ensure that the modulation field stays way below the linewidth field of the signal. If not, over-modulation artifacts such as linewidth broadening may occur. We should calibrate the modulation field by measuring and fitting the linewidth as a function of modulation current amplitude, and choose the modulation amplitude appropriately.

The modulation field amplitude is proportional to the modulation voltage, and based on our design and construction the modulation current may be approximated by magnetic field for the Helmholtz's coil [79]:

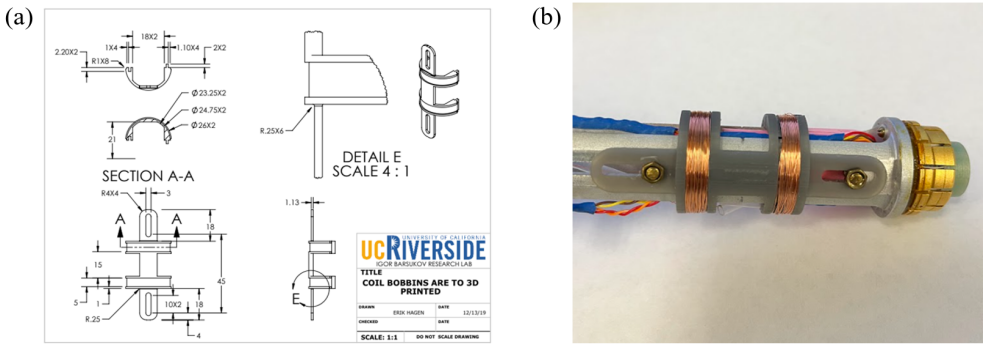

Figure 4.6: (a) The sketch of a coil bobbin drawn by my lab mate Erik Hagen. The coil bobbin is used as a holder for modulation coil setup. (b) An image of a modulation coil sitting on a coil bobbin, which is wrapped around the bracket. The coil bobbin is tightened with two screws, and it sits firmly on place.

$$B_{mod} = \left(\frac{4}{5}\right)^{3/2} \cdot \frac{\mu_0 N I_{mod}}{R} = c \cdot I_{mod}$$

where μ_0 is the permeability of the free space, R is the radius of the coil, N is the number of turns in each coil, and I_{mod} is the current through the coil.

4.6 Software adjustments

To facilitate the interaction between the computer and the PPMS for conducting measurements with the cryostat insert, a Python API serves as the bridge. This API functions as the intermediary, enabling communication and control between the computer and the Quantum Design (QD) socket server. The QD socket server acts as a communication interface that allows the computer to establish a connection with the MultiVu software of the PPMS. Through the Python API, specific protocols and commands are utilized to configure and interact with the QD socket server, establishing the necessary port for

seamless communication. This setup allows for the remote control and automation of the PPMS, enabling the initiation and management of measurements in the PPMS.

4.7 Benchmarking

The successful test run, Figure 4.7, on 10 nm thin film Permalloy (Py) sample marks a significant milestone in the development of the experimental apparatus. The test spectrum is measured with the magnetic field applied along the easy plane of the film at 20 Kelvin. The frequency of 7 GHz is used with the nominal power at the source of 7 dBm. The 3% field modulation is used.

The observed ferromagnetic resonance [80] spectrum validates the functionality of the equipment and affirms that it is capable to detect and characterize essential properties of the measured material. The test run stands firmly as a proof to the insert's reliability and functionality. The presence of both the raw data and the corresponding graphical representations stored in the drive underscores the thoroughness of the experimental process. This achievement not only corroborates the effectiveness of the developed apparatus but also sets the stage for further investigations and discoveries that could significantly advance our understanding of material science and its applications in diverse fields. Now, we are all set to perform the microwave spectroscopic measurements in the anti-ferromagnetic materials.

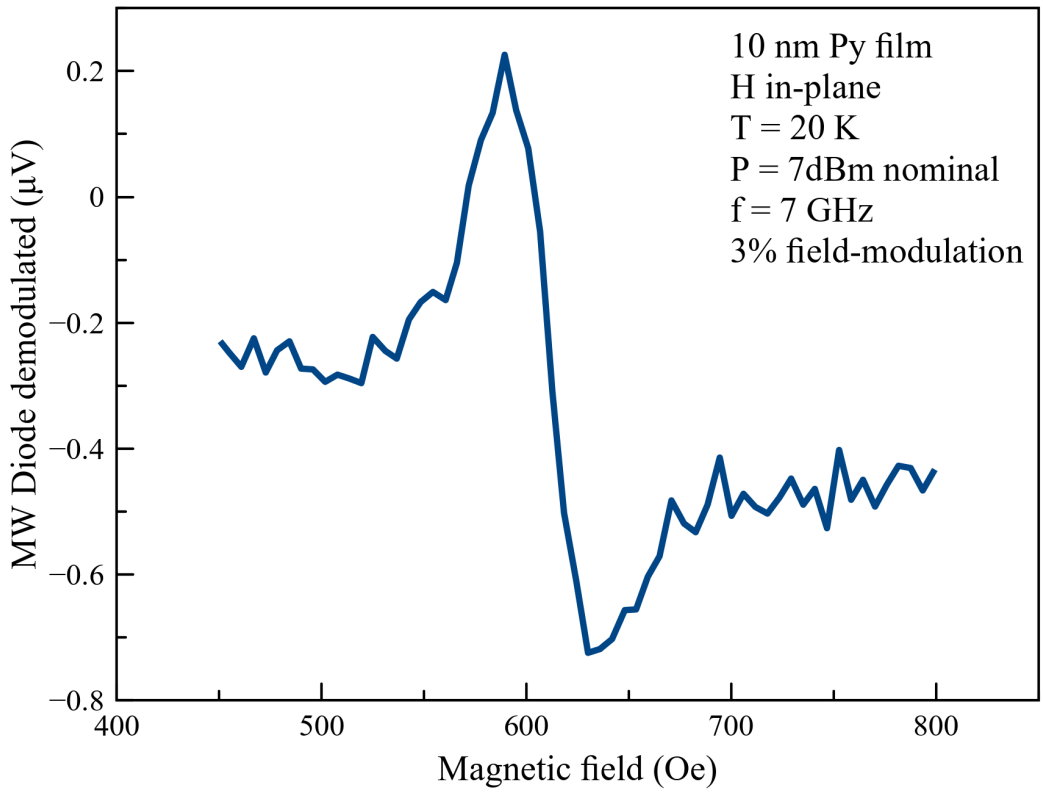

Figure 4.7: Field modulated ferromagnetic resonance signal on a 10 nm thin Py layer measured using the low-temperature and high magnetic field insert developed by me. The observed signal serves as a proof of insert's performance.

Chapter 5

Electrical readout of coherent spin dynamics in an insulating antiferromagnetic crystal

5.1 Introduction and motivation

In the last decade, antiferromagnetic spin systems have moved to the forefront of spintronics research as highly promising candidates for the future of information technologies [81, 82]. Antiferromagnets (AFMs) have ∼1000 times faster spin precession than ferromagnets with frequencies lying in the terahertz (THz) regime [83]. In AFMs, many intriguing spin phenomena are expected that go beyond the ferromagnetic spin systems. For instance, spin excitation (magnon) in easy-axis AFMs can carry positive and negative spin polarization, providing a potential extraordinary means for advanced computation schemes.

AFMs possess no stray fields and can thus be used for spintronics applications with large device-per-area density [83]. For the very same reason, however, AFMs are weakly susceptible to excitation by magnetic fields and require another means of spin manipulation.

The interfacial spin torque phenomena may provide a route for energy-efficient and versatile spin control [84, 85]. Antiferromagnetic spin dynamics has been directly observed in bulk systems using optical methods [86]. By using neutron scattering, antiferromagnetic magnons have also been observed in bulk [87]. THz antiferromagnetic resonance (AFMR) signal from spin pumping has been detected in bulk [88, 89, 90] in the sub-terahertz frequency range.

Antiferromagnetic resonance signal from spin pumping has also been measured by our group in the gigahertz frequency range close to the spin flop region, which opened the way towards exploring the anti-ferromagnetic spin dynamics using state-of-the-art GHz electronics. In spin pumping detection technique, the inverse spin Hall voltage scales with the size of the device, but the modern day technologies demand nanoscale devices. Thus, it is very important for us to scale our anti-ferromagnet based devices down to nanoscale. In this chapter, I explore the spin dynamics in bulk antiferromagnets with thin layer of non-magnetic metal using the magneto-resistive antiferromagnetic resonance technique at the microscale. If we succeed, we will move our way towards the spin-torque antiferromagnetic resonance at nanoscale devices. But, first I would like to start with the discussion of the materials of choice, and the fabrication procedures.

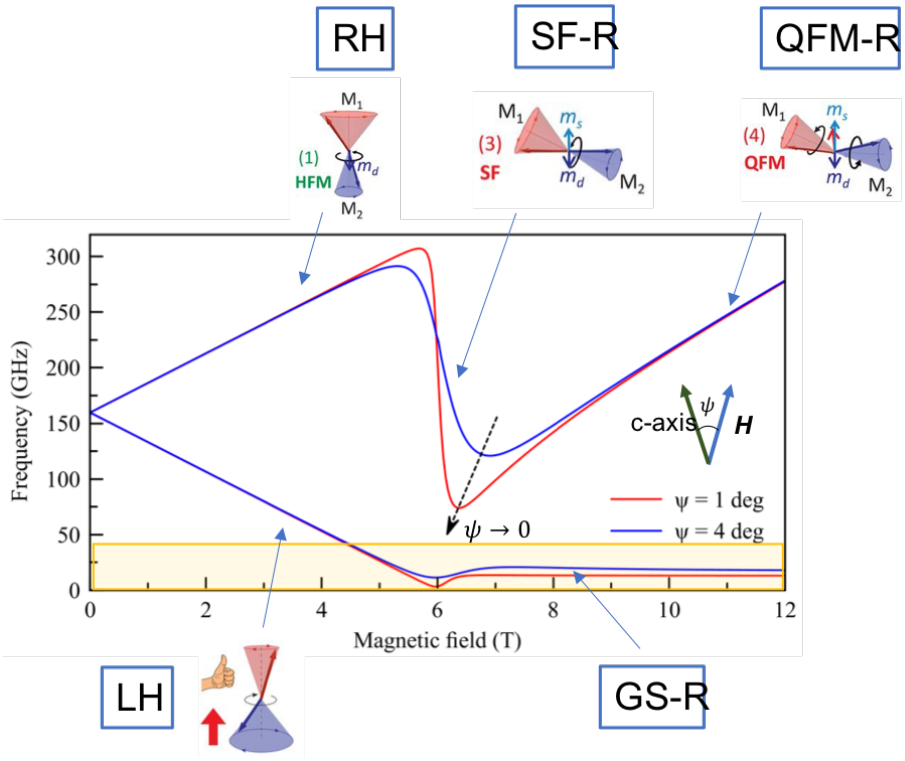

Figure 5.1: Frequency vs magnetic field relation at 0 K in bulk Cr2O3. Magnon's degenerate energy state at 0 T splits into left hand (LH) and right hand (RH) mode as we increase the external magnetic field. After the spin flop (SF-R) field at 6 T, quasi-ferromagnetic (QFM-R) mode is excited. ψ is a misalignment angle between the c-axis and the external magnetic field. When the misalignment is present we observe the Goldstone-like mode (GS-R).

5.2 Materials of Choice

In our experimental pursuit, the choice of the materials is chromium oxide (Cr2O3) and platinum (Pt), each possessing unique and defining characteristics. Cr2O3 is a uniaxial antiferromagnetic insulator, characterized by its easy axis aligned along the c-axis of the corundum crystal type with hexagonal lattice [91, 92, 93]. The critical Néel temperature for Cr2O3 is around 308 K. Figure 5.1 shows the overview of the antiferromagnetic resonance modes in Cr2O3. The antiferromagnetic resonance frequency is approximately at 165 GHz

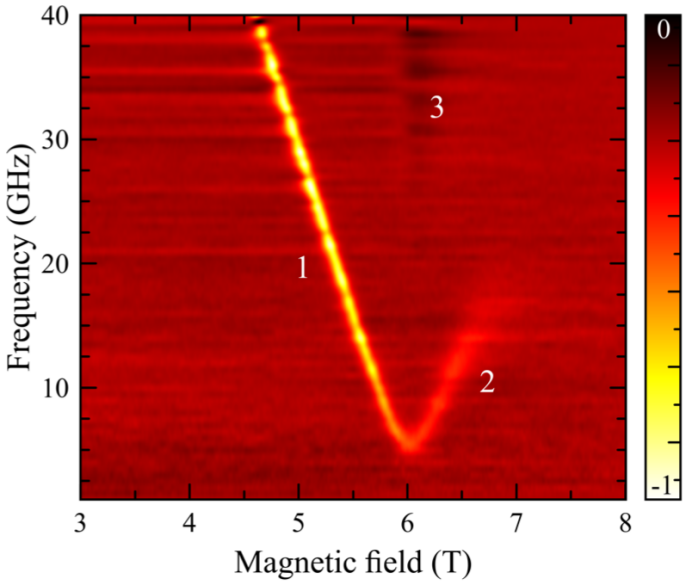

Figure 5.2: Color plot of frequency vs magnetic field relation of an inductively measured antiferromagnetic resonance signal in a bulk Cr2O3 at 5 K. 1 is the left handed mode, 2 is the Goldstone-like mode, and 3 is the spin flop mode.

at 0 T and a spin flop field is at 6 T at 0 K. Figure 5.1 also shows the Left Handed mode (LH), Right Handed mode (RH), Spin Flop mode (SF-R), Quasi-Ferromagnetic mode (QFM-R), and Goldstone mode (GS-R) as a function of applied magnetic field. Figure 5.2 is the color-coded plot for the left-hand resonance mode of Cr2O3 that is measured inductively.

Platinum (Pt) is a non-magnetic heavy metal. Due to high atomic number, Pt has a significant spin-orbit interaction. This enables Pt to generate a pure spin current owing to the spin Hall effect (SHE) [12, 13, 94].

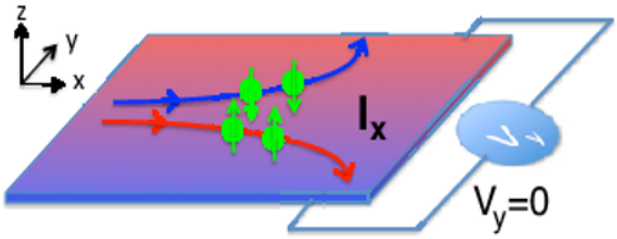

Figure 5.3: Adapted from [95]. Schematic of the depiction of spin Hall effect (SHE). This effect generates the pure spin current by means of spin dependent scattering of conduction electrons due to spin-orbit interaction.

5.3 Nano and micro-fabrication

The bulk Cr2O3 with the pre-defined crystal plane and c-axis were purchased from the SurfaceNet GmbH. I did the fabrication on (11-20) plane and (0001) plane Cr2O3 crystals.

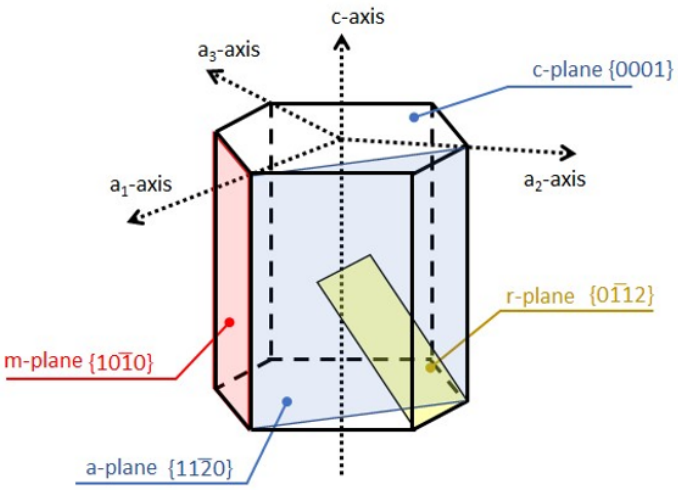

Figure 5.4: Adapted from [96]. Crystal planes and orientations.

5.3.1 Fabrication of a nano-cross device

The following steps were used to prepare the nanodevice:

Sputter deposition: I deposited a 5 nm of Pt on top of the bulk Cr2O3. The deposition was done using AJA sputtering with 4 mTorr of Ar gas pressure and 10^{-7} Torr of system pressure with 18 Watts DC power.

Electron beam lithography: Next step is to pattern the device structure on the surface. Fabrication of the nanodevice was carried out using the electron beam lithography (EBL). After the thorough cleaning of the specimen with acetone, and isopropanol, the Cr2O3/Pt film was first coated with the negative resist MAN-2401 of around 100 nm thickness. The spin coating was performed at the rate of 3500 rpm for 45 seconds. The resist was baked out on a hot plate for 1 minute at 90 °C.

The resist was patterned into nanowires and leads using EBL with the nanometer pattern generation system (NPGS) software. The typical write current was 15 pA and area dose was about 200 - 300 μC/cm^2. The center to center distance and line spacing were set to 1 nm. After the EBL writing, the developer (maD-525) was applied for 60 seconds, and the sample was rinsed with HPLC water for 3 minutes.

Ion-milling: After defining the patterns, the sample was ion-milled at an incident angle of 65 deg for several minutes (according to calibration such that Cr2O3/heavy metal material is etched up to the substrate: Pt etching rate is 3.7 nm/min). Duty-cycling and water cooling of the sample was used during the ion milling to prevent the sample from overheating. The remaining resist was removed using sonication in acetone.

Final nano-cross device: Figure 5.5 is a scanning electron microscopy image of a nano-cross device fabricated on a Cr2O3 crystal substrate. The pattern visible on the top is a 5 nm thick platinum layer. The zoomed-in image shows the device's active region

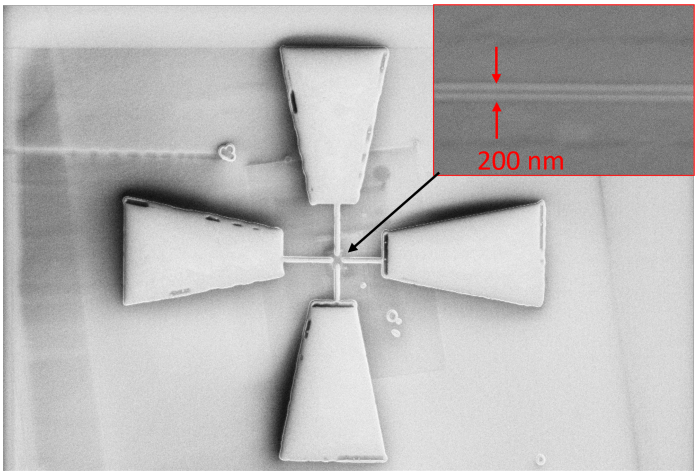

Figure 5.5: Scanning electron microscopy image of the nano-cross device on a Cr2O3 bulk crystal. The pattern visible is thin layer (5 nm) of Pt. The larger pads are for wire-bonding to provide an electrical connections to the device. The inset figure is the nanowire that is 200 nm wide and 10 μm long.

that has a width of 200 nm and length of 10 μm. The larger pads are for wire-bonding to provide an electrical connections to the device.

5.3.2 Fabrication of a "pizza device"

I followed the following procedures to prepare the pizza device.

Photo-lithography: The photolithography process was performed after completing standard cleaning procedure of the substrate. The substrate was pre-baked on a hotplate for 2 minutes at 180 °C to remove any organic solvent residues. I applied the s-1813 positive photoresist and spin coated at the rate of 4000 rpm for 45 seconds to receive a thickness of 1.3 μm. The resist was soft baked for 1 minute at 115 °C.

An optical mask was designed in the lab and fabricated commercially in the course of this work. The optical mask was aligned with the substrate. The patterns were exposed for 10 seconds with "flood type exposure" under UV light. The s-1813 resist becomes soluble

in the developer after exposure, in contrast to negative resist, where the unexposed areas are soluble in the developer. The developing was done using the MIF-319 developer for 60 seconds. The substrate is now ready for metal deposition.

Sputter deposition: I deposited a 5 nm of Pt film on top of the bulk Cr2O3. The film was deposited at room temperature using the magnetron sputtering with 4 mTorr of Ar gas pressure and 10^{-7} Torr of system base pressure. The deposition rate of Pt was 0.36 Å/s at 18 Watts DC power.

Lift-off: The deposition of Pt was followed by the lift-off process. I soaked the specimen in acetone for about 15 minutes. I checked the device under the microscope for any residues. The remaining resist was removed by sonication.

Final "pizza" device:

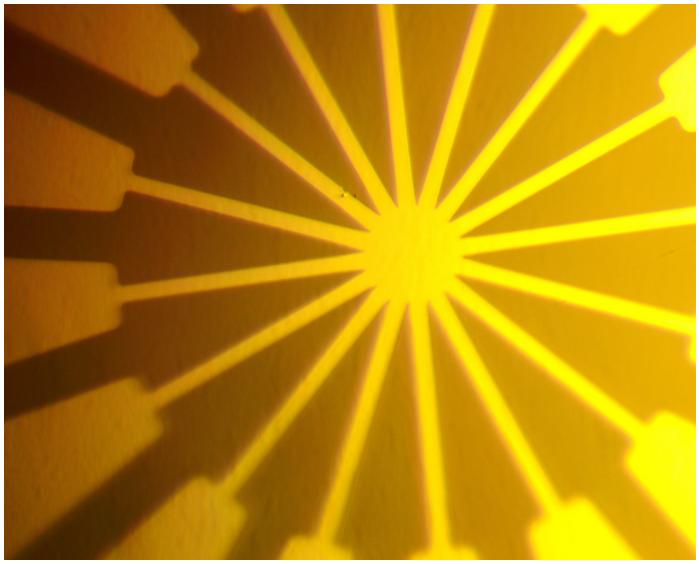

Figure 5.6: Optical microscopy image of the micro-structure device on a Cr2O3 bulk crystal. The pattern visible is thin layer (5 nm) of Pt. The device is a microwire of 10 μm wide and 200 μm long. The microwire extend to the larger pads on both ends. The larger pads are used for wire-bonding to provide an electrical connections to the device.

Figure 5.6 shows the optical microscopy image of the final "pizza" device. The shiny patterns are the platinum deposited on the Cr2O3 crystal. There are eight micro-structure wires in the pizza-device. Each wire is $10\,\mu$m $\times$ $200\,\mu$m. All the wires pass through the center making the center large. The wire ends on both ends with wire-bonding pads for electrical connections to the pizza device.

5.4 Excitation and detection techniques

5.4.1 Inductive excitation, microwave transmission detection

A magnetic material to be measured is placed directly on top of the coplanar waveguide. The microwave frequency propagates through the waveguide. This microwave generates an oscillating magnetic field in a circular fashion around the direction of the microwave propagation. The generated magnetic field, also known as Oersted field, induces an excitation of the spin in the direction perpendicular to the easy axis of the magnetic material. When the spin excitation frequency and the driven microwave frequency comes into a resonance, the microwave transmission through the waveguide drops. This is an inductive way to perform the measurement (Figure 5.7). The resonance signal can be collected with the lock-in amplifier or a nano-voltmeter.

5.4.2 Inductive excitation, magneto-resistance detection

This process involves excitation by the Oersted field and the detection by magnetoresistance (MR) technique. The MR detection requires spin-charge conversion. Since the

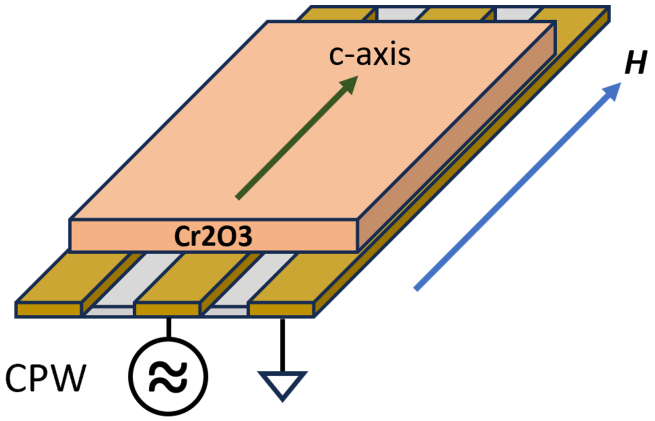

Figure 5.7: The microwave current flowing through coplanar waveguide (CPW) generates an Oersted field or high frequency field transverse to the direction of microwave current flow. The Oersted field excites spin waves in the bluk Cr2O3 crystal sitting on a coplanar waveguide. The microwave transmission is converted into a measurable voltage signal using the microwave diode.

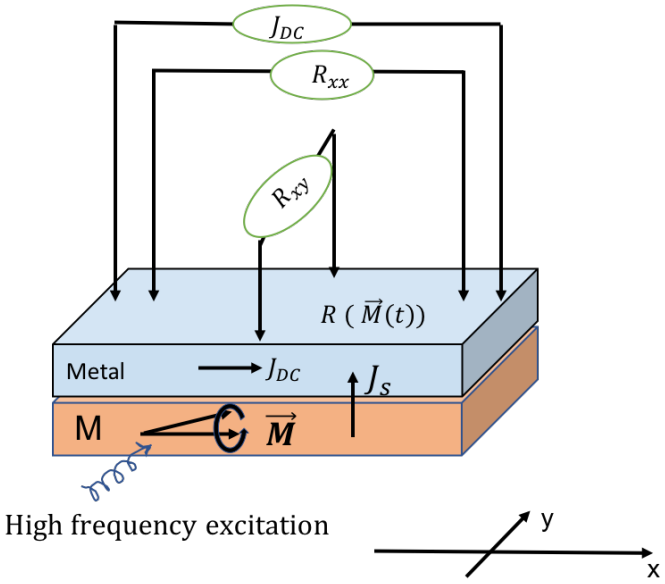

Figure 5.8: Depiction of inductive excitation and magneto-resistive detection of spin dynamics. High frequency magnetic field induces magnetization dynamics in the magnetic material. This oscillating magnetization couples with the electron spins in the metallic layer resulting in the resistance oscillations due to magnetoresistive effect.

magnet is an insulator, we need a conducting overlayer that would facilitate interfacial spin transport and ensuing spin to charge conversion. We send the direct current through the metallic layer to conduct electric charge and probe the resistance. The spin waves excited by Oersted field and other torques interact with electrons in the metallic layer and transfer angular momentum to it. This spin current is then converted into resistance fluctuations via spin-Hall magnetoresistance (SMR) [97, 98, 99], which can be described by the equation below.

$$\rho = \rho_0 + \Delta\rho[1 - \cos^2\left(\frac{\vec{M}\cdot\vec{\sigma}}{M}\right)]$$

The difference in the magneto-resistance when it is in-resonance and out-of-resonance mixes with the direct current; thus giving a photo-resistance effect. The magnetoresistive effect helps us probe the spin dynamics of the underlying magnetic materials. This technique opens up the avenue to interface the conductor and magnetic insulator for the next generation spintronic devices.

5.4.3 Spin-torque excitation, magneto-resistance detection

In this technique, we excite the magnetic resonance by spin torque [27, 28] in addition to Oersted field. The surface metallic layer is used to conduct a microwave current. Theis high frequency current generates the spin current in a transverse direction to the flow of current and the spin polarization of current carriers. The spin current is then transferred across the interface of metal and magnetic material. This transferred spin current exerts a torque on the spins of a magnetic material and generates the coherent spin

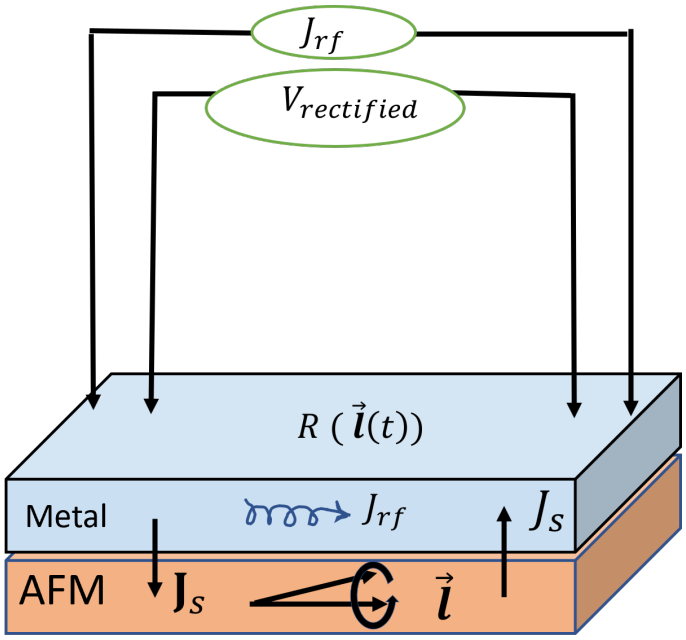

Figure 5.9: Depiction of spin torque excitation and magnetoresistive detection. High frequency microwave current flows through the metallic layer that generates the spin current in the transverse direction. This spin current is injected into the magnetic material that exerts a spin torque to induce magnetization dynamics in the magnetic material. This oscillating magnetization couples with the electron spins in the metallic layer resulting in the resistance oscillations due to magnetoresistive effect.

precession at the drive frequency in the magnetic material. Spin precession in response to such excitation leads to resistance oscillations due to the magnetoresistance effect. Since both the current and resistance oscillations are mostly at the same frequency, they can mix and result in a rectified voltage. This voltage is proportional to the resistance oscillations and thus to the oscillations of the magnetization (or more generally magnetic order). In addition to this so-called photovoltage effect under microwave current, another effect exists – photoresistance refers to difference of the sample resistance in and out of the resonance due to the magnetoresistance under a direct current.

5.5 Adaptation to pulse modulation

We introduce the pulse modulation technique in our electrical detection of anti-ferromagnetic resonance experiment in order to reduce the background noise and to facilitate the detection of the weak signals. In the pulse modulation setup, a microwave frequency is modulated with a low frequency square wave. Figure 5.10 is the picture of the microwave source generator used in my experiment that can also generate the pulse internally. The BNC cable connects the pulse generator Video OUT port in the microwave generator to the Reference-In port in the lock-in amplifier. This configuration enables the generation of microwave pulses from few Hz to several kHz range. We choose the optimum value as required. The final signal received from the device is collected with lock-in amplifier. The microwave pulsing frequency is used as a reference frequency for the lock-in amplifier.

Figure 5.10: Microwave signal generator up to 40 GHz.

5.6 Magnetoresistive (MR) detection of AFMR modes

This section involves the experiment performed to study anti-ferromagnetic resonances in Cr2O3/Pt in a microwire (pizza shaped device) due to the inductive excitation and magneto-resistive detection technique alongside inductive excitation and microwave transmission detection. I perform the experimental measurements of the antiferromagnetic resonance and do the systematic study of the magnetoresistive spin-to-charge conversion of coherent spin dynanmics at the interface, and evaluate the resonance behavior as a function of microwave power, DC current, temperature and crystallographic orientation. Achieving this result is an important milestone in paving the road towards the AFM spin-torque devices.

5.6.1 MR-AFMR on out-of-plane c-axis device

In this section, I present the results of the measurements done in a bulk Cr2O3 (0001) plane that has the c-axis perpendicular to the device plane. The 5 nm of platinum on the top surface acts as a conducting surface. The measured device is a microwire of about 10 μm wide on the pizza device. Figure 5.11 is the picture of the device that is ready to be measured. The device sits with its face facing the top of the coplanar waveguide central conducting channel. Silver paint is used to extend the wirebonding pads from the device to the other side as in Figure 5.11. The copper wire connects the silver paint to low frequency circuitry in the probing insert. The magnetic field is applied along the c-axis of the device. We excite the magnon modes inductively, and detect the signal simulta-

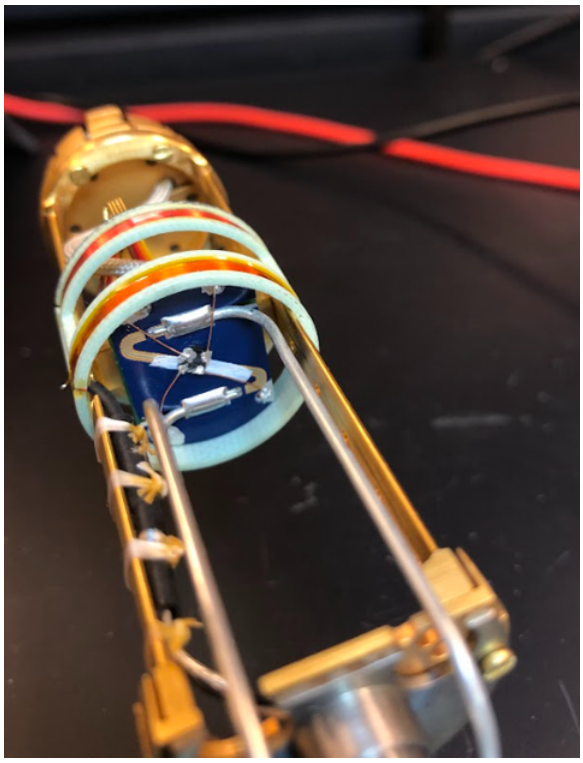

Figure 5.11: Image of the pizza device ready for MR-AFMR measurement. Bulk Cr2O3/Pt with out-of-plane c-axis pizza device sits with its face down on coplanar waveguide of the PPMS insert. Silver paint is used to extend the wirebonding pads from the device. The copper wire connects the silver paint to low frequency circuitry in the insert.

neously using microwave transmission and magnetoresistive detection techniques. For the microwave transmission, the resonance mode is directly observed using the microwave diode that converts the microwave signal into directly measurable voltage signal. For the magnetoresistive detection, the resistance oscillations couple with the probing direct current, and the photo-resistance voltage is measured directly with lockin amplifier.

Figure 5.12 is the result of inductive and magnetoresistive measurement. The measurement is done at 1.5 mA direct current at 50 K. The microwave frequency is 11 GHz and the microwave power is 20 dBm nominal at the source. We sweep the magnetic field from 0 Tesla to 9 Tesla initially to locate the narrow range of fields where interesting physics is

observed, and continue the experimental measurements in the narrow region of interest. We observe two resonance signals for both transmission and magnetoresistance measurements. The left signal is the low-frequency excitation mode, i.e. left hand mode (LHM). The LHM signal amplitude in the magnetoresitive xy channel is about 6 nV, which is extremely small. The right side signal is Goldstone-like mode, with a comparable magnitude. The Goldstone mode is visible at a relatively low microwave frequency range. The Goldstone mode may have originated because of the misalignment between the external magnetic field and the c-axis (which is inevitable in experiment), and the anisotropy within the basal plane of Cr2O3.

Temperature dependence of resonance signal for out-of-plane c-axis

The microwave transmission method of detecting the resonance signal was done for the purpose of comparison to conclude that the signal obtained with magneto-resistive technique is indeed an anti-ferromagnetic resonance signal. The results corroborate that the signals were consistent in both techniques.

Now, we would like to do further analysis of the signal as a function of temperature. The magnetic field is applied perpendicular to the device plane. We use the microwave of 15 GHz at 19 dBm nominal power at the source. A finite direct current of 1.5 mA is applied through the wirebonding pads on the pizza device. We look at the temperature dependence of the MR-AFMR resonance signal on the longitudinal (xx) channel in Figure 5.13 (a), and transverse (xy) channel in Figure 5.13 (b). xx channel is along the probing current, and xy is transverse to the probing current. We observe that the amplitude falls as we go

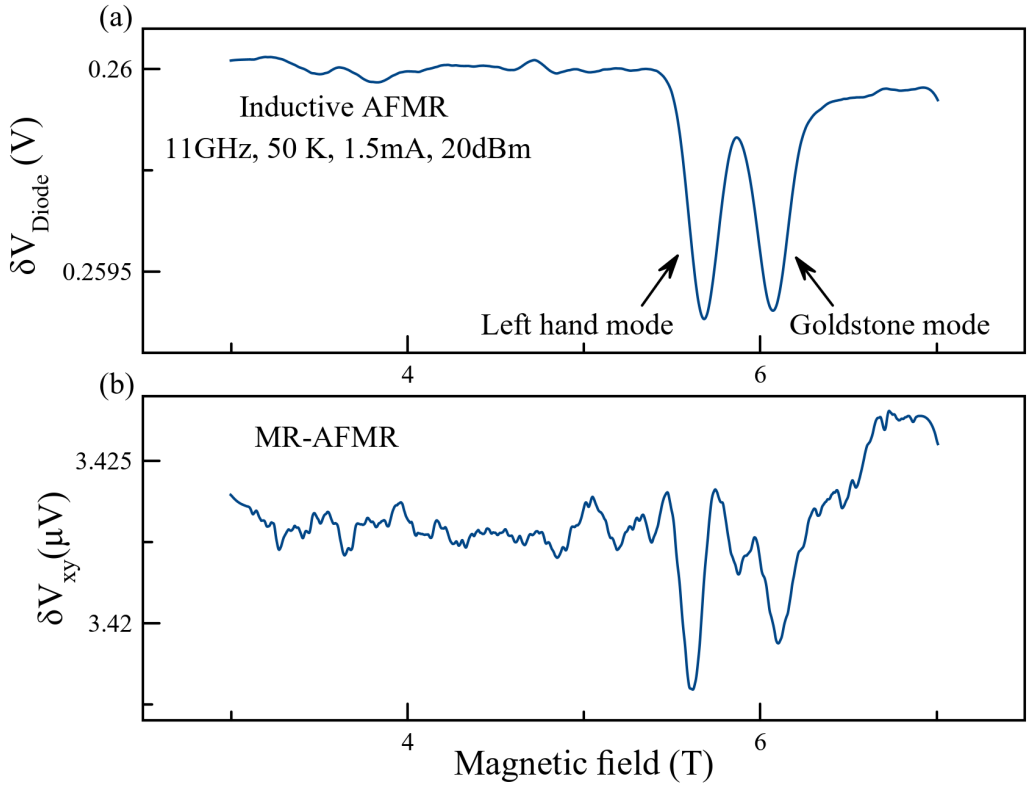

Figure 5.12: Antiferromagnetic resonance signal of a bulk Cr2O3/Pt microstructure device of dimension 10 μm $\times$ 200 μm with the out-of-plane c-axis. The resonance signal is measured at microwave current of 11 GHz with 20 dBm nominal power at the source, and 1.5 mA direct current. The measurement is carried out at 50 K. (a) Microwave transmission detection of AFMR signal. (b) Magnetoresistive detection of AFMR signal of transverse (xy) channel.

higher in temperature. Both of the channels have excitation amplitude maximized at low temperature. xx channel signal falls steeply after 150 K. xy channel signal falls immediately at around 10 K and show a consistently falling thereof, which is similar to the one performed on the previous studies of Cr2O3 [100]. The resonance signal amplitude in xx is about 0.5 μV at 10 K and that in xy is about 0.05 μV at 10 K which is about an order of magnitude smaller than xx. The typical decrease of any signal to charge conversion has been also been observed in the previous study [100].

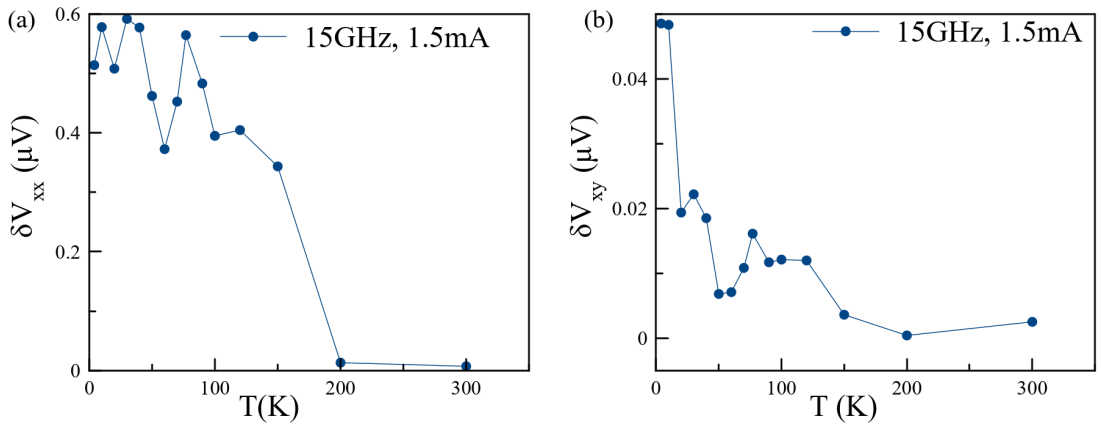

Figure 5.13: The temperature dependence of magnetoresistive antiferromagnetic resonance (MR-AFMR) signal of bulk Cr2O3/Pt microstructure device of dimension $10\,\mu\text{m} \times 200\,\mu\text{m}$ in the out-of-plane c-axis device. The measurement parameters are 15 GHz at 20 dBm nominal source power microwave current and 1.5 mA direct current. (a) MR-AFMR signal vs temperature in the longitudinal (xx) channel. The microwave current flows through the xx channel. (b) MR-AFMR signal vs temperature in the transverse (xy) channel.

5.6.2 MR-AFMR on the in-plane configuration

In this section, I present the results of the measurements performed in a bulk Cr2O3 (11-20) plane that has the c-axis within the device plane. The 5 nm of platinum on the top surface acts as a conducting material. The device measured is about $10\,\mu\text{m}$ wide on the pizza-like device. The device sits with its face facing the top of the coplanar waveguide central conducting channel. Silver paint is used to extend the wirebonding pads from the device to the other side as in Figure 5.11. The copper wire connects the silver paint to low frequency circuitry in the probing insert. The magnetic field is applied along the c-axis of the device. We excite the magnon modes inductively, and do the simulataneous detection of transmission and magnetoresistive signals. For the magnetoresistive detection, we detect the signal on both the longitudinal (xx) channel and transverse (xy) channel,

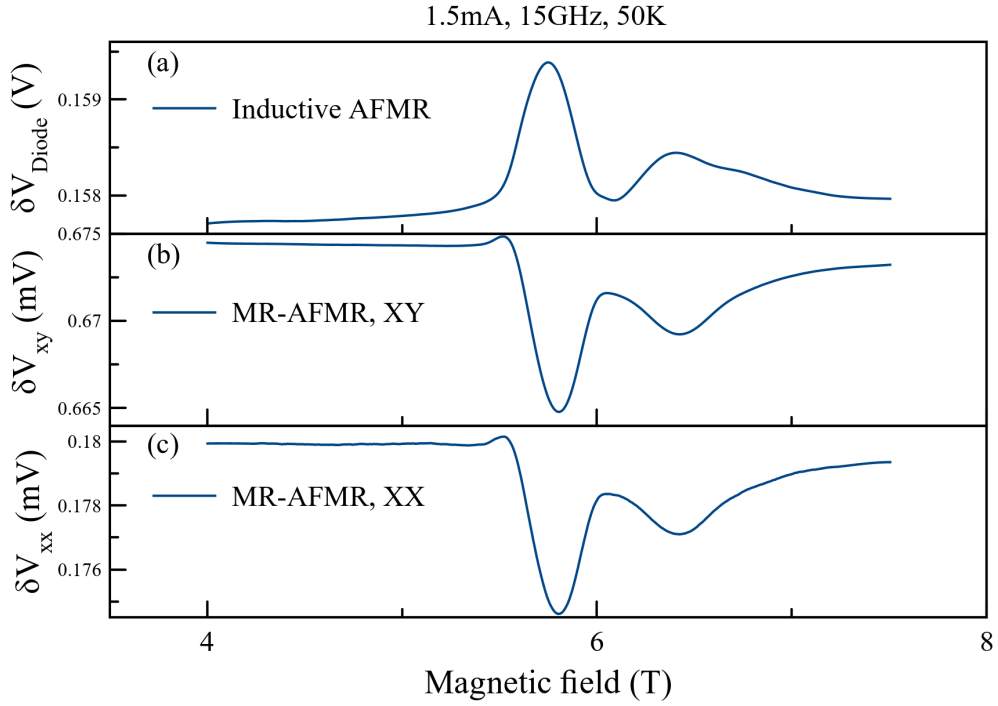

Figure 5.14: Antiferromagnetic resonance signal of a bulk Cr2O3/Pt microstructure device of dimension 10 μm $\times$ 200 μm with the in-plane c-axis. The external magnetic field is applied along the c-axis. The resonance signal is measured at microwave current of 15 GHz with 20 dBm nominal power at the source, and 1.5 mA direct current. The measurement is carried out at 50 K. (a) Microwave transmission detection of AFMR signal. (b) Magnetoresistive detection of AFMR signal in the longitudinal (xx) channel. The microwave current flows through the xx channel. (c) Magnetoresistive detection of AFMR signal in the transverse (xy) channel.

with xx channel along the probing direct current. The signals are collected with the lock-in amplifier.

Figure 5.14 is the result of inductive and magnetoresistive measurements. The measurement is done at a direct current of 1.5 mA at 50 K. The microwave frequency used is 15 GHz at 19 dBm nominal power at the source. We sweep the magnetic field from 0 Tesla to 9 Tesla initially to locate the narrow range of fields where interesting physics is observed,

and continue the experimental measurements in the narrow region of interest. We observe the two resonance signals. The signals are strong for both transmission and magnetoresistance. The left signal is low frequency excitation or left handed mode (LHM) and the right signal is Goldstone-like mode. The LHM signal in the transmission is about 1 mV, in the xy channel is about 10 μV, and in the xx channel is about 6 μV. The Goldstone-like mode signal amplitude in the transmission is about 0.4 mV, in the xy channel is about is about 2.3 μV, and in the xx channel is about 1.2 μV.

Temperature and microwave power dependence of the resonance signal

We are able to detect the magnetoresistive signals on both xx and xy channels. Now we would like to do further analysis of the signal as a function of the temperature and also the microwave power.

We look at amplitude of the antiferromagnetic resonance signal on the xx channel and xy channel. XX channel is the one along the probing current, and xy is the one transverse to the probing current. The magnetic field is within the device plane along the c-axis. We use the microwave of 15 GHz at 19 dBm nominal power at the source and a direct current of 1.5 mA. In Figure 5.15, we make a plot of amplitude of the MR-AFMR signal with varying microwave power on the left and temperature on the right. For the microwave power dependence, the power plotted on the x-axis is the calculated power in milliWatt at the coplanar waveguide. We observe that the amplitude grows linearly with microwave power. There is no non-linear behavior visible until 2 mW power, except some noisy behavior at very low power. This is expected because the signal to noise ratio is extremely low at very low power. Furthermore, for the temperature dependence, we observe that the

amplitude of the signal falls as we go higher in temperature. We can clearly see that the excitation amplitude is maximal at low temperature on both the xx and xy channels. This temperature dependence profile is consistent with observations made in the out-of-plane configuration, and the previously done studies [88, 100].

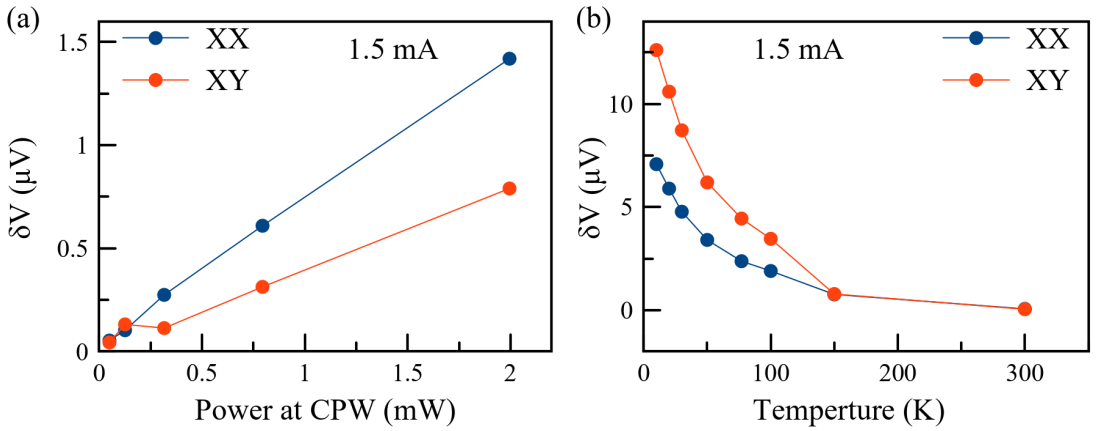

Figure 5.15: The dependence of magnetoresistive antiferromagnetic resonance (MR-AFMR) signal of bulk Cr2O3/Pt microstructure device of dimension 10 μm × 200 μm in the in-plane c-axis device. The external magnetic field is applied along the c-axis. The microwave current flows along the longitudinal (xx) channel. The xy is the transverse channel. (a) MR-AFMR signal amplitude of both xx and xy channels vs microwave power at the coplanar waveguide. Measured at 15 GHz, 1.5 mA DC and 50 K. (b) MR-AFMR signal amplitude of both xx and xy channels with varying temperature. Measured at 15 GHz, 10 dBm at source, and 1.5 mA direct current.

5.6.3 MR-AFMR conclusion and moving forward

We have successfully measured the antiferromagnetic resonance using magnetoresistive detection technique in bulk Cr2O3 and 5 nm Pt microstructure devices in both in-plane and out-of-plane c-axis of the crystal orientations. This is an important milestone to achieve. As opposed to inductive or spin pumping, magnetoresistive detection is inde-

pendent of the device size, so the proof of concept that the signal is detected using MR technique strengthens the possibilities to detect the resonance signal at nano-scale device using spin torque excitation technique. It helped us pave the path towards antiferromagnet based spintronic devices at nanoscale. The next section discusses the spin torque antiferromagnetic resonances.

5.7 Spin torque antiferromagnetic resonance (ST-AFMR)

After the successful detection of antiferromagnetic resonance using magnetoresistive detection technique, I present the experiment performed to study the resonances in antiferromagnet with a thin layer of non-magnetic heavy metal in a nano and microscale devices due to the spin torque excitation [101, 102] and magneto-resistive detection technique as mentioned in section 5.4. I evaluate the resonance behavior as a function of microwave power, DC current, temperature, and crystallographic orientations. For the in-plane configuration, as a part of detailed analysis of the origin of the resonance signal, I perform the angular dependence measurements of the signal. In addition, I analyze the spin-flop transition amplitudes as a function of DC current density, microwave power, temperatures, and angles between the microwave current and the external field.

5.7.1 ST-AFMR in a nano-cross device, out-of-plane Cr2O3/Pt

In this section, I present my experimental results of the spin torque induced antiferromagnetic resonance in the bulk Cr2O3 (0001) plane that has the c-axis perpendicular to the device plane. The 5 nm of platinum on the top surface acts as a conducting sur-

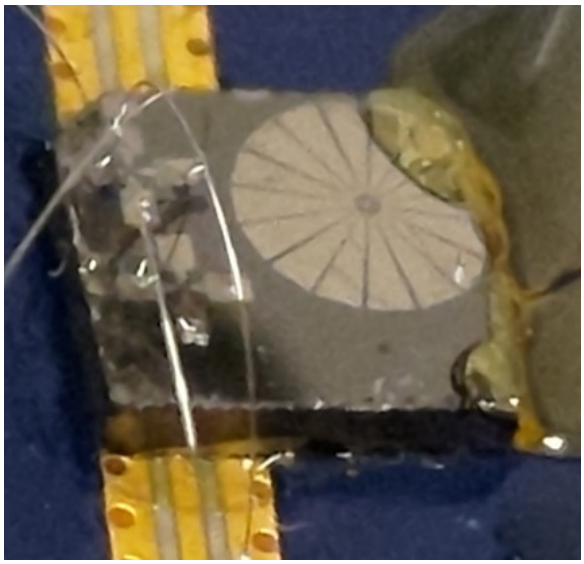

Figure 5.16: Image of the bulk Cr2O3/Pt nano-cross device sitting on the sample holder. The device is wirebonded and ready for ST-AFMR measurement.

face. I prepared the device that is a nano-cross of dimension $200\,\text{nm} \times 10\,\mu\text{m}$. Figure 5.16 is an image of the nano-cross device that is wirebonded and ready to be measured. The device with the microwave current is longitudinal (xx) channel, and the transverse device is xy channel. I would like to mention that the transverse channel has microwave detection region of $200\,\text{nm} \times 200\,\text{nm}$ area. We apply the magnetic field along the c-axis that is perpendicular to the device plane. We excite the magnon modes [103] by spin torque and Oersted field. We do simultaneous detection of the resonance signals on both xx and xy channels. The resonantly precessing spin wave modes in the antiferromagnetic layer induce the resistance oscillations in the non-magnetic layer. These resistance oscillations couple with the microwave current, and generate the rectified voltage signal. The signal is then feed into the low frequency signal pre-amplifier; the pre-amplified signal is measured with

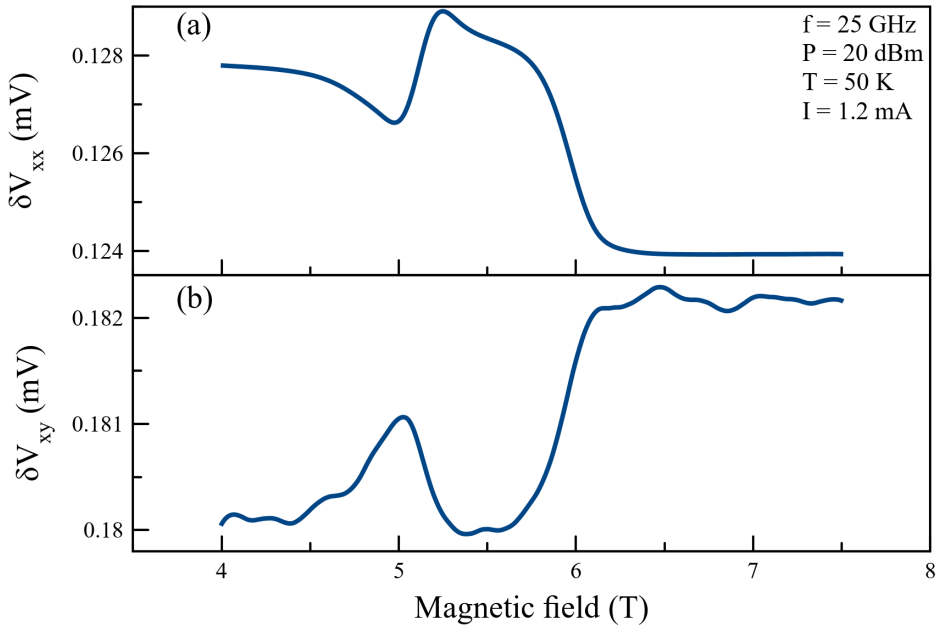

Figure 5.17: The ST-AFMR signal of a bulk Cr2O3/Pt nanocross device of dimension 200 nm × 10 μm in the out-of-plane c-axis device. The resonance signal is measured at microwave current of 25 GHz with 20 dBm nominal power at the source, 1.2 mA direct current. The measurement is carried out at 50 K. (a) Resonance signal amplitude of channel xx. This is also the longitudinal channel where microwave current flows. (b) Resonance signal amplitude of channel xy. This is the transverse channel in the nanocross device.

the lock-in amplifier. The pulsed microwave modulation frequency of 400 Hz square wave is used as a reference frequency for the lock-in amplifier.

The measurement is performed at a direct current of 1.2 mA at 50 K. The microwave frequency is 25 GHz and the microwave power is 20 dBm nominal at the source. We sweep the magnetic field from 0 Tesla to 9 Tesla initially to locate the narrow range of fields where interesting physics is observed, and continue the experimental measurements in the narrow region of interest. Figure 5.17 (a) and (b) are the plots of the ST-AFMR mea-

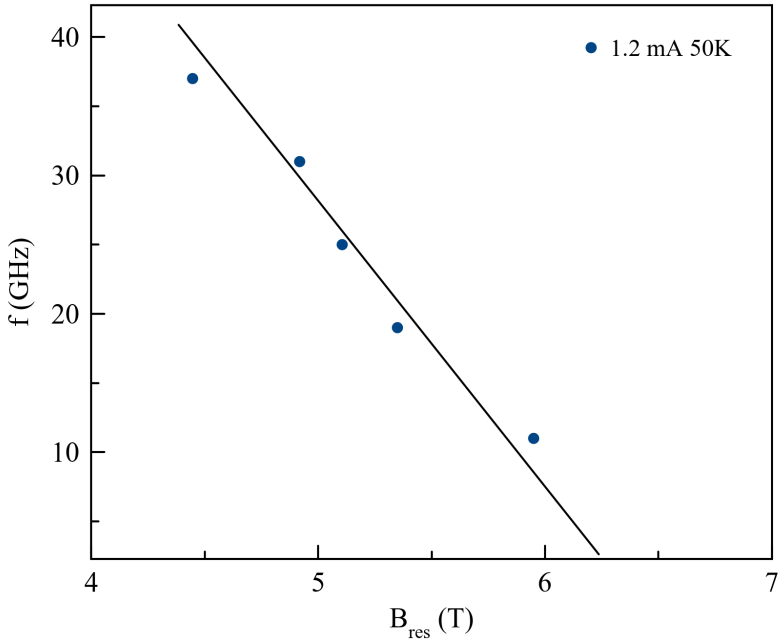

Figure 5.18: The frequency vs resonant field plot for longitudinal channel on a bulk Cr2O3/Pt nanocross device of dimension 200 nm × 10 μm in the out-of-plane c-axis device. The resonance signal is measured at 20 dBm nominal power at the source, 1.2 mA direct current. The measurement is carried out at 50 K.

surements for longitudinal (xx) and transverse (xy) channels respectively. The resonance signals are observed on both xx and xy channels. The xx channel has the active detection region of 200 nm × 10 μm, and xy channel has the active detection region of 200 nm × 200 nm. xx channel resonance signal amplitude is about 2 μV, and xy channel signal amplitude is about 1 μV. The observed resonances on both xx and xy channels are left-handed mode. This can be confirmed by looking at the frequency vs resonant field plot in Figure 5.18, which is plotted for the xx channel. Figure 5.18 correlates to the left-handed antiferromagnetic resonance modes that I presented in Figures 5.1 and 5.2. We also observe the spin flop at around 6 T. The spin flop jump voltage is about 4 μV in the xx channel, and about 2 μV in the xy channel.

Microwave power, temperature, and direct current dependence of the ST-AFMR signal, out-of-plane nano-cross Cr2O3/Pt device

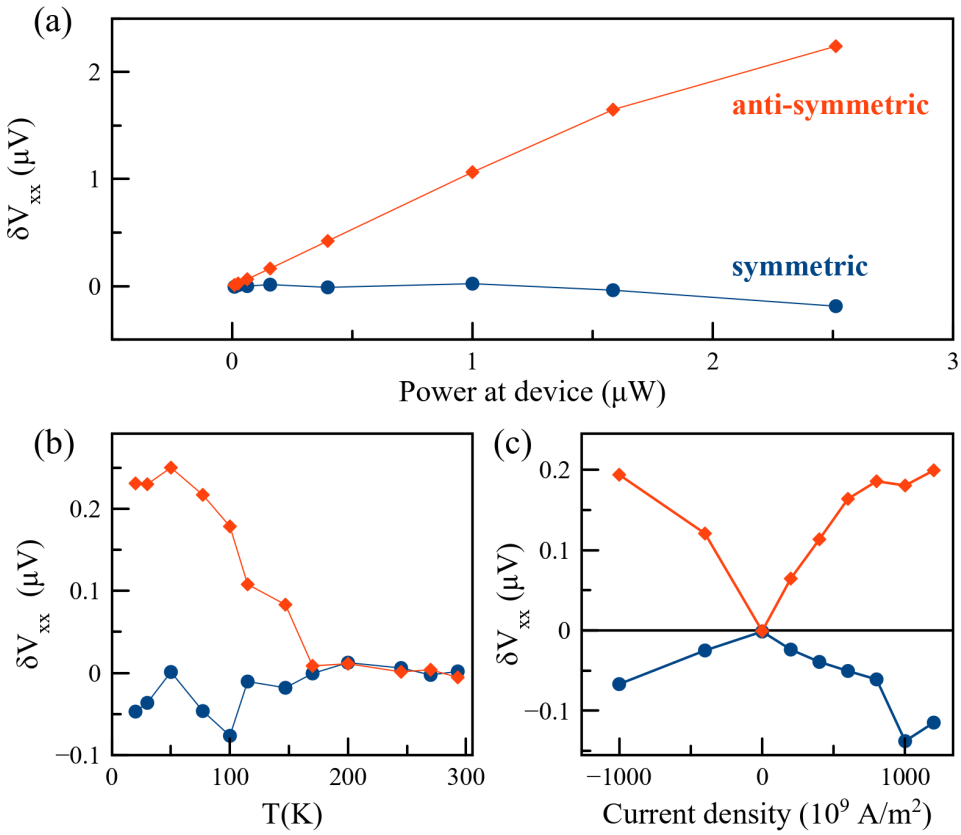

Figure 5.19: The dependence of ST-AFMR signal of bulk Cr2O3/Pt nanocross device of dimension 200 nm × 10 μm out-of-plane c-axis with: (a) Resonance signal amplitude with microwave power at the device. Measured at 25 GHz, 1.2 mA DC and 50 K. (b) Resonance signal amplitude with varying temperature. Measured at 25 GHz, 10dBm at source, and 1.2 mA DC. (c) Resonance signal amplitude with varying direct current density. Measured at 25 GHz, 10 dBm at source, and 50 K.

We are able to detect the ST-AFMR signal on a nanodevice. Now I further analyze the signal as a function of the microwave power, temperature, and direct current.

We look at amplitude of the antiferromagnetic resonance signal on the xx channel. XX channel is the one along the microwave current. The external magnetic field is applied

along the c-axis and perpendicular to the device plane. We use the microwave of 25 GHz at 19 dBm nominal power at the source and a direct current of 1.2 mA. Figure 5.19 (a,b,c) shows the plot for the ST-AFMR signal strength with varying microwave power at the device, temperature, and direct current density respectively. For the microwave power dependence, the power plotted on the x-axis is the calculated power in microWatt at the device. We observe that the symmetric component signal is small. For anti-symmetric component, the signal grows linearly with power. There is no non-linear behavior visible until 1.5 μW power; after this the non-linear effect may have come into effect. This can be expected as the heating effect from the microwave power become more prominent at higher power. For the temperature dependence, we observe that the signal for anti-symmetric component falls as we go higher in temperature. The amplitude is maximal at low temperature; the signal becomes very weak above 150 K. The symmetric component of the signal is small. For the direct current density dependence, we observe the signal for both anti-symmetric and symmetric component. The anti-symmetric component signal amplitude is stronger. The signal shows a linear behavior in the beginning, and it shows some non linear effect at higher current density. The non linear effect may have originated from the heating by the current. We also perform the measurement with negative current. The data is similar to the positive current.

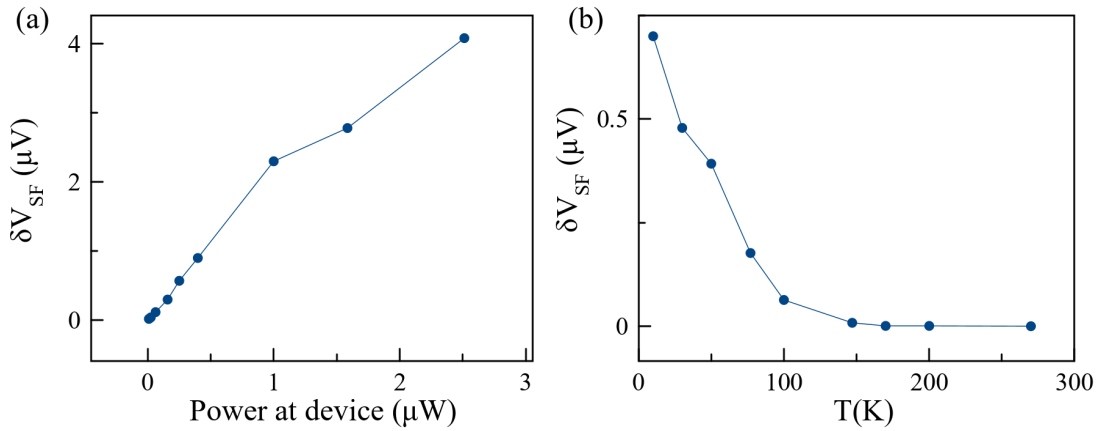

Figure 5.20: The dependence of spin flop voltage signal of bulk Cr2O3/Pt nanocross device of dimension 200 nm × 10 μm in the out-of-plane c-axis device: (a) spin flop voltage signal amplitude with microwave power at the device. Measured at 25 GHz, 1.2 mA DC and 50 K, and (b) spin flop voltage signal amplitude with varying temperature. Measured at 25 GHz, 10dBm at source, and 1.2 mA DC.

AFMR Spin-Flop signal analysis

If we look at the ST-AFMR signal in figure 5.17, we see a substantial amount of spin flop transition voltage. I would like to present some analysis of the spin flop voltage signal as a function of microwave power at the device, and temperature.

Figure 5.20 shows the amplitude of the spin flop for the xx channel with varying the microwave power at the device (left) and temperature (right). For the microwave power dependence, the power plotted on the x-axis is the calculated power in microWatt. We observe that the amplitude of the spin flop signal grows linearly with power. For the temperature dependence, we observe that the signal falls as we go higher in temeprature. The amplitude is maximum at low temperature; the signal becomes very weak at around 150 K.

Resistance and magnetoresistance of a nanodevice

I measure the resistance of a nanowire at 200 K. Figure 5.21 (a) is a plot of resistance vs probing current density. The measurements are taken in the presence of various external magnetic fields. A field at -4 T is below the spin flop region, and -9 T is above the spin flop region. I have also performed the measurements for negative current. The resistance and current dependence is consistent and show no abnormalities.

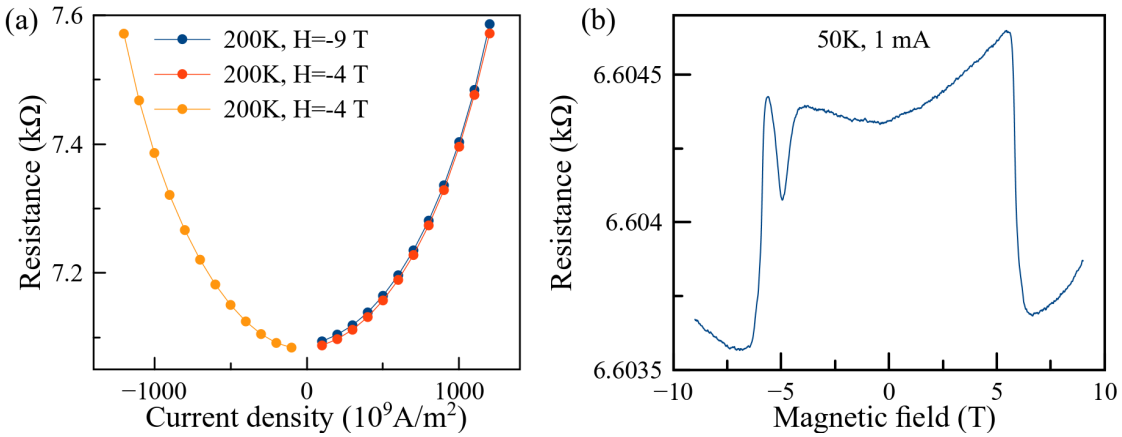

Figure 5.21: (a) Electrical resistance vs current density of a nanocross device measured at 200 K. The measurement is done at positive and negative current at -4 T, and only at positive current at -9 T. A field at -4 T is below the spin flop and a field at -9 T is above the spin flop. (b) Magnetoresistance measurement of a nanocross device measured at 50 K. 1 mA direct current is used.

I also perform the magnetoresistance measurement of the nanowire at 1 mA direct current at 50 K. The measurement is done in the absence of microwave current. I vary the magnetic field at the rate of 100 Oe/sec from +9 T to -9 T and measure the electrical resistance. Figure 5.21 (b) is the spectrum of the magnetoresistance. The spectrum shows

asymmetric behavior between the spin flop at the positive and negative field. This may be due to misalignment of the c-axis & external magnetic field, and some surface effects.

5.7.2 ST-AFMR in a microwire, Cr2O3/Pt

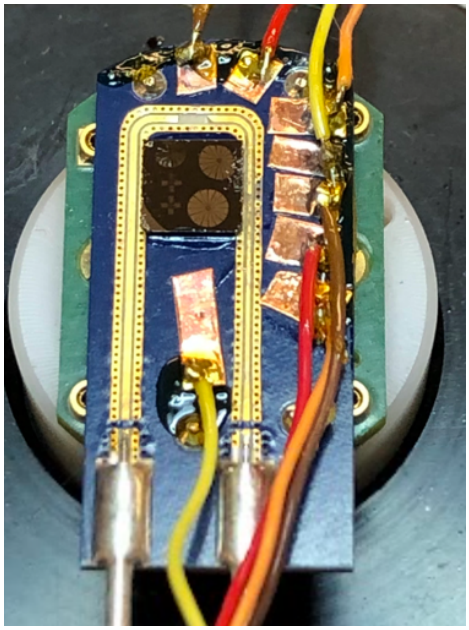

Figure 5.22: Microstructure wire (pizza-like device) of Cr2O3/Pt in-plane c-axis configuration ready for ST-AFMR measurements.

In the previous section, I presented the results of the ST-AFMR in a nanocross device. In this section, I would like to perform the detailed analysis of the spin torque induced resonances [101, 102] and present my experimental finding for the measurements carried out in the pizza-like microstructure ($10\,\mu$m $\times$ $200\,\mu$m) device. For this experiment, I use the bulk Cr2O3 (11-20) that has c-axis on the plane of the device. Figure 5.22 shows the photograph of the device. The device with the microwave current is xx channel, and the transverse device is the xy channel. The external magnetic field is applied along the c-axis in the device plane. The magnon modes are excited by spin torque and Oersted field. The spin

waves in the antiferromagnetic layer induce the resistance oscillations in the non-magnetic layer. This resistance oscillations couple with the microwave current and generates rectified voltage signal. The signal is then fed into the low frequency signal pre-amplifier; the pre-amplified signal is measured with the lock-in amplifier. The pulsed microwave modulation frequency of 400 Hz square wave is used as a reference frequency for the lock-in amplifier.

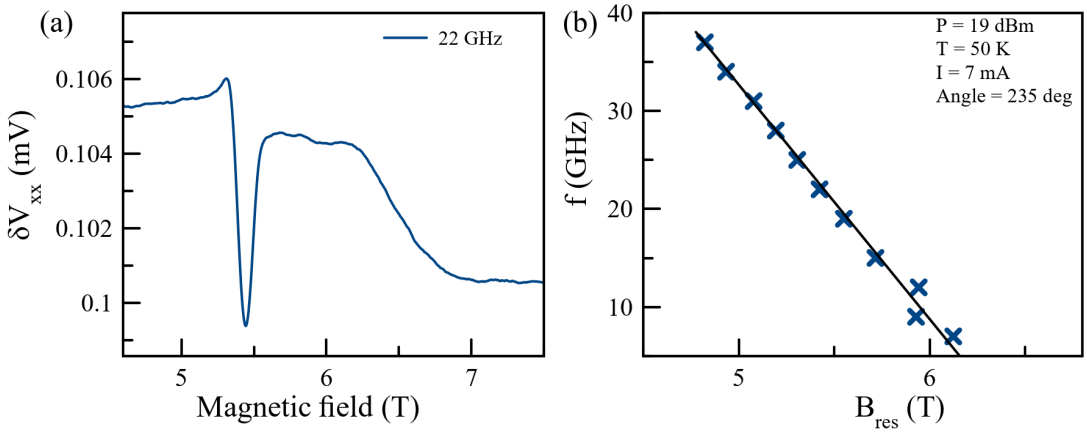

Figure 5.23: The ST-AFMR signal of a bulk Cr2O3/Pt microstructure pizza-like device of dimension 10 μm $\times$ 200 μm in the in-plane c-axis device, with external magnetic field along the c-axis. The resonance signal is measured at microwave current of 22 GHz with 19 dBm nominal power at the source, and 7.0 mA direct current. The measurement is carried out at 50 K. The angle between the c-axis and the microwave current flow (xx) channel is 235 degree. (a) Resonance signal amplitude of channel xx. (b) Frequency vs resonant field relation plot for the left handed mode.

Figure 5.23 (a) is a plot for a single ST-AFMR measurement spectrum for the xx channel. The measurement is performed at a direct current of 7.0 mA at 50 K. The microwave frequency used is 22 GHz with 19 dBm nominal value of microwave power at the source. The magnetic field is swept from 0 T to 9 T initially to locate the narrow range of fields where interesting physics is observed, and continue the experimental measurements

in the narrow region of interest. We observe the resonance signal by varying the external magnetic field. The resonance signal observed is clearly visible with an amplitude of about $6\,\mu$V. The resonance field is around 5 T. We also observe the spin flop region slightly above 6 T. The spin flop amplitude is about $3.7\,\mu$V. Figure 5.23 (b) is the frequency vs magnetic field plot for the ST-AFMR measurements. We can compare Figure 5.23 (b) with Figure 5.2 and confirm that the resonance mode is a left handed mode.

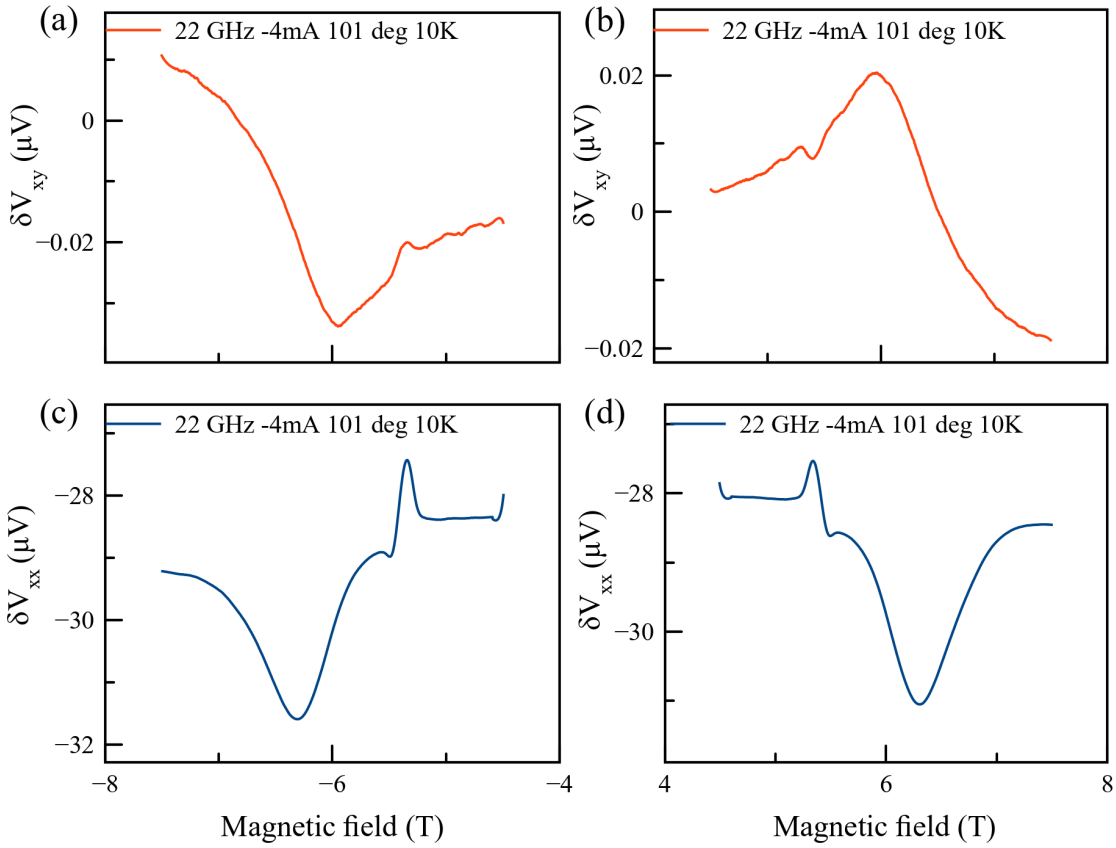

Figure 5.24: The ST-AFMR signal of a bulk Cr2O3/Pt microstructure pizza-like device of dimension 10 μm × 200 μm in the in-plane c-axis device. The resonance signal is measured at microwave current of 22 GHz with 19 dBm nominal power at the source, and -4.0 mA direct current. The measurement is carried out at 10 K. The angle between the c-axis and the microwave current flow (xx) channel is 101 degree. xy is the transverse channel (a) ST-AFMR signal amplitude of xy channel at negative field. (b) ST-AFMR signal amplitude of xy channel at positive field. (c) ST-AFMR signal amplitude of xx channel at negative field. (d) ST-AFMR signal amplitude of xx channel at positive field.

Figure 5.24 show the plots of ST-AFMR measurements taken for xx and xy channels for both polarities of external magnetic field at -4 mA direct current at 10 K. The resonance signals are clearly visible in both xx and xy channels for both field polarities. The resonance signal amplitude in xy channel for both field polarities is very small; the resonance signal amplitude in xx channel for both field polarities is about 1.5 μV. We also

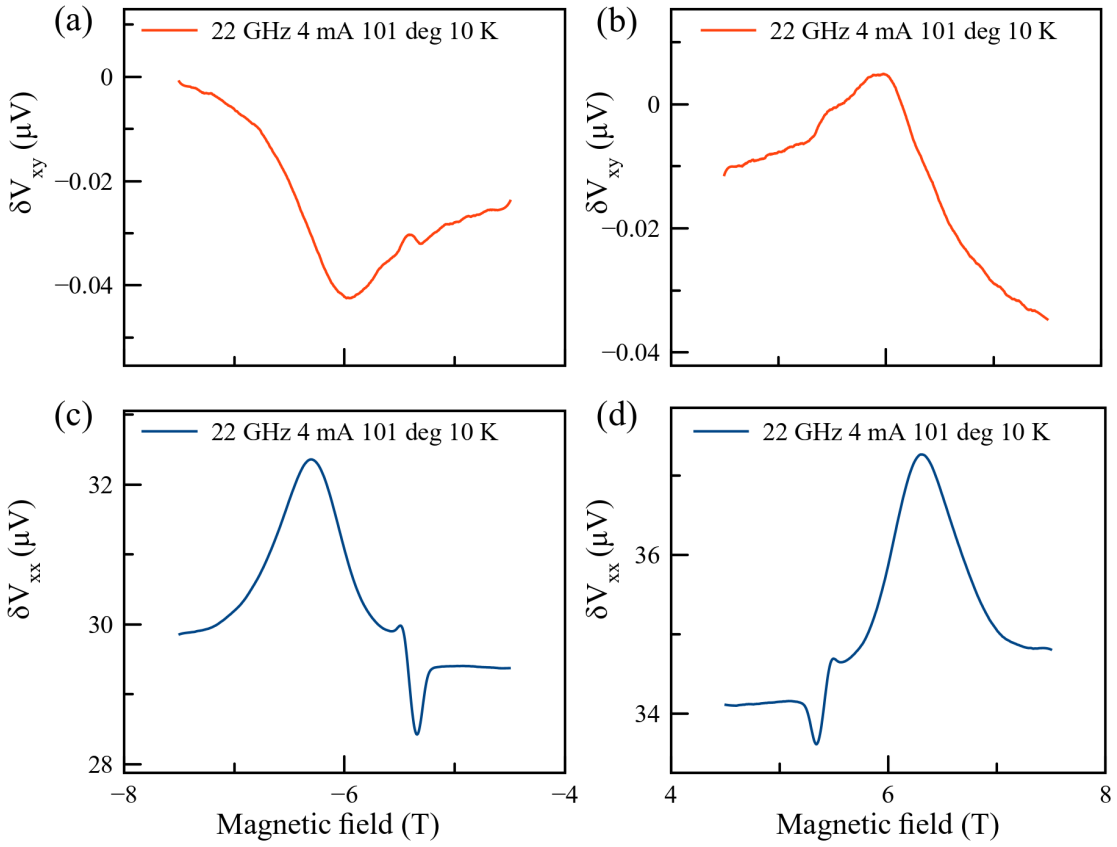

Figure 5.25: The ST-AFMR signal of a bulk Cr2O3/Pt microstructure pizza-like device of dimension 10 μm × 200 μm in the in-plane c-axis device. The resonance signal is measured at microwave current of 22 GHz with 19 dBm nominal power at the source, and 4.0 mA direct current. The measurement is carried out at 10 K. The angle between the c-axis and the microwave current flow (xx) channel is 101 degree. xy is the transverse channel (a) ST-AFMR signal amplitude of xy channel at negative field. (b) ST-AFMR signal amplitude of xy channel at positive field. (c) ST-AFMR signal amplitude of xx channel at negative field. (d) ST-AFMR signal amplitude of xx channel at positive field.

observe a big dip around spin-flop region. As we go higher in temperature, the dip disappears and it becomes just a steep fall without the dip, like in Figure 5.23 (a).

Figure 5.25 shows the plots of ST-AFMR measurements taken for xx and xy channels for both polarities of external magnetic field at 4 mA direct current at 10 K. The resonance signals are clearly visible in both xx and xy channels for both field polarities.

The resonance signal amplitude in xy channel for both field polarities is very small. Comparing the resonances in Figures 5.24 and 5.25, the signal strengths are very similar in both cases. The xx-channel signal retains its sign under reversing the magnetic field polarity, and changes the sign under reversing the direct current polarity. However, the xy-channel signal retains its sign under reversing the direct current polarity, and changes the sign under reversing magnetic field polarity.

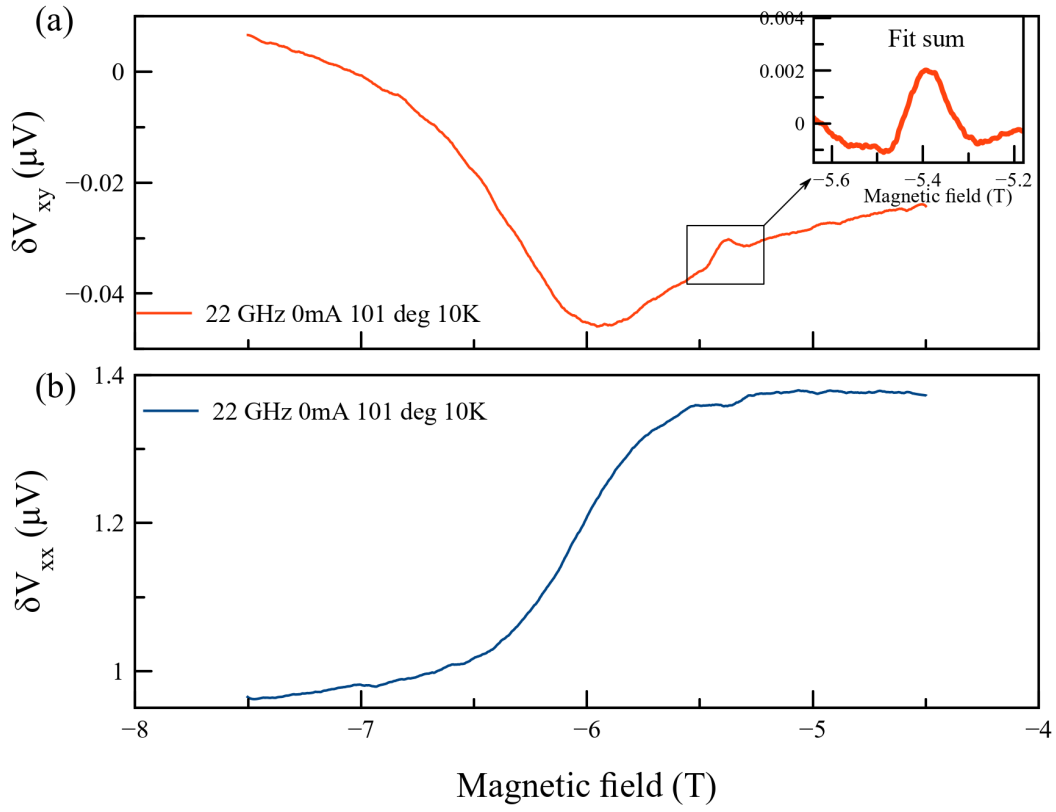

Figure 5.26: The ST-AFMR signal of a bulk Cr2O3/Pt microstructure pizza-like device of dimension 10 μm × 200 μm in the in-plane c-axis device at zero direct current, and 22 GHz with 19 dBm microwave current. The measurement is carried out at 10 K. The angle between the c-axis and the microwave current flow (xx) channel is 101 degree. xy is the transverse channel (a) ST-AFMR signal amplitude of transverse (xy) channel at negative field. (b) ST-AFMR signal amplitude of longitudinal (xx) channel at negative field.

Figure 5.26 shows the plots of ST-AFMR signal at zero direct current. When we use direct current, our signals have the contribution from both photo-voltage and photo-resistance effect. The zero direct current would only have the rectification effect. We observe the signal from rectification on both channels: xx and xy. The signals are visible; however, the resonance signal amplitudes are in the range of nanovolts. I will talk more about the photo-voltage and photo-resistance contributions during the angular dependence analysis of the resonances.

Direct current density, microwave power, and temperature dependence of the ST-AFMR signal, in-plane c-axis microwire

We are able to detect the ST-AFMR signal on a microstructure device with in-plane c-axis. We have the f-H plot and the single spectrum plot for both xx and xy channels at both polarities of the fields. Now I present further analysis of the resonance signal as a function of the direct current density, microwave power and temperature. The analysis is performed only on the longitudinal (xx) channel. The microwave current of 22 GHz at 19 dBm nominal power at the source is supplied along the xx channel. The external magnetic field is applied along the c-axis within the device plane.

In Figure 5.27: (a) is the plot of the resonance signal amplitude vs current density, (b) is the plot of resonance signal amplitude vs resonant field, and (c) is the plot of the resonance signal amplitude vs fine step current density. We observe the resonance signals for both symmetric and anti-symmetric component with varying current density. The

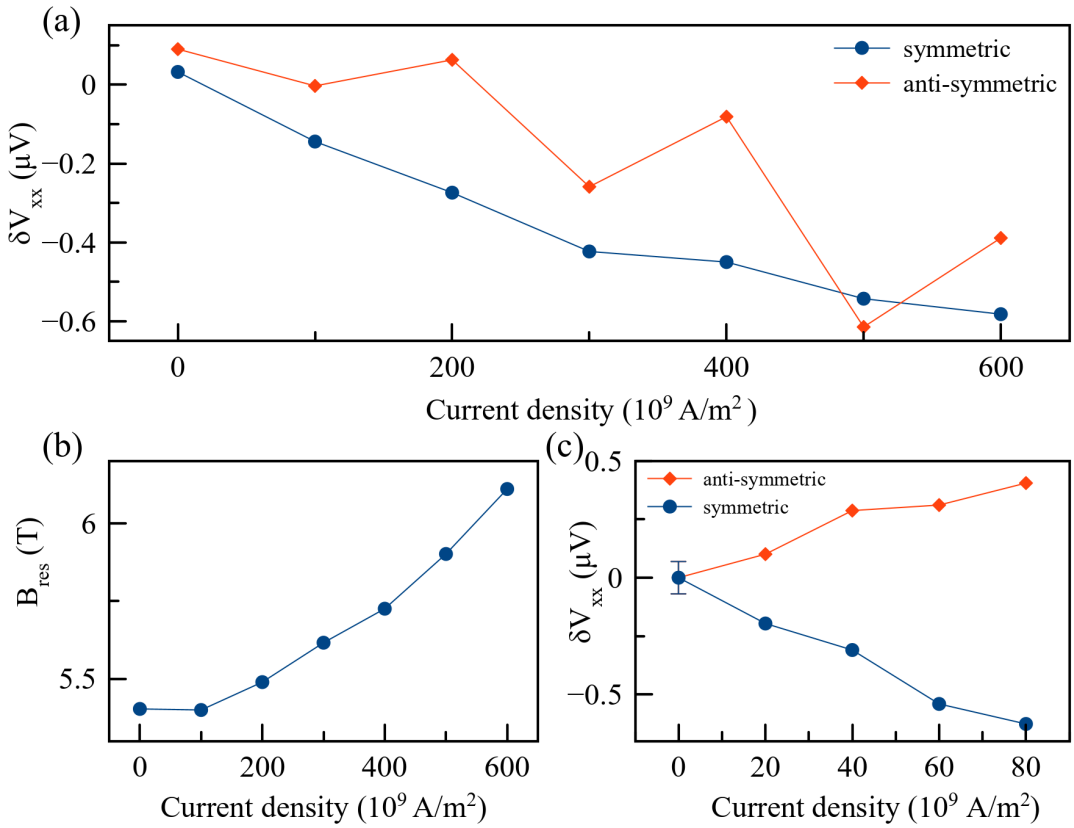

Figure 5.27: The current density dependence of ST-AFMR signal of bulk Cr2O3/Pt microstructure pizza-like device of dimension 10 μm × 200 μm in the in-plane c-axis device. The microwave current of 25 GHz with 19 dBm nominal power at the source flows through longitudinal (xx) channel. The angle between the xx channel and the c-axis is -33 degree. The measurement is carried out at 50 K. (a) Symmetric and anti-symmetric resonance signal amplitude with varying current density. (b) Resonance field with varying current density. (c) Symmetric and anti-symmetric resonance signal amplitude with varying direct current density with the current density values taken between the first and second point of figure a.

anti-symmetric component signals show some fluctuations and irregularities. The symmetric component signals have no irregular patterns; they show linear behavior until about 300 A/m^2. After this some non-linear effect starts to appear. Figure 5.27 (c) is a fine step measurement of the ST-AFMR signal with current dependence. We observe a linear dependence for both symmetric and anti-symmetric component signals. Figure 5.27 (b) represents

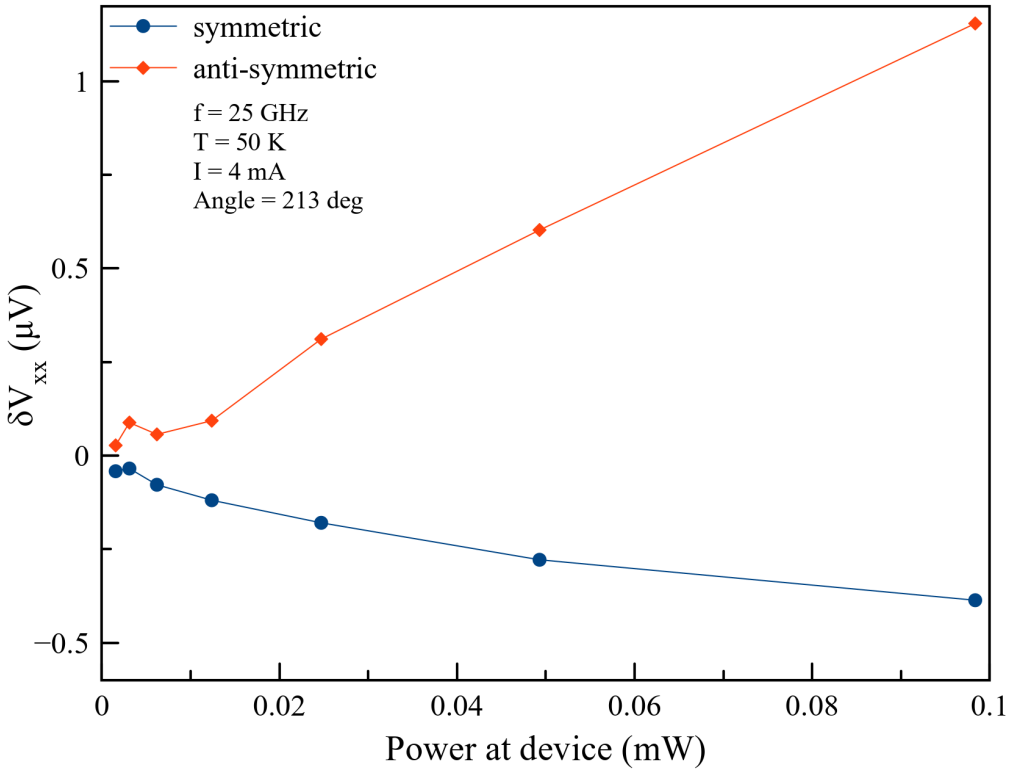

Figure 5.28: The plot shows the symmetric and anti-symmetric resonance signal amplitude with varying microwave power at the device in a bulk Cr2O3/Pt microstructure pizza-like device of dimension 10 μm × 200 μm with in-plane c-axis. The direct current of 4 mA and microwave current of 25 GHz flow through longitudinal (xx) channel. The angle between the xx channel and the c-axis is 213 degree. The measurement is carried out at 50 K.

the relation of the resonant field as a function of the applied current density. The applied current induces the heat on the surface and thus affects the resonant field non-linearly after a certain threshold current density.

Figure 5.28 is a plot for ST-AFMR signal with varying microwave power at a direct current of 4 mA. The power plotted on the x-axis is a calculated power at the device. We observe that the amplitude for both anti-symmetric and symmetric component of the signal grows linearly with power. There is no non-linear behavior visible for both components.

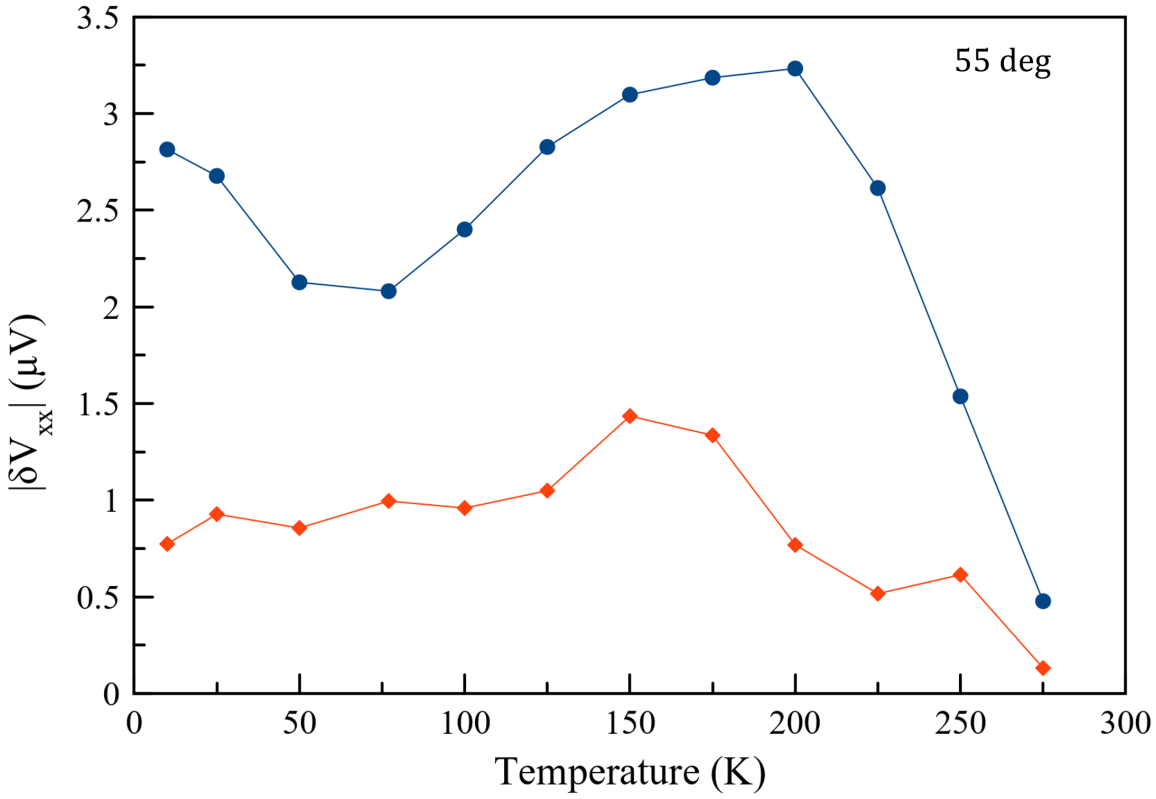

Figure 5.29: The plot shows the absolute values of symmetric and anti-symmetric resonance signal amplitude with varying temperature in a bulk Cr2O3/Pt microstructure pizza-like device of dimension 10 μm $\times$ 200 μm with in-plane c-axis. The direct current of 4 mA and microwave current of 25 GHz at 19 dBm nominal power at the source flow through longitudinal (xx) channel. The angle between xx channel and the c-axis is 55 degree. The measurement is carried out at 50 K.

Figure 5.29 is a plot for the temperature dependence of the absolute value of the ST-AFMR signals when the angle between the c-axis and the microwave current direction is 55 degree. We observe that the signal for anti-symmetric component is lower than the symmetric component. The signal amplitude is high at very low temperature; then we observe a dip in the signal. At around 200 K the signal picks up the maximum value before the amplitude starts to fall with a very high slope. The temperature dependence reflects a behavior with double peak.

AFMR Spin-Flop transition analysis, in-plane c-axis microwire

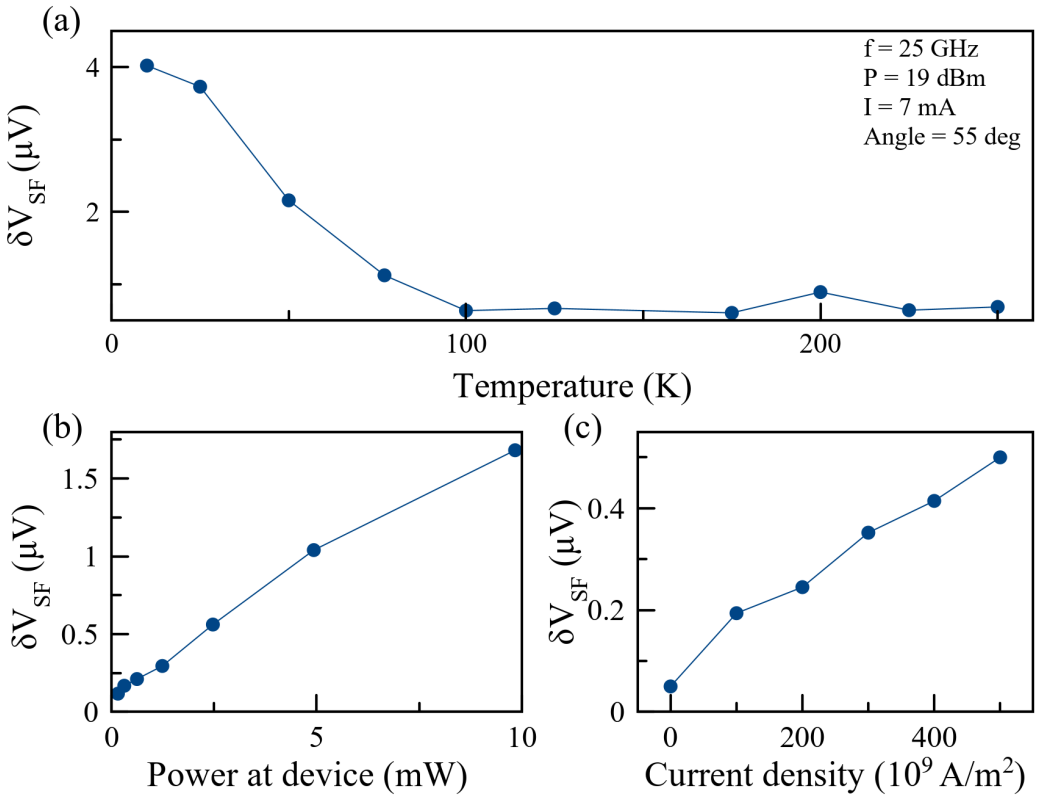

Figure 5.30: The dependence of spin flop signal amplitude of bulk Cr2O3/Pt microstructure pizza-like device of dimension 10 μm × 200 μm with in-plane c-axis. The microwave current of 25 GHz flows through longitudinal (xx) channel. The angle between xx channel and c-axis is 55 degree. (a) Spin flop signal amplitude with varying temperature. The direct current of 7 mA flows in the xx channel along with microwave current. (b) Spin flop signal amplitude with varying microwave power at the device at 50 K. The direct current of 7 mA flows in the xx channel. (c) Spin flop signal amplitude with varying current density at 50 K.

If we look at the ST-AFMR signal in Figure 5.23, we see a substantial amount of spin flop transition voltage. I would like to present the analysis of the spin flop voltage signals as a function of temperature, microwave power at the device, and direct current density.

Figure 5.30 shows the amplitude of the spin flop for the xx channel with varying temperature (a), the microwave power at the device (b) and direct current density (c). For the temperature dependence, we observe that the signal falls as we go higher in temperature. The spin flop signal amplitude is about 4 μV at 10 K. The amplitude is maximum at low temperature; the signal become very weak at around 100 K and stays low thereafter. For the microwave power dependence, the power plotted on the x-axis is the calculated power in milliWatt. We observe that the amplitude of the spin flop signal grows linearly with power, and the signal doesn't show any non-linear behavior. For the direct current density dependence, the spin flop voltage signal grows linearly with the current strength, and the signal doesn't show any nonlinear behavior that may originate from the heating effect.

Resistance and magnetoresistance measurements

Initially, I started out by measuring the electrical resistance of the microwire device as a function of applied direct current at 50 K. I also measured the electrical resistance as a function of temperature at 7 mA applied direct current. The resistance measured showed no abnormal behavior.

Then I proceed to perform the magneto-resistance measurements. The magnetic field is swept from -9 Tesla to +9 Tesla, and the electrical resistance of the microwire device is measured using the nano-voltmeter as a function of the applied external magnetic field. The measurement is carried out at 10 mA direct current at 50 K in the absence of the microwave current. The result is plotted in Figure 5.31 (a). We observe the peak at the spin flop transition field on both polarities of the magnetic field. Peaks at both field polarities look

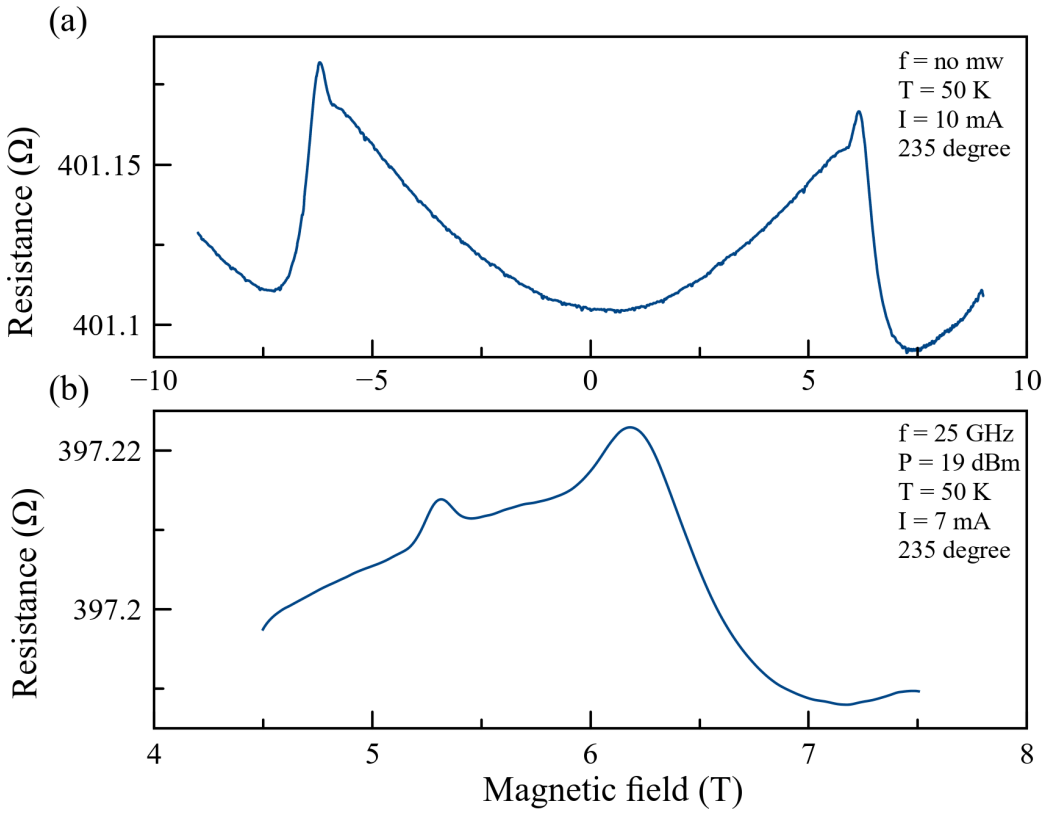

Figure 5.31: Magnetoresistance measurement of a bulk Cr2O3/Pt microstructure pizza-like device of dimension $10\,\mu\text{m} \times 200\,\mu\text{m}$ with in-plane c-axis. The direct current flows through the longitudinal (xx) channel. The angle between the xx channel and the c-axis is 235 degree. The measurement is carried out at 50 K. (a) Resistance vs magnetic field without the microwave current. The direct current of 10 mA is used. (b) Resistance vs magnetic field with the microwave current of 25 GHz and 19 dBm nominal power at the source. The direct current of 7 mA is used.

similar in behavior. The resistance level on different field polarities is slightly off. This may be coming from the device not being thermally stable. Waiting for longer time before starting the measurement might circumvent this issue.

I also perform the magnetoresistance measurement in the presence of the microwave current. The magnetic field is swept in a small region of field from +4.5 T to +7.5 T, and the resistance is measured with the nano-voltmeter. The measurement is car-

ried out at 7 mA direct current, 25 GHz microwave current, and 19 dBm microwave nominal power at the source at 50 K. In Figure 5.31 (b), we observe the peak at the spin flop transition. The spin flop behavior looks similar in both cases of with and without the microwave current. The left handed anti-ferromagnetic resonance peak is also observed at around 5.4 T in the presence of microwave current.

Angular dependence analysis and discussion of the photo-voltage and photo-resistance contribution

In this section, I present the experimental results performed in a microstructure wire of a pizza-device to study the spin torque antiferromagnetic resonance (ST-AFMR) signal as a function of the angle between the c-axis and the direction of the microwave current flow. The microwave current flows on the Pt layer that sits on the top of Cr2O3. This microwave current excites the magnon modes resonantly in the underlying Cr2O3 by spin torque and Oersted field. Experimental operating parameters are microwave frequency of 25 GHz, nominal power at the source of 19 dBm, temperature of 50 K, and a direct current of 4 mA. The external magnetic field is applied along the c-axis in the device plane. The resonance signal is pre-amplified before being collected with a lock-in amplifier. Figure 5.32 is the symmetric and anti-symmetric component of the ST-AFMR signal plotted with respect to the angle between c-axis (also the external magnetic field) and the direction of microwave current flow. The Oersted field contribution is the least when the microwave current flows perpendicular to the external magnetic field because the Oersted field oscillation is parallel to the external magnetic field. We observe that the signal amplitude is non-zero at around

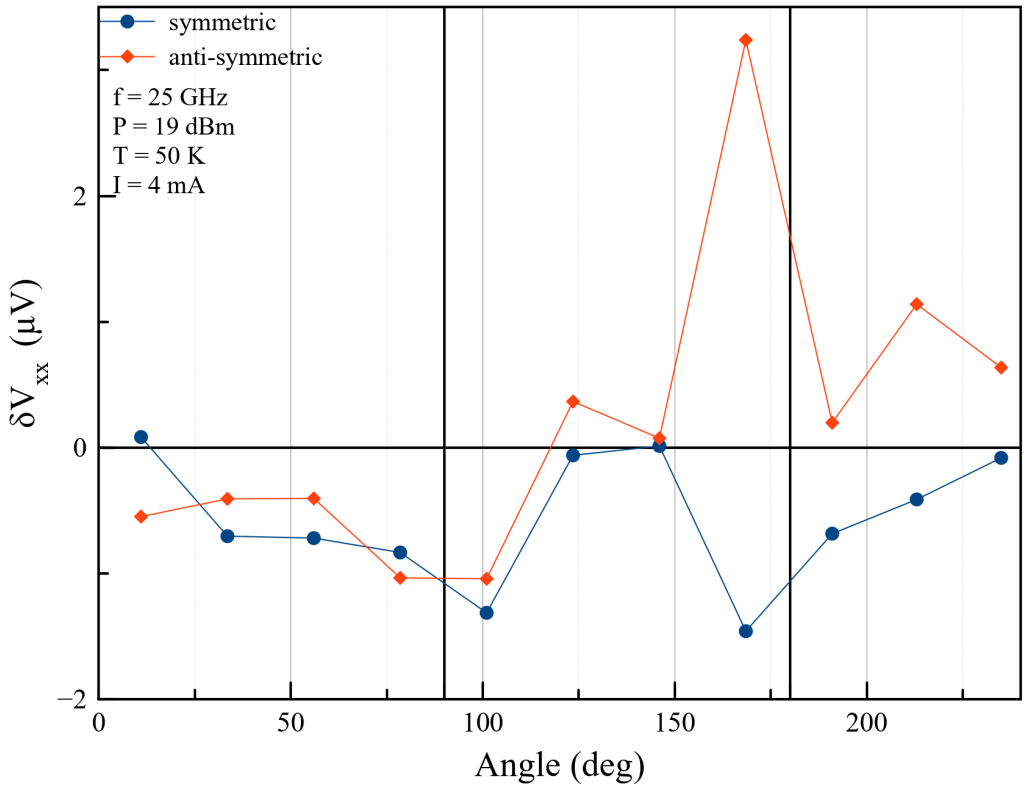

Figure 5.32: The plot shows the angular dependence of ST-AFMR signal of a bulk Cr2O3/Pt microstructure pizza-like device of dimension 10 μm × 200 μm with in-plane c-axis. The direct current of 4 mA, and microwave current of 25 GHz with 19 dBm nominal power at the source flow through the longitudinal (xx) channel of the device. The x-axis is the angle between xx channel and the c-axis. The measurement is carried out at 50 K.

90 degree. This may mean that the resonance signal has a non-zero contribution from the spin torque excitation.

By means of angular dependence measurement, I plan to differentiate the photo-voltage and photo-resistance contributions in the resonant signal. For each angle, I perform the direct current dependence measurement; I plot the resonance signal strength vs the applied direct current, and I fit the data with a straight line. From fitting, I extrapolate a slope and an intercept values. I repeat the measurements at different angles and collect

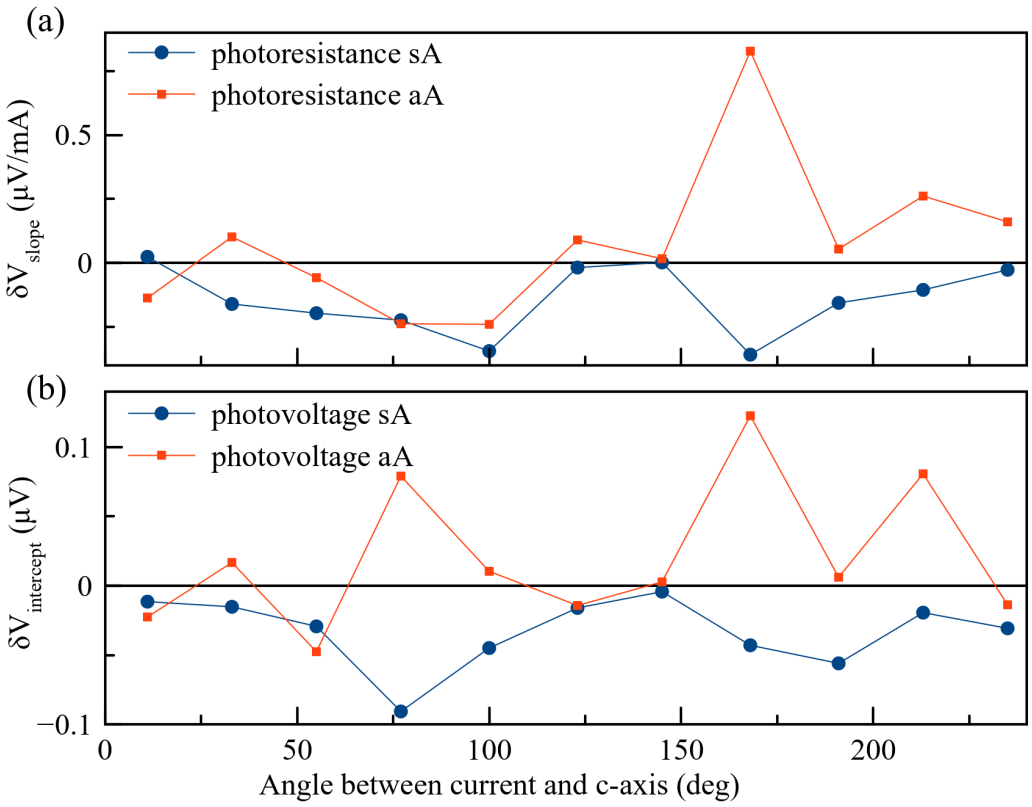

Figure 5.33: The angular dependence of the slope and intercept of ST-AFMR signal of a bulk Cr2O3/Pt microstructure pizza-like device of dimension 10 μm × 200 μm with in-plane c-axis at 50 K. The microwave current of 25 GHz with 19 dBm nominal power at the source flows through the longitudinal (xx) channel of the device. The angle on the x-axis of the plot is the angle between xx channel and the c-axis. At each angle, the current dependence measurement is performed. The ST-AFMR signal from the current dependence is plotted against each other and fitted with a straight line to extrapolate the values of the slope (δV_{slope}) and the intercept ($\delta V_{intercept}$). (a) The slope (δV_{slope}) vs angle between the microwave current flow (xx) channel and the c-axis. (b) The intercept ($\delta V_{intercept}$) vs angle between the microwave current flow (xx) channel and the c-axis.

the values of slope and intercept. In Figure 5.33, I plot δV_{slope} and $\delta V_{intercept}$ versus angle between the c-axis and the microwave current direction. The slope indicated the photo-resistance contribution, illustrating its linear relationship with DC current. Conversely, the intercept revealed the photo-voltage contribution, with a non-zero value indicating rectifi-

cation effects in the signal. The observed angular dependence highlighted the presence of rectification effects across various angles.

The angular dependence results (Figures 5.32 and 5.33) exhibit complex behavior. After each measurement at a specific angle, the sample was removed from the system, re-wire-bonded at a different angle, and then reinserted into the PPMS system. This process inevitably introduced misalignment between the crystal's c-axis and the external magnetic field. Such systematic errors have contributed to the observed complexity in the angular behavior, however, the overall trend remains clear – the spin waves are excited at angles with prohibitively small Oersted field contribution, thus necessitating the presence of spin torque.

Magnetostriction in Cr2O3: Discussion

The magnetostriction effect in Cr2O3 has been highlighted by Prof. Jing Shi. The deformation happens at the spin-flop field of about 6 Tesla and doesn't change above and below the spin flop field. The deformation along the axis parallel to c-axis is 2.8×10^{-5}, and along the axis perpendicular to the c-axis is -0.4×10^{-5}. The relative volume change is 2×10^{-5} [104].

In the spin flop jump, two oppositely oriented spins suddenly undergo a phase transition such that both the spins cant almost 90 degree from the c-axis. These two spins, however, are still facing away from each other. In Figure 5.23 (a), the spin flop jump may have been affected by the magnetostrictive effect. However, our ST-AFMR signal is the left hand mode that has the resonant field below the spin flop field. This resonantly excited mode precesses at a very small angle, perhaps 1 or 2 degree, which is

much less compared to the spin flop transition angle of about 90 degree. So, we could say that the magnetostriction has no or very minimal contribution (if any) for the left hand mode resonance signal. Besides, the resistance change by the deformation length of 0.28 micrometer only changes the resistance or voltage at less than a microvolt range. Our signal strength is stronger and in the range of 5-10 microvolt.

5.7.3 ST-AFMR in a microwire, Fe2O3/Pt

After exploring the spin dynamics in Cr2O3, we move our way towards Fe2O3. Fe2O3, commonly known as hematite, behaves as an antiferromagnet below the Néel temperature of around 950 K [105, 106]. In this section, I present the ST-AFMR experiments and results performed on Fe2O3 crystal with a thin layer of Platinum on the surface. Fe2O3 has no magnetostriction effect, so it would be a good comparison to observe the qualitative differences and similarities in the signals between Fe2O3 and Cr2O3. But first I would like to start with the fabrication process of the device.

Fabrication of Fe2O3/Pt microwire

The device for this experiment and study was fabricated and provided by Prof. Jing Shi's group. The following steps were used to prepare the device:

Sputter deposition: 5 nm of Pt film was deposited on top of the bulk Fe2O3. The film was deposited at room temperature using the magnetron sputtering with 4 mTorr of Ar gas pressure and 10^{-7} Torr of system base pressure. The deposition rate of Pt was 0.36 Å/sec at 18 Watts DC power.

Photo-lithography: The photolithography was performed after completing the standard cleaning procedure of the substrate. The substrate was pre-baked on the hotplate for 2 minutes at 110 °C to remove any organic solvent residues. The negative photoresist s-5214 was applied and spin coated at the rate of 4000 rpm for 45 seconds to receive a thickness of 1.3 μm. Then the resist was soft baked for 1 minute at 115 °C.

An optical mask was used to pattern the design. The mask was aligned with the substrate. The patterns were exposed for 10 seconds with "normal exposure" under the UV light. The substrate was baked again for 10 minutes at 110°C. Then the substrate were exposed for 3 minutes with "flood type exposure" under the UV light. The s-5214 resist becomes insoluble in the developer after exposure. The developing was done using AZ300 developer for 60 seconds.

Etching: After defining the patterns, the sample was ethched using the inductively coupled plasma universal etching system with vacuum load lock. Chlorine based gas was used for etching thin Pt metal. The 300 Watt RF system produces a high density, low-pressure, low energy inductively coupled plasma. The total time for etching was around 30 sec.

Measurements and results

In this section, I present the experimental results of the anti-ferromagnetic resonance measurements performed in the bulk Fe2O3 (10-10) plane that has the c-axis in the device plane. The 5 nm thin layer of Pt is fabricated on top of Fe2O3. The measured device is a Hall bar of dimension 250 μm $\times$ 2 mm. As discussed in section 5.4.3, I perform the measurements of the antiferromagnetic resonance by spin torque excitation and magnetore-

sistance detection technique. The device with the microwave current is our longitudinal (xx) channel, and the transverse device is the xy channel.

Case I: Microwave current is parallel to external magnetic field and the c-axis of the device

A schematic of the device with wiring and axes is presented in Figure 5.34 (a). We send the microwave current through the channel that is parallel to the c-axis. External magnetic field is applied along the c-axis that is within the device plane. The magnon modes are resonantly excited by spin torque and Oersted field. The resonantly precessing spin wave modes in the antiferromagnetic layer induce the resistance oscillations in the non magnetic layer. The resistance oscillations couple with the microwave current and generate the rectified voltage signal. The signal is then feed into a low frequency signal pre-amplifier; the pre-amplified signal is measured with lock-in amplifier. Pulsed microwave modulation frequency of 400 Hz square wave is used as a reference frequency for the lock-in amplifier.

The microwave frequency of 19 GHz is used with 19 dBm nominal power at the source. The measurement is carried out at a direct current of 3.5 mA at 50 K. The magnetic field is swept from 4.5 T to 7.5 T. Figure 5.34 (c) and (d) are the plots of the ST-AFMR measurements for the xx, and xy channels respectively. The resonance signal is observed on both xx and xy channels. The xy channel resonance signal is very weak. The xx channel resonance signal is clearly visible with the signal amplitude of about 0.1 μV. The resonance field observed for 19 GHz is about 5.5 T. We also observe the spin flop around 7 T. The spin flop jump voltage strength in the xx channel is about $0.6\,\mu V$. Figure 5.34 (b) shows

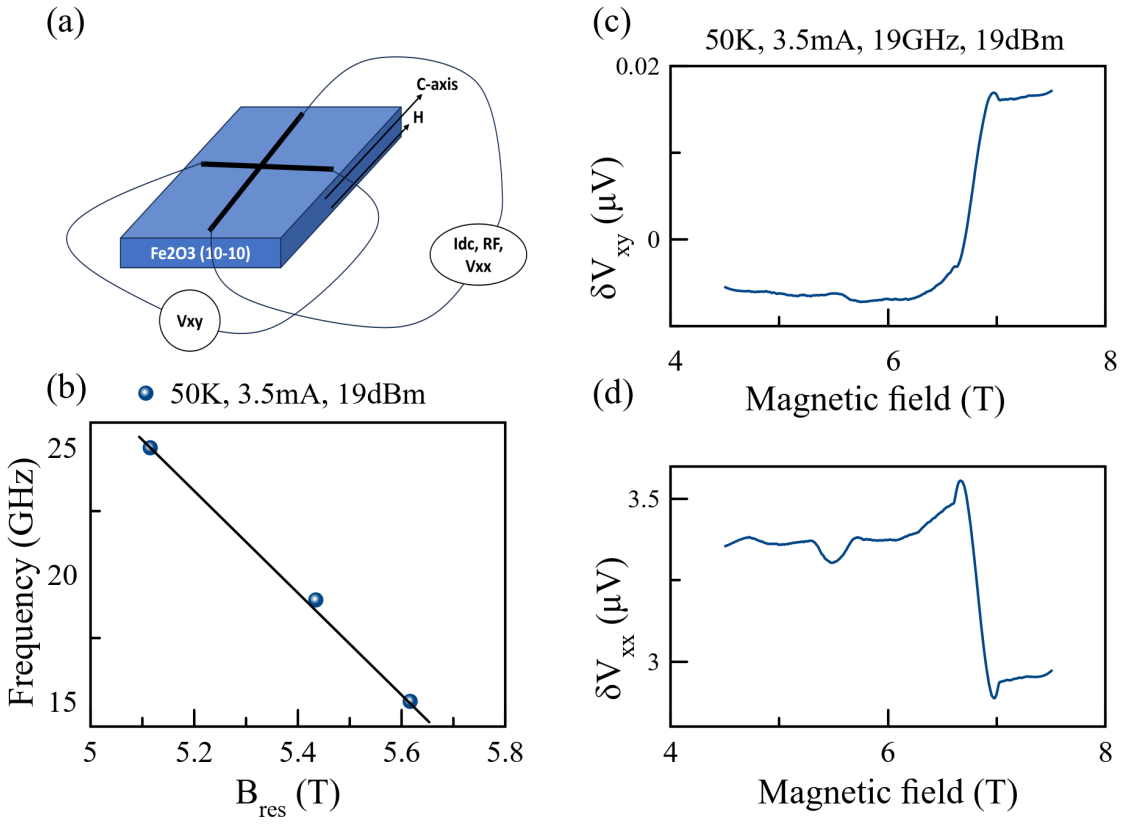

Figure 5.34: Case I: The microwave current of 19 GHz with 19 dBm nominal power at the source and direct current of 3.5 mA flow through longitudinal (xx) channel. The xx channel is parallel to the c-axis of the Fe2O3/Pt device. The magnetic field is applied parallel to the c-axis. The device is a Hall bar of dimension 250 μm $\times$ 2 mm. (a) Schematic of the Hall bar device and the electrical wiring. (b) Frequency vs resonant field plot of the resonance signal of the device. (c) Resonance signal amplitude of the transverse (xy) channel. (d) Resonance signal amplitude of the longitudinal (xx) channel.

the driving microwave frequency vs external magnetic field relation. This plot is consistent with the expected frequency vs magnetic field relation established in prior studies [107].

Case II: Microwave current is perpendicular to the external magnetic field and c-axis of the device

The schematic of the device with the wiring and the axes is presented in Figure 5.35 (a). We send the microwave current through the xx channel that is transverse to the c-axis. The

magnetic field is still applied along the c-axis. The magnon modes are resonantly excited by spin torque and Oersted field.

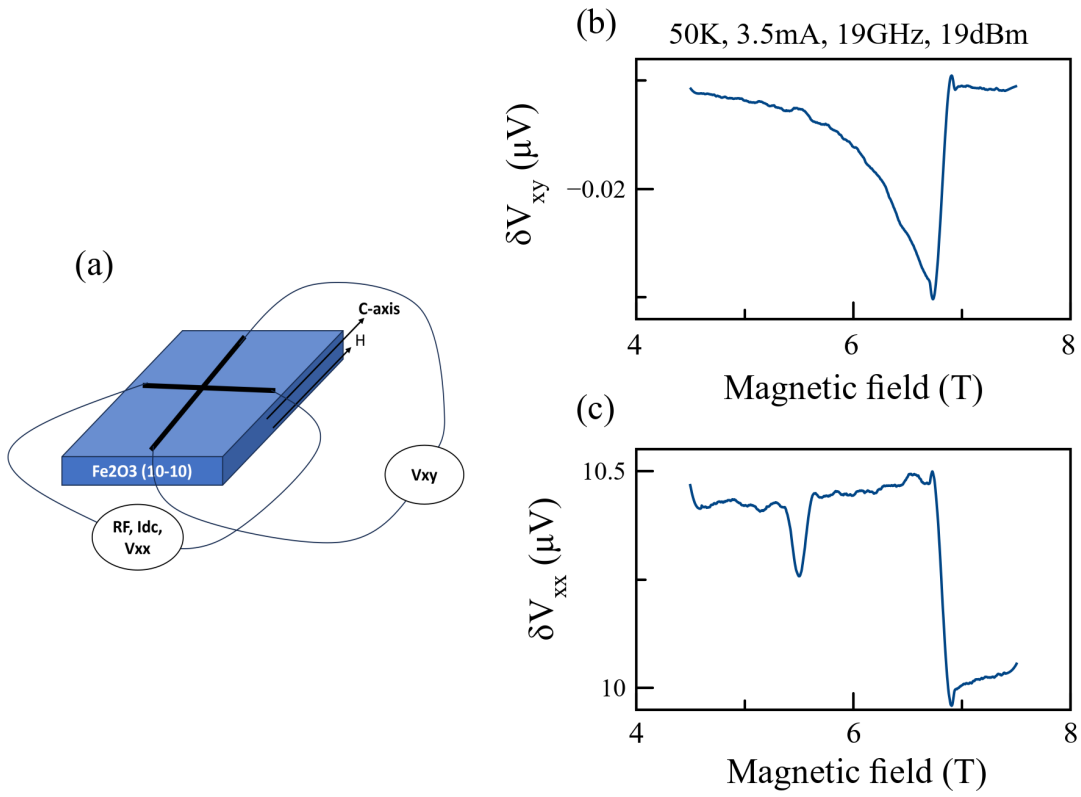

Figure 5.35: Case II: The microwave current of 19 GHz with 19 dBm nominal power at the source and direct current of 3.5 mA flow through longitudinal (xx) channel. The xx channel is perpendicular to the c-axis of the Fe2O3/Pt device. The magnetic field is applied parallel to the c-axis. The device is a Hall bar of dimension 250 μm $\times$ 2 mm. (a) Schematic of the Hall bar device and the electrical wiring. (b) Resonance signal amplitude of the transverse (xy) channel. (c) Resonance signal amplitude of the longitudinal (xx) channel.

In case II, the experimental parameters used are still the same as in case I: direct current of 3.5 mA, microwave current of 19 GHz at 19 dBm nominal power at the source, the temperature of 50 K, and 400 Hz microwave pulse modulation. The signal is collected with the lock-in amplifier. The field sweep region is 4.5 T to 7.5 T. Figure 5.35 (b) and (c) are the

plots of the ST-AFMR measurements for both xx and xy channels. The resonance signal is observed on both xx and xy channels. The xy channel resonance signal is very weak. The xx channel resonance signal is clearly visible with the signal amplitude of about $0.2\,\mu V$. The spin flop is also observed at around 7 T. The spin flop jump voltage strength is about $0.5\,\mu V$.

Discussion:

We are able to detect the resonance signal in Fe2O3/Pt device on both the cases: microwave current parallel to the c-axis and microwave current perpendicular to the c-axis. The measurement parameters used on both cases are same. The microwave current perpendicular to the c-axis has a better signal strength than the parallel case. When the microwave is supplied perpendicular to the c-axis (also perpendicular to the external field direction), it generates oscillating Oersted field that is parallel to the external magnetic field. When the high frequency (Oersted) field and external magnetic field are parallel we have the least contribution from the inductive excitation. However, we have the stronger signal strength when microwave is perpendicular to the c-axis. This may mean that the observed resonance signal have more contribution from the spin torque excitation than the Oersted excitation.

5.8 Summary and outlook

Following the popularity of antiferromagnets because of their robustness to external magnetic perturbation and high excitation frequency range, we pursue the study of coherent spin dynamics in the antiferromagnetic system and pave the way toward the applications of antiferromagnet based spintronic device at the nanoscale.

We start with the magnetoresistive detection of the antiferromagnetic resonance in the bulk Cr2O3 and 5 nm Pt microstructure devices in both in-plane and out-of-plane c-axis of the crystal orientations. After the successful detection of the AFMR signal using the magnetoresitive technique, we move our way toward the ST-AFMR at the nanoscale. We design and fabricate the nanodevice. We detect the ST-AFMR signal in the nanoscale device with the c-axis out-of-plane. The detected signal is clearly visible. Signals are present on both the xx (longitudinal) and xy (transverse) channels. For the purpose of detailed study, we fabricate the pizza structure device on the in-plane c-axis Cr2O3 crystal. We perform the angular dependence measurement, and we also perform the current dependence for each angle. This helped us discern the photo-voltage and photo-resistance contributions present in the signals.

We also do the ST-AFMR measurement in bulk Fe2O3 and 5 nm of Pt microstructure device with the in-plane c-axis. We observe the signal for both the xx (longitudinal) and xy (transverse) channels. Although the xy channel signal is weak, the xx channel signal is clearly visible. We found that the microwave current perpendicular to the c-axis has stronger signal than microwave current parallel to the c-axis. This may have suggested that the resonance signal may have been dominated by spin torque excitation rather than Oersted excitation.

Chapter 6

Development and adaptation of planar micro-resonator to boost inductive detection of antiferromagnetic spin dynamics

6.1 Motivation and introduction

The previous chapter demonstrates that we were able to achieve the milestone of electrical detection of antiferromagnetic resonance on laterally confined structures down to the nanoscale limit. The electrical detection method makes it possible to detect spin fluctuations in antiferromagnets independent of their thickness. Thus, electrical detection method applies to both thin films, and bulk crystals shown in the previous chapter, which

can be considered quasi-infinite in the vertical direction. Antiferromagnetic resonance in films has remained a significant challenge and hurdle to overcome for the advancement of the antiferromagnetic spintronics [108, 109]. Inductive measurements of AFMR on thin films are principally difficult since they require a substantial dynamics magnetic moment of the sample, which antiferromagnets generally lack. Moreover, antiferromagnetic thin films show complex, yet to be understood, structure-magnetism correlations that are likely to negatively affect our ability to detect and utilize antiferromagnetic resonance – that is until the structure-magnetism issues are resolved. While we commence our efforts to exploit electrical detection of AFMR in antiferromagnetic structures confined in all three dimensions – to ultimately work with a (quasi-) discrete AFM spin wave spectrum and to be able to inject substantial spin current densities – in parallel, another approach is needed that would significantly increase inductive detection capabilities.

Such an approach involves planar microwave micro-resonators [110, 111], which offer nearly ultimate detection sensitivity for micro- and nano-structures and should allow to compensate for antiferromagnet's low dynamics magnetic moment. Such resonators, as I will show, require multi-step device fabrication and a lot of effort. However, once proven successful, this approach offers big advantages [112, 113]. Primarily, micro- and nano-structures antiferromagnetic structures could be used with a secure inductive detective feedback and excitation technique. At the same time, the implementation of planar resonators allows for concurrent electrical detection and spin-current biasing of the sample. Moreover, implementation of planar resonator would potentially allow for exploration of possibilities for coupling of antiferromagnetic magnons with quantum-electrodynamics

circuits (cQED) for further translation of antiferromagnetic spintronics into the realm of hybrid quantum systems [114, 115].

We plan to use omega shaped planar micro-resonator with AFM micro-structure integrated on the resonator to increase the inductive detection capabilities. The measurement setting will also be optimized for electrical detection and spin current biasing with the electric circuitry fabricated within the substrate with the Cr2O3 micro-structure. If successful, we plan to use the large critical field superconducting material as a planar resonator with smaller dimensions AFM integrated together to explore the cavitronic effects of coupling/hybridization of magnons to resonator photons. But, first I will talk about the multi-step fabrication procedure.

6.2 Device and micro-resonator fabrication

This section talks about fabrication and preparation of the device and the omega shaped micro-resonator.

6.2.1 Device fabrication

Our choice of the device is a microstructure of Cr2O3 with a thin layer (5 nm) of Pt on the top. The device is fabricated using focused ion beam (FIB) system by our collaborator at Helmholtz-Zentrum Dresden-Rossendorf (HZDR) research laboratory in Germany .

A scanning electron microscopy is used to locate the specific site in the specimen for extraction. The identified site is precisely milled with a FIB system, and then extracted from the region with a micro-manipulator. The removed crystal part is transferred onto

the sapphire substrate. Figure 6.1 (a) is the optical microscopy image of the Cr2O3 crystal used for the sample extraction. Figure 6.1 (b) is the scanning electron microscopy image of the extracted sample after being transferred to the sapphire substrate.

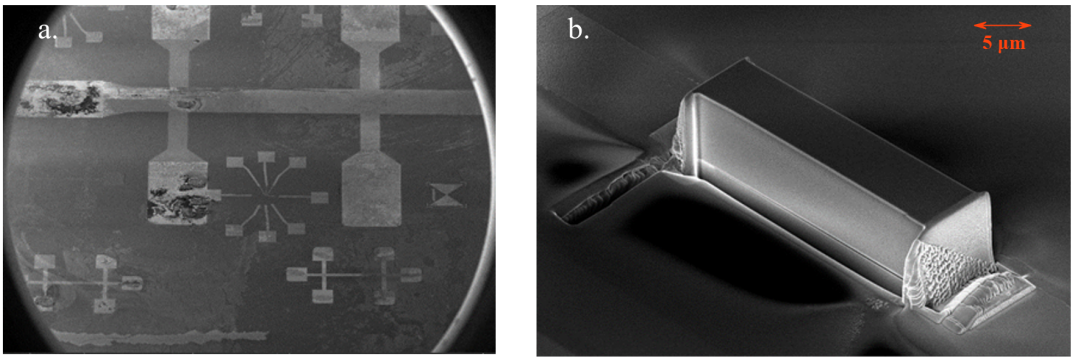

Figure 6.1: (a) The optical microscopy image of the Cr2O3 crystal. (b) The scanning electron microscopy image of the extracted piece.

6.2.2 Omega shaped planar micro-resonator fabrication

I fabricate the normal metal omega shaped planar micro-resonator on the m-plane (10-10) sapphire crystal substrate. The following procedures were followed:

Photomask: The photomask with omega pattern was designed and commercially fabricated. Figure 6.2 is the schematic of the omega resonator. The omega (Ω) shaped region is the active part. The active element is a micro coil that generates a strong and localized magnetic fields. A microscale or even nanoscale sample placed into the active area is excited by these fields. In resonance, the microwave is partially absorbed in the sample, and thus the microwave reflection coefficient from the micro-resonator changes.

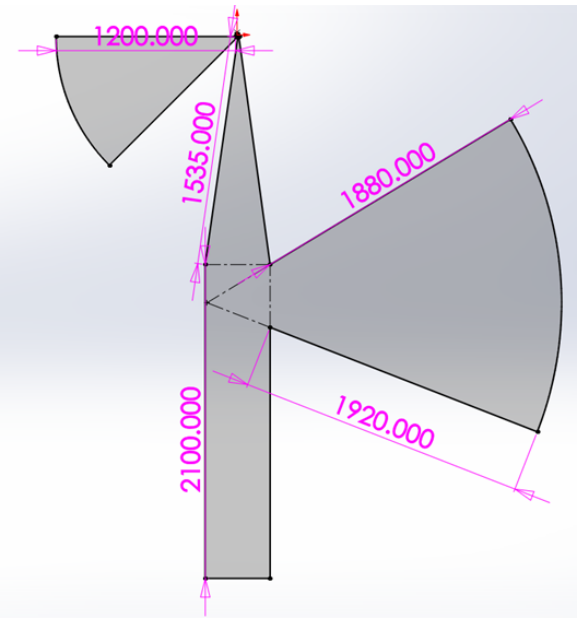

Figure 6.2: Schematic of the omega shaped planar microwave micro-resonator. The numbers represent the length in the units of micrometer.

Photolithography: The photolithography was performed after the standard cleaning procedure of the substrate with acetone, isopropanol, and DI-water. The substrate was pre-baked on the hot plate for 2 min at 180 °C. I applied the s-1813 positive photoresist on the substrate and spin coated at the rate of 4000 rpm for 45 sec to obtain the thickness of about 1.3 μm. After spin coating, the resist was soft baked for 1 min at 115 °C.

The negative mask was used. The patterns were exposed for 12 sec with "flood-type exposure" under the UV light. The s-1813 resist become soluble in the developer. The developing was done using the MIF-319 developer for 60 sec.

E-beam evaporation: The metallization of the resonator was done using e-beam evaporators of the Temescal BJD system with the system base pressure of about 2.6×10^{-6} Torr. Three layers of metals were deposited. The first layer contains Titanium (Ti) of 5 nm thickness, and acts as an adhesion layer for the next layer which is copper (Cu).

The copper was deposited around 400 nm in thickness. The capping layer of Gold (Au) was deposited to prevent the underlying layers from oxidation.

Lift off: The remaining resists and residues were cleaned using acetone.

6.2.3 Superconducting omega shaped planar micro-resonator fabrication

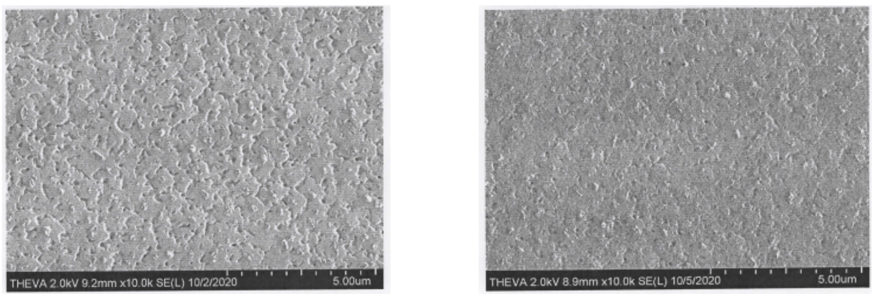

Figure 6.3: Scanning electron microscopy image of YBCO film. Image on the left is face 1 of the film and image on the right is face 2 of the film.

Alongside the normal metal planar micro-resonator, I also fabricate the superconducting planar micro-resonator for future use.

The resonant excitation of Cr2O3 spin dynamics at lower frequencies occurs at high magnetic field. So, micro-resonator fabricated from superconducting material must retain superconductivity at high field. Therefore, our choice of superconducting material is Yttrium Barium Copper Oxide (YBCO) because of its very high upper critical field of about 100 T. YBCO also has a critical temperature of around 88 K [116], which is above the boiling temperature of liquid nitrogen; thus, allowing a plenty of usefulness to the science research.

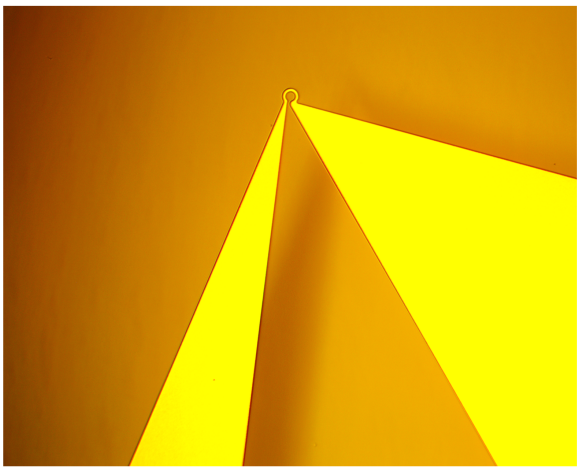

Figure 6.4: Optical microscopy image of superconducting omega shaped planar micro-resonator. The shiny region is the superconducting region that is sitting on sapphire (10-10) substrate.

YBCO/Au is sourced from Ceraco. Figure 6.3 is the scanning electron miscroscopy image of the YBCO film. It is polished on both sides. The film is on 10 mm $\times$ 10 mm Al2O3 wafer with a thickness of 0.5 mm. The sapphire substrate is m-plane (10-10). The thickness of YBCO film is 330 nm with 50 nm Au layer on top.

We carried out following steps to prepare the final resonator from YBCO/Au film:

Photolithography: The photolithography was performed like the one for normal metal planar resonator as we discussed above.

Etching: After the photolithography, the sample was ion-milled to etch the metal. Then the residue were cleaned with acetone. Figure 6.4 is the optical image of the superconducting omega shaped planar micro-resonator.

Figure 6.5: Measurement setup to characterize the eigen-frequency of omega shaped planar micro-resonator.

6.3 Eigen-frequency characterization of micro-resonator

After the device is fabricated, I perform the eigen-frequency characterization of the micro-resonator using the setup as shown in Figure 6.5. A microwave signal is sent through a directional coupler into the micro-resonator. The signal is partially reflected and diverted via the directional coupler into a microwave diode. The reflected signal magnitude is minimized when the microwave frequency matches the eigen-frequency of the omega resonator. The measurement was performed at room temperature (around 293 K) and low temperature (30 K). In Figure 6.6, it is observed that the eigen frequency is 5.84 GHz at 30 K, and 5.80 GHz at room temperature. The frequency shift between low temperature and room temperature is very small.

6.4 Integration of Cr2O3/Pt device with planar micro-resonator

Now that we have characterized the planar resonator, we would like to integrate the resonator and the device to make it ready for microwave spectroscopy measurements.

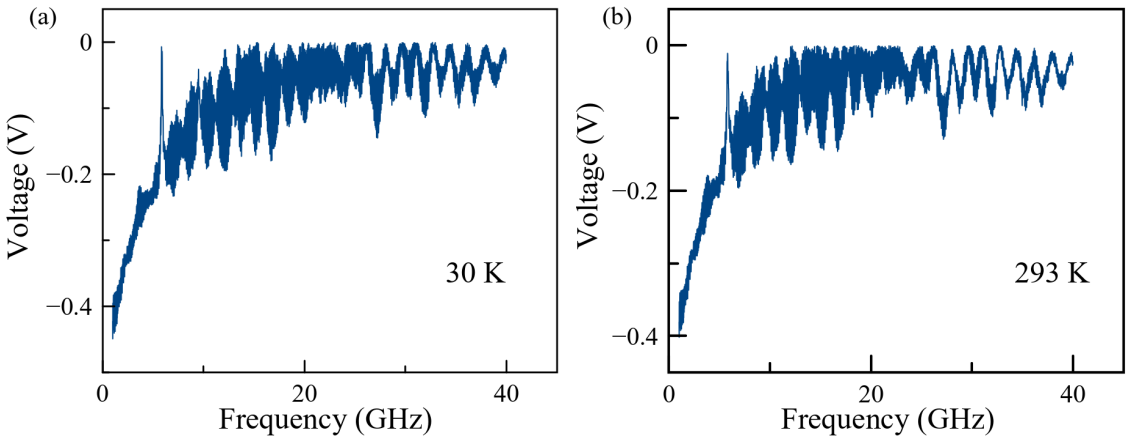

Figure 6.6: Reflected signal as a function of microwave frequency. A sharp inverted dip in the voltage signal is characterized as eigen-frequency of the measured omega shaped planar micro-resonator. (a) Measurement done at 30 K. (b) Measurement done at 293 K.

The integration of Cr2O3/Pt device on the non-superconducting planar resonator has been a very challenging task. The micro-structure of Cr2O3 is on one substrate and the planar resonator is on the other. The micro-structure needs to perfectly sit on the micro-coil in the resonator to feel the maximum strength of the high-frequency magnetic field. We flip one of the substrate over and position the Cr2O3 device and micro-coil located in the resonator. This procedure is carried out under the optical microscope. After trying for hours and multiple failed attempts, we finally were able to align the device and the micro-coil as shown in Figure 6.7.

6.5 Microwave spectroscopy: Results and discussion

Figure 6.8 is the integrated device of planar resonator and Cr2O3 that is ready to be measured. We perform microwave spectroscopy measurements at 30 K. We drive the external frequency of 5.86 GHz using the microwave source generator, microwave cable

Figure 6.7: Optical microscopy image of Cr2O3 micro-structure device integrated on the micro-coil of the non-superconducting omega-shaped planar micro resonator.

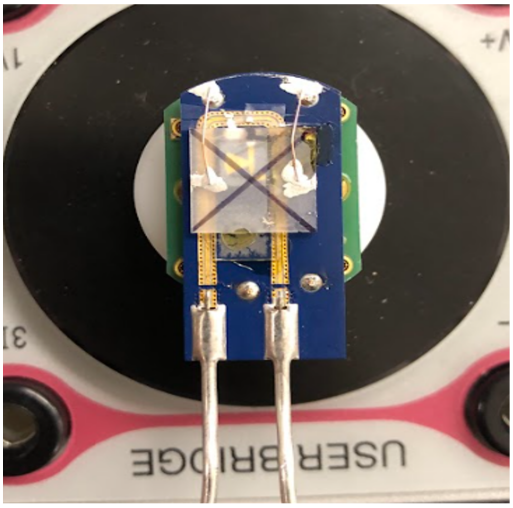

Figure 6.8: Integrated Cr2O3/Pt micro-structure device and non-superconducting omega-shaped planar micro-resonator sitting on a sample holder and ready for microwave spectroscopy measurement. The copper wire on the top is for electrical detection and spin biasing purpose.

and the coplanar waveguide assembly. The coplanar waveguide is electrically connected to the omega shaped planar micro-resonator. The microwave traveling in the planar micro-resonator creates the Oersted field encircling the propagation direction of the wave. The Oersted field excites the spins in Cr2O3. This resonance excitation leads to resistance oscillations due to the magnetoresistance effect that is detected via lock-in amplifier. The lock-in amplifier is referenced with the internal square wave of 400 Hz microwave pulse modulation frequency.

We sweep the magnetic field from 4.5 T to 7.5 T in both forward and reverse directions. Figure 6.9 below is the result of the microwave spectroscopy performed at 5.86 GHz and 100 times spectral averaged data for the forward (from 4.5 T to 7.5 T) and reverse (from 7.5 T to 4.5 T) directions. The resonance signal is not clearly visible. It is expected to be in between 5 T to 6 T at 30 K based on the frequency vs magnetic field relation from the experiment performed in Cr2O3 in the previous chapter. However, the hysteretic behavior is realized as we sweep the fields in different direction. Figure 6.10 is the corresponding Cr2O3/Pt microwave spectroscopy measurement for 7 GHz performed at 50 K for the broadband coplanar waveguide where we have observed only a slight hysteretic behavior.

Comparing the results in both cases: with the omega shaped planar micro-resonator and broadband coplanar resonator; the resonance signal is almost invisible in both cases. The misalignment in the c-axis and the external magnetic field direction leads to a very weak or no signal at lower frequencies zone. However, in both cases the hysteretic be-

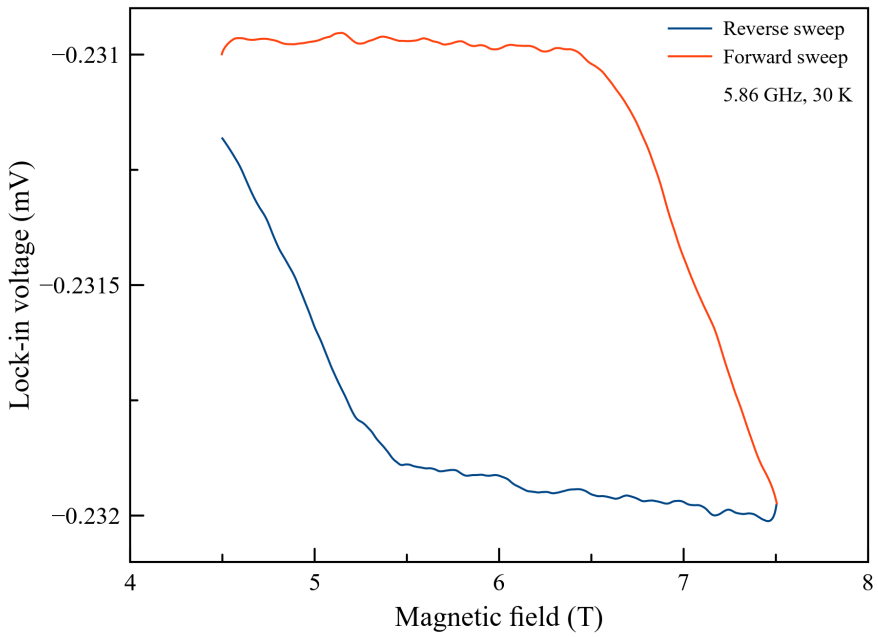

Figure 6.9: Microwave spectroscopy measurement of Cr2O3/Pt on a omega shaped planar micro-resonator performed at 30 K. The red curve is the data when the magnetic field is swept from 4.5 T to 7.5 T. The blue curve is the data when the magnetic field is swept from 7.5 T to 4.5 T.

havior is present. The hysteretic behavior of the omega shaped planar micro-resonator is substantially larger versus the broadband coplanar resonator.

6.6 Summary and outlook

Antiferromagnetic dynamics on thin films is more difficult compared to the bulk dynamics. As a parallel approach to increase the inductive detection capabilities for antiferromagnetic materials, we performed a preliminary study in the omega shaped planar micro-resonator.

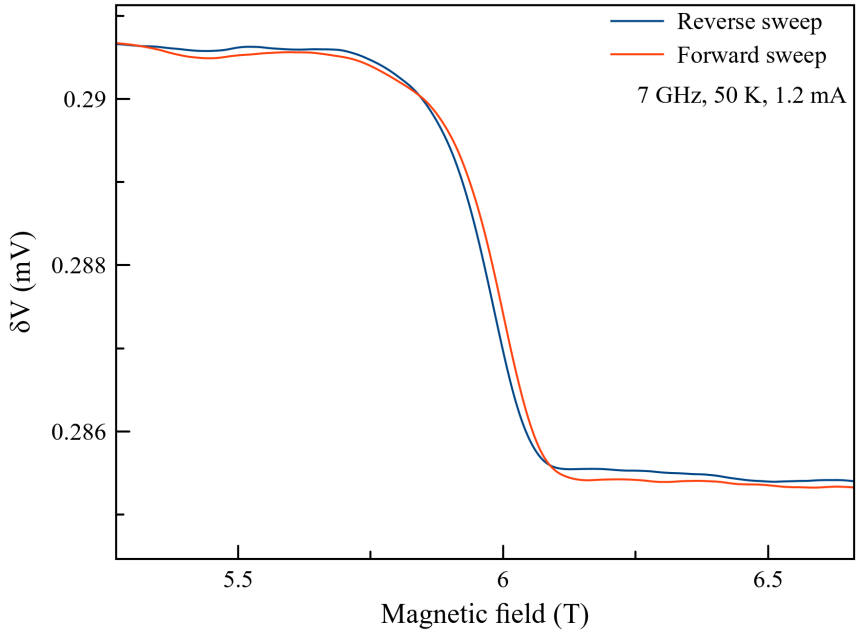

Figure 6.10: Microwave spectroscopy measurement of Cr2O3/Pt on a broadband coplanar waveguide (CPW) resonator performed at 50 K. The red curve is the data when the magnetic field is swept from 4.5 T to 7.5 T. The blue curve is the data when the magnetic field is swept from 7.5 T to 4.5 T.

We successfully fabricated the Cr2O3 micro-structure onto the sapphire substrate using the focused ion beam technique. We also implemented the electrical circuitry for electrical detection and spin biasing. We fabricated micro-resonator device using photolithography. We had to put an immense effort in order to align and integrate the micro-structure Cr2O3 device onto the micro-resonator chip.

After successfully integrating the device and the resonator, we performed the microwave spectroscopy. The results from our microwave spectroscopy show some hysteretic behavior, but the resonance signal is not visible. Perhaps the signal is very weak. As per Cr2O3 frequency vs magnetic field results in the previous chapter, the resonance signal magnitude is much stronger and clearly visible in the frequency range of 19-25 GHz. We need

to fabricate the omega shaped planar micro-resonator that has eigen frequency in the above range such that the possibility of seeing the resonance signal in Cr2O3 increases. Upon successfully validating the proof of concept of integrated micro-structure antiferromagnet and omega shaped planar micro-resonator, we plan to use the superconducting planar resonator as the next step.

Chapter 7

Conclusion

In this dissertation, energy efficiency has been explored in ferromagnetic system. The established techniques and knowledge of ferromagnetic system are extended to antiferromagnetic systems.

Our research examined two magnet hybrid nano-structures, uncovering intricate interfacial coupling resulting in weakly hybridized magnon modes. We observed auto-oscillation phenomena in configurations where Nickel magnetization was oblique and YIG magnetization nearly saturated in the out-of-plane setting. We concluded that the auto-oscillation observed is driven mainly by spin Seebeck effect. Furthermore, a pronounced nonlinear frequency shift of auto-oscillation near zero field was observed that might hold a significance for potential applications in neuromorphic systems.

Due to resilience to external magnetic perturbations and high excitation frequency range, we dive deeper into studying the coherent spin dynamics within antiferromagnetic systems by utilizing the pre-established techniques and knowledge from ferromagnetic sys-

tems. Beginning with magnetoresistive detection of antiferromagnetic resonance (AFMR) in bulk Cr2O3 and Pt microstructure devices, we progressed to nanoscale systems. These efforts resulted in a successful electrical detection of antiferromagnetic resonance signals in nanocross device of size $200\,\text{nm} \times 200\,\text{nm}$. We also analyzed and explored the resonance signals at various angles between the microwave current flow and the c-axis of the device. Additionally, our exploration extended to bulk Fe2O3. We found that the microwave current perpendicular to the c-axis of the device has stronger signal than microwave current parallel to the c-axis. This may have suggested that the resonance signal may have been dominated by spin torque excitation rather than inductive or Oersted excitation.

Recognizing the challenges inherent in studying antiferromagnetic dynamics in thin films, we proposed an alternative detection methods, including an omega-shaped planar micro-resonator. Despite successful fabrication and integration efforts, microwave spectroscopy results showed limited visibility of resonance signals, possibly due to signal weakness. To address this, future endeavors will focus on optimizing resonator design to enhance signal detection, ultimately aiming to validate the integration of micro-structure antiferromagnets with planar resonators for advanced applications.

Bibliography

[1] Giovanni Finocchio, Massimiliano Di Ventra, Kerem Y Camsari, Karin Everschor-Sitte, Pedram Khalili Amiri, and Zhongming Zeng. The promise of spintronics for unconventional computing. *Journal of Magnetism and Magnetic Materials*, 521:167506, 2021.

[2] Abdulqader Mahmoud, Frederic Vanderveken, Florin Ciubotaru, Christoph Adelmann, Said Hamdioui, and Sorin Cotofana. Spin wave based approximate computing. *IEEE Transactions on Emerging Topics in Computing*, 10(4):1932–1940, 2021.

[3] Ryosho Nakane, Gouhei Tanaka, and Akira Hirose. Reservoir computing with spin waves excited in a garnet film. *IEEE Access*, 6:4462–4469, 2018. doi: 10.1109/ACCESS.2018.2794584.

[4] Tomohiro Taniguchi, Sumito Tsunegi, Shinji Miwa, Keisuke Fujii, Hitoshi Kubota, and Kohei Nakajima. Reservoir computing based on spintronics technology. *Reservoir Computing: Theory, Physical Implementations, and Applications*, pages 331–360, 2021.

[5] Taro Kanao, Hirofumi Suto, Koichi Mizushima, Hayato Goto, Tetsufumi Tanamoto, and Tazumi Nagasawa. Reservoir computing on spin-torque oscillator array. *Phys. Rev. Appl.*, 12:024052, Aug 2019. doi: 10.1103/PhysRevApplied.12.024052. URL `https://link.aps.org/doi/10.1103/PhysRevApplied.12.024052`.

[6] Mrigank Sharad, Charles Augustine, Georgios Panagopoulos, and Kaushik Roy. Cognitive computing with spin-based neural networks. In *Proceedings of the 49th Annual Design Automation Conference*, pages 1262–1263, 2012.

[7] Hiroko Arai and Hiroshi Imamura. Neural-network computation using spin-wave-coupled spin-torque oscillators. *Phys. Rev. Appl.*, 10:024040, Aug 2018. doi: 10.1103/PhysRevApplied.10.024040. URL `https://link.aps.org/doi/10.1103/PhysRevApplied.10.024040`.

[8] Christoph Kloeffel and Daniel Loss. Prospects for spin-based quantum computing in quantum dots. *Annu. Rev. Condens. Matter Phys.*, 4(1):51–81, 2013.

[9] Veronica Cerletti, WA Coish, Oliver Gywat, and Daniel Loss. Recipes for spin-based quantum computing. *Nanotechnology*, 16(4):R27, 2005.

[10] Sadamichi Maekawa, Hiroto Adachi, Ken-ichi Uchida, Jun'ichi Ieda, and Eiji Saitoh. Spin current: Experimental and theoretical aspects. *Journal of the Physical Society of Japan*, 82(10):102002, 2013.

[11] Prashant Sharma. How to create a spin current. *Science*, 307(5709):531–533, 2005.

[12] Jairo Sinova, Sergio O. Valenzuela, J. Wunderlich, C. H. Back, and T. Jungwirth. Spin hall effects. *Rev. Mod. Phys.*, 87:1213–1260, Oct 2015. doi: 10.1103/RevModPhys.87.1213. URL `https://link.aps.org/doi/10.1103/RevModPhys.87.1213`.

[13] J. E. Hirsch. Spin hall effect. *Phys. Rev. Lett.*, 83:1834–1837, Aug 1999. doi: 10.1103/PhysRevLett.83.1834. URL `https://link.aps.org/doi/10.1103/PhysRevLett.83.1834`.

[14] Naoto Nagaosa, Jairo Sinova, Shigeki Onoda, A. H. MacDonald, and N. P. Ong. Anomalous hall effect. *Rev. Mod. Phys.*, 82:1539–1592, May 2010. doi: 10.1103/RevModPhys.82.1539. URL `https://link.aps.org/doi/10.1103/RevModPhys.82.1539`.

[15] T. Jungwirth, Qian Niu, and A. H. MacDonald. Anomalous hall effect in ferromagnetic semiconductors. *Phys. Rev. Lett.*, 88:207208, May 2002. doi: 10.1103/PhysRevLett.88.207208. URL `https://link.aps.org/doi/10.1103/PhysRevLett.88.207208`.

[16] Ph Nozieres and CJJPF Lewiner. A simple theory of the anomalous hall effect in semiconductors. *Journal de Physique*, 34(10):901–915, 1973.

[17] Jiang Xiao, Gerrit E. W. Bauer, Ken-chi Uchida, Eiji Saitoh, and Sadamichi Maekawa. Theory of magnon-driven spin seebeck effect. *Phys. Rev. B*, 81:214418, Jun 2010. doi: 10.1103/PhysRevB.81.214418. URL `https://link.aps.org/doi/10.1103/PhysRevB.81.214418`.

[18] Hiroto Adachi, Ken-ichi Uchida, Eiji Saitoh, and Sadamichi Maekawa. Theory of the spin seebeck effect. *Reports on Progress in Physics*, 76(3):036501, 2013.

[19] C. M. Jaworski, J. Yang, S. Mack, D. D. Awschalom, R. C. Myers, and J. P. Heremans. Spin-seebeck effect: A phonon driven spin distribution. *Phys. Rev. Lett.*, 106:186601, May 2011. doi: 10.1103/PhysRevLett.106.186601. URL https://link.aps.org/doi/10.1103/PhysRevLett.106.186601.

[20] B. F. Miao, S. Y. Huang, D. Qu, and C. L. Chien. Inverse spin hall effect in a ferromagnetic metal. *Phys. Rev. Lett.*, 111:066602, Aug 2013. doi: 10.1103/PhysRevLett.111.066602. URL https://link.aps.org/doi/10.1103/PhysRevLett.111.066602.

[21] C. Hahn, G. de Loubens, M. Viret, O. Klein, V. V. Naletov, and J. Ben Youssef. Detection of microwave spin pumping using the inverse spin hall effect. *Phys. Rev. Lett.*, 111:217204, Nov 2013. doi: 10.1103/PhysRevLett.111.217204. URL https://link.aps.org/doi/10.1103/PhysRevLett.111.217204.

[22] Kazuya Ando and Eiji Saitoh. Observation of the inverse spin hall effect in silicon. *Nature communications*, 3(1):629, 2012.

[23] H Weiss. Magnetoresistance. In *Semiconductors and Semimetals*, volume 1, pages 315–376. Elsevier, 1966.

[24] Kai Chen and Shufeng Zhang. Spin pumping in the presence of spin-orbit coupling. *Physical review letters*, 114(12):126602, 2015.

[25] M. Weiler, H. Huebl, F. S. Goerg, F. D. Czeschka, R. Gross, and S. T. B. Goennenwein. Spin pumping with coherent elastic waves. *Phys. Rev. Lett.*, 108:176601, Apr 2012. doi: 10.1103/PhysRevLett.108.176601. URL https://link.aps.org/doi/10.1103/PhysRevLett.108.176601.

[26] A Brataas, Yaroslav Tserkovnyak, GEW Bauer, and Paul J Kelly. Spin pumping and spin transfer. *Spin current*, 17:87–135, 2012.

[27] M. D. Stiles and A. Zangwill. Anatomy of spin-transfer torque. *Phys. Rev. B*, 66:014407, Jun 2002. doi: 10.1103/PhysRevB.66.014407. URL https://link.aps.org/doi/10.1103/PhysRevB.66.014407.

[28] Daniel C Ralph and Mark D Stiles. Spin transfer torques. *Journal of Magnetism and Magnetic Materials*, 320(7):1190–1216, 2008.

[29] Z. Li and S. Zhang. Magnetization dynamics with a spin-transfer torque. *Phys. Rev. B*, 68:024404, Jul 2003. doi: 10.1103/PhysRevB.68.024404. URL https://link.aps.

org/doi/10.1103/PhysRevB.68.024404.

[30] Stephen Blundell. *Magnetism in Condensed Matter*. Oxford University press, 2001.

[31] C. Zener and R. R. Heikes. Exchange interactions. *Rev. Mod. Phys.*, 25:191–198, Jan 1953. doi: 10.1103/RevModPhys.25.191.2. URL https://link.aps.org/doi/10.1103/RevModPhys.25.191.2.

[32] J. VAN KRANENDONK and J. H. VAN VLECK. Spin waves. *Rev. Mod. Phys.*, 30: 1–23, Jan 1958. doi: 10.1103/RevModPhys.30.1. URL https://link.aps.org/doi/10.1103/RevModPhys.30.1.

[33] Sergej O Demokritov. Magnons. *Topology in Magnetism*, pages 299–334, 2018.

[34] Andrii V Chumak, Vitaliy I Vasyuchka, Alexander A Serga, and Burkard Hillebrands. Magnon spintronics. *Nature physics*, 11(6):453–461, 2015.

[35] Sebastian Neusser and Dirk Grundler. Magnonics: Spin waves on the nanoscale. *Advanced materials*, 21(28):2927–2932, 2009.

[36] Igor Žutić, Jaroslav Fabian, and S. Das Sarma. Spintronics: Fundamentals and applications. *Rev. Mod. Phys.*, 76:323–410, Apr 2004. doi: 10.1103/RevModPhys.76.323. URL https://link.aps.org/doi/10.1103/RevModPhys.76.323.

[37] Eric Montoya, Thomas Sebastian, Helmut Schultheiss, Bret Heinrich, Robert E Camley, and Zbigniew Celinski. Magnetization dynamics. In *Handbook of Surface Science*, volume 5, pages 113–167. Elsevier, 2015.

[38] Andrei Slavin and Vasil Tiberkevich. Nonlinear auto-oscillator theory of microwave generation by spin-polarized current. *IEEE Transactions on Magnetics*, 45(4):1875–1918, 2009. doi: 10.1109/TMAG.2008.2009935.

[39] M Lakshmanan. The fascinating world of the landau–lifshitz–gilbert equation: an overview. *Philosophical Transactions of the Royal Society A: Mathematical, Physical and Engineering Sciences*, 369(1939):1280–1300, 2011.

[40] Augusto Visintin. On landau-lifshitz'equations for ferromagnetism. *Japan journal of applied mathematics*, 2:69–84, 1985.

[41] Unai Atxitia, Denise Hinzke, and Ulrich Nowak. Fundamentals and applications of the landau–lifshitz–bloch equation. *Journal of Physics D: Applied Physics*, 50(3):033003, 2016.

[42] J.C. Slonczewski. Current-driven excitation of magnetic multilayers. *Journal of Magnetism and Magnetic Materials*, 159(1):L1–L7, 1996. ISSN 0304-8853. doi: https://doi.org/10.1016/0304-8853(96)00062-5. URL https://www.sciencedirect.com/science/article/pii/0304885396000625.

[43] S Il Kiselev, JC Sankey, IN Krivorotov, NC Emley, RJ Schoelkopf, RA Buhrman, and DC Ralph. Microwave oscillations of a nanomagnet driven by a spin-polarized current. *nature*, 425(6956):380–383, 2003.

[44] Dmytro A. Bozhko, Alexander A. Serga, Peter Clausen, Vitaliy I. Vasyuchka, Frank Heussner, Gennadii A. Melkov, Anna Pomyalov, Victor S. L'vov, and Burkard Hillebrands. Supercurrent in a room-temperature bose–einstein magnon condensate. *Nature Physics*, 12:1057 – 1062, 2015. URL https://api.semanticscholar.org/CorpusID:118497976.

[45] Fengyuan Yang and P Chris Hammel. Fmr-driven spin pumping in y3fe5o12-based structures. *Journal of Physics D: Applied Physics*, 51(25):253001, may 2018. doi: 10.1088/1361-6463/aac249. URL https://dx.doi.org/10.1088/1361-6463/aac249.

[46] Can Onur Avci, Andy Quindeau, Chi-Feng Pai, Maxwell Mann, Lucas Caretta, Astera S Tang, Mehmet C Onbasli, Caroline A Ross, and Geoffrey SD Beach. Current-induced switching in a magnetic insulator. *Nature materials*, 16(3):309–314, 2017.

[47] Editorial. Memory with a spin. *Nature Nanotechnology*, 2015. URL https://doi.org/10.1038/nnano.2015.50.

[48] Andrew D Kent and Daniel C Worledge. A new spin on magnetic memories. *Nature nanotechnology*, 10(3):187–191, 2015.

[49] H-S Philip Wong and Sayeef Salahuddin. Memory leads the way to better computing. *Nature nanotechnology*, 10(3):191–194, 2015.

[50] Joo-Von Kim. Chapter four - spin-torque oscillators. volume 63 of *Solid State Physics*, pages 217–294. Academic Press, 2012. doi: https://doi.org/10.1016/B978-0-12-397028-2.00004-7. URL https://www.sciencedirect.com/science/article/pii/B9780123970282000047.

[51] Zheng Duan, Andrew Smith, Liu Yang, Brian Youngblood, Jürgen Lindner, Vladislav E. Demidov, Sergej O. Demokritov, and Ilya N. Krivorotov. Nanowire spin torque oscillator driven by spin orbit torques. *Nature Communications*, 2014. URL `https://doi.org/10.1038/ncomms6616`.

[52] Miguel Romera, Philippe Talatchian, Sumito Tsunegi, Flavio Abreu Araujo, Vincent Cros, Paolo Bortolotti, Juan Trastoy, Kay Yakushiji, Akio Fukushima, Hitoshi Kubota, Shinji Yuasa, Maxence Ernoult, Damir Vodenicarevic, Tifenn Hirtzlin, Nicolas Locatelli, Damien Querlioz, and Julie Grollier. Vowel recognition with four coupled spin-torque nano-oscillators. *Nature*, 2018.

[53] Kartik Adhikari, Sourav Sahoo, Amrit Kumar Mondal, Yoshichika Otani, and Anjan Barman. Large nonlinear ferromagnetic resonance shift and strong magnon-magnon coupling in n i 80 f e 20 nanocross array. *Physical Review B*, 101(5):054406, 2020.

[54] M. Evelt, C. Safranski, Mohammed Aldosary, V. E. Demidov, I. Barsukov, A. P. Nosov, A. B. Rinkevich, K. Sobotkiewich, Xiaoqin Li, Jing Shi, I. N. Krivorotov, and S. O. Demokritov. Spin hall-induced auto-oscillations in ultrathin yig grown on pt. *Scientific Reports*, 2018. URL `https://www.nature.com/articles/s41598-018-19606-5`.

[55] C. Safranski, I. Barsukov, H. K. Lee, T. Schneider, A. A. Jara, A. Smith, H. Chang, J. andTserkovnyak Y. Lenz, K. andLindner, M. Wu, and I. N. Krivorotov. Spin caloritronic nano-oscillator. *Nature Communications*, 2017. URL `https://www.nature.com/articles/s41467-017-00184-5`.

[56] Bassim Arkook, Christopher Safranski, Rodolfo Rodriguez, Ilya N. Krivorotov, Tobias Schneider, Kilian Lenz, Jürgen Lindner, Houchen Chang, Mingzhong Wu, Yaroslav Tserkovnyak, and Igor Barsukov. Thermally driven two-magnet nano-oscillator with large spin-charge conversion, 2019.

[57] Georg Schmidt, Christoph Hauser, Philip Trempler, Maximilian Paleschke, and Evangelos Th Papaioannou. Ultra thin films of yttrium iron garnet with very low damping: A review. *physica status solidi (b)*, 257(7):1900644, 2020.

[58] Houchen Chang, Peng Li, Wei Zhang, Tao Liu, Axel Hoffmann, Longjiang Deng, and Mingzhong Wu. Nanometer-thick yttrium iron garnet films with extremely low damping. *IEEE Magnetics Letters*, 5:1–4, 2014.

[59] Christian Hahn, VV Naletov, Gregoire de Loubens, Olivier Klein, O d'Allivy Kelly, Abdelmadjid Anane, Rozenn Bernard, Eric Jacquet, Paolo Bortolotti, Vincent Cros,

et al. Measurement of the intrinsic damping constant in individual nanodisks of y3fe5o12 and y3fe5o12| pt. *Applied Physics Letters*, 104(15), 2014.

[60] CL Jermain, SV Aradhya, ND Reynolds, RA Buhrman, JT Brangham, MR Page, PC Hammel, FY Yang, and DC Ralph. Increased low-temperature damping in yttrium iron garnet thin films. *Physical Review B*, 95(17):174411, 2017.

[61] PC Dorsey, SE Bushnell, RG Seed, and C Vittoria. Epitaxial yttrium iron garnet films grown by pulsed laser deposition. *Journal of Applied Physics*, 74(2):1242–1246, 1993.

[62] Chi Tang, Mohammed Aldosary, Zilong Jiang, Houchen Chang, Benjamin Madon, Kyle Chan, Mingzhong Wu, Javier E Garay, and Jing Shi. Exquisite growth control and magnetic properties of yttrium iron garnet thin films. *Applied Physics Letters*, 108(10), 2016.

[63] S Satapathy, PK Siwach, HK Singh, RP Pant, and KK Maurya. Structural and magnetic properties of yig thin films deposited by pulsed laser deposition and rf magnetron sputtering technique. *Physica Scripta*, 98(10):105508, 2023.

[64] Tao Liu, Houchen Chang, Vincent Vlaminck, Yiyan Sun, Michael Kabatek, Axel Hoffmann, Longjiang Deng, and Mingzhong Wu. Ferromagnetic resonance of sputtered yttrium iron garnet nanometer films. *Journal of Applied Physics*, 115(17):17A501, 01 2014. ISSN 0021-8979. doi: 10.1063/1.4852135. URL `https://doi.org/10.1063/1.4852135`.

[65] William Thomson. Xix. on the electro-dynamic qualities of metals:—effects of magnetization on the electric conductivity of nickel and of iron. *Proceedings of the Royal Society of London*, 1857.

[66] HW Schumacher, S Serrano-Guisan, Karsten Rott, and Günter Reiss. Ultrafast magnetization dynamics probed by anisotropic magnetoresistance. *Applied physics letters*, 90(4), 2007.

[67] T Wren and O Kazakova. Anisotropic magnetoresistance effect in sub-micron nickel disks. *Journal of Applied Physics*, 117(17), 2015.

[68] J-E Wegrowe, SE Gilbert, D Kelly, B Doudin, and J-P Ansermet. Anisotropic magnetoresistance as a probe of magnetization reversal in individual nono-sized nickel wires. *IEEE transactions on magnetics*, 34(4):903–905, 1998.

[69] Arne Vansteenkiste, Jonathan Leliaert, Mykola Dvornik, Mathias Helsen, Felipe Garcia-Sanchez, and Bartel Van Waeyenberge. The design and verification of mumax3. *AIP Adv.*, 4(10):107133, 2014. doi: 10.1063/1.4899186.

[70] Michael Schreier, Takahiro Chiba, Arthur Niedermayr, Johannes Lotze, Hans Huebl, Stephan Geprägs, Saburo Takahashi, Gerrit EW Bauer, Rudolf Gross, and Sebastian TB Goennenwein. Current-induced spin torque resonance of a magnetic insulator. *Physical Review B*, 92(14):144411, 2015.

[71] Luqiao Liu, Takahiro Moriyama, D. C. Ralph, and R. A. Buhrman. Spin-torque ferromagnetic resonance induced by the spin hall effect. *Phys. Rev. Lett.*, 106:036601, Jan 2011. doi: 10.1103/PhysRevLett.106.036601. URL `https://link.aps.org/doi/10.1103/PhysRevLett.106.036601`.

[72] J. C. Sankey, P. M. Braganca, A. G. F. Garcia, I. N. Krivorotov, R. A. Buhrman, and D. C. Ralph. Spin-transfer-driven ferromagnetic resonance of individual nanomagnets. *Phys. Rev. Lett.*, 96:227601, Jun 2006. doi: 10.1103/PhysRevLett.96.227601. URL `https://link.aps.org/doi/10.1103/PhysRevLett.96.227601`.

[73] Christopher Safranski. *Spin Torque Oscillators*. PhD thesis, University of California, Irvine, 2018. URL `https://escholarship.org/uc/item/8803x2g4`.

[74] AM Gonçalves, I Barsukov, Y-J Chen, L Yang, JA Katine, and IN Krivorotov. Spin torque ferromagnetic resonance with magnetic field modulation. *Applied Physics Letters*, 103(17), 2013.

[75] SM Rezende and RL Rodríguez-Suárez. Theory for the spin caloritronic nano-oscillator. *Physical Review B*, 105(14):144429, 2022.

[76] Jen-Ru Chen, Andrew Smith, Eric A Montoya, Jia G Lu, and Ilya N Krivorotov. Spin–orbit torque nano-oscillator with giant magnetoresistance readout. *Communications Physics*, 3(1):187, 2020.

[77] HC Tong, C Qian, L Miloslavsky, S Funada, X Shi, F Liu, and S Dey. The spin flop of synthetic antiferromagnetic films. *Journal of Applied Physics*, 87(9):5055–5057, 2000.

[78] Cheng P Wen. Coplanar waveguide: A surface strip transmission line suitable for nonreciprocal gyromagnetic device applications. *IEEE Transactions on Microwave Theory and Techniques*, 17(12):1087–1090, 1969.

[79] Edward M Purcell. Helmholtz coils revisited. *American Journal of Physics*, 57(1): 18–22, 1989.

[80] Charles Kittel. On the theory of ferromagnetic resonance absorption. *Phys. Rev.*, 73:155–161, Jan 1948. doi: 10.1103/PhysRev.73.155. URL `https://link.aps.org/doi/10.1103/PhysRev.73.155`.

[81] Editorial. Quantum possibilities. *Nature Physics*, 2018.

[82] Davide Castelvecchi. Quantum computers ready to leap out of the lab in 2017. *Nature*, 541(7635), 2017.

[83] Vincent Baltz, Aurelien Manchon, M Tsoi, Takahiro Moriyama, T Ono, and Y Tserkovnyak. Antiferromagnetic spintronics. *Reviews of Modern Physics*, 90(1): 015005, 2018.

[84] Tomas Jungwirth, X Marti, P Wadley, and J Wunderlich. Antiferromagnetic spintronics. *Nature nanotechnology*, 11(3):231–241, 2016.

[85] Joseph Sklenar, Wei Zhang, Matthias B Jungfleisch, Wanjun Jiang, Hilal Saglam, John E Pearson, John B Ketterson, and Axel Hoffmann. Spin hall effects in metallic antiferromagnets–perspectives for future spin-orbitronics. *AIP Advances*, 6(5), 2016.

[86] AV Kimel, BA Ivanov, RV Pisarev, PA Usachev, A Kirilyuk, and Th Rasing. Inertia-driven spin switching in antiferromagnets. *Nature Physics*, 5(10):727–731, 2009.

[87] Shohei Hayashida, Oksana Zaharko, Nobuyuki Kurita, Hidekazu Tanaka, Masato Hagihala, Minoru Soda, Shinichi Itoh, Yoshiya Uwatoko, and Takatsugu Masuda. Pressure-induced quantum phase transition in the quantum antiferromagnet csfecl 3. *Physical Review B*, 97(14):140405, 2018.

[88] Junxue Li, C Blake Wilson, Ran Cheng, Mark Lohmann, Marzieh Kavand, Wei Yuan, Mohammed Aldosary, Nikolay Agladze, Peng Wei, Mark S Sherwin, and Jing Shi. Spin current from sub-terahertz-generated antiferromagnetic magnons. *Nature*, 578(7793): 70–74, 2020.

[89] Priyanka Vaidya, Sophie A Morley, Johan van Tol, Yan Liu, Ran Cheng, Arne Brataas, David Lederman, and Enrique Del Barco. Subterahertz spin pumping from an insulating antiferromagnet. *Science*, 368(6487):160–165, 2020.

[90] Priyanka Vaidya. *Sub-Terahertz Spin Pumpping from an Insulating Antiferromagnet*. PhD thesis, University of Central Florida, 2019. URL https://stars.library.ucf.edu/etd/6757/.

[91] LM Corliss, JM Hastings, R Nathans, and G Shirane. Magnetic structure of cr2o3. *Journal of Applied Physics*, 36(3):1099–1100, 1965.

[92] Siqi Shi, Aleksander L Wysocki, and Kirill D Belashchenko. Magnetism of chromia from first-principles calculations. *Physical Review B*, 79(10):104404, 2009.

[93] Jason A Cline, Angeliki A Rigos, and Tomás A Arias. Ab initio study of magnetic structure and chemical reactivity of cr2o3 and its (0001) surface. *The Journal of Physical Chemistry B*, 104(26):6195–6201, 2000.

[94] Sverre A. Gulbrandsen, Camilla Espedal, and Arne Brataas. Spin hall effect in antiferromagnets. *Phys. Rev. B*, 101:184411, May 2020. doi: 10.1103/PhysRevB.101.184411. URL https://link.aps.org/doi/10.1103/PhysRevB.101.184411.

[95] Hongming Weng, Xi Dai, and Zhong Fang. From anomalous hall effect to the quantum anomalous hall effect. *arXiv: Materials Science*, 2015. URL https://api.semanticscholar.org/CorpusID:119248891.

[96] Physical Properties of Sapphire. URL https://www.shinkosha.com/english/techinfo/feature/physical-properties-of-sapphire/. SHINKOSHA CO., LTD.

[97] Yan-Ting Chen, Saburo Takahashi, Hiroyasu Nakayama, Matthias Althammer, Sebastian T. B. Goennenwein, Eiji Saitoh, and Gerrit E. W. Bauer. Theory of spin hall magnetoresistance. *Phys. Rev. B*, 87:144411, Apr 2013. doi: 10.1103/PhysRevB.87.144411. URL https://link.aps.org/doi/10.1103/PhysRevB.87.144411.

[98] Johanna Fischer, Olena Gomonay, Richard Schlitz, Kathrin Ganzhorn, Nynke Vlietstra, Matthias Althammer, Hans Huebl, Matthias Opel, Rudolf Gross, Sebastian T. B. Goennenwein, and Stephan Geprägs. Spin hall magnetoresistance in antiferromagnet/heavy-metal heterostructures. *Phys. Rev. B*, 97:014417, Jan 2018. doi: 10.1103/PhysRevB.97.014417. URL https://link.aps.org/doi/10.1103/PhysRevB.97.014417.

[99] Richard Schlitz, Tobias Kosub, Andy Thomas, Savio Fabretti, Kornelius Nielsch, Denys Makarov, and Sebastian TB Goennenwein. Evolution of the spin hall mag-

netoresistance in cr2o3/pt bilayers close to the néel temperature. *Applied Physics Letters*, 112(13), 2018.

[100] Rodolfo Rodriguez, Shirash Regmi, Hantao Zhang, Wei Yuan, Pavlo Makushko, Eric A. Montoya, Ihor Veremchuk, René Hübner, Denys Makarov, Jing Shi, Ran Cheng, and Igor Barsukov. Robust spin injection via thermal magnon pumping in antiferromagnet/ferromagnet hybrid systems. *Phys. Rev. Res.*, 4:033139, Aug 2022. doi: 10.1103/PhysRevResearch.4.033139. URL `https://link.aps.org/doi/10.1103/PhysRevResearch.4.033139`.

[101] Ran Cheng, Jiang Xiao, Qian Niu, and Arne Brataas. Spin pumping and spin-transfer torques in antiferromagnets. *Physical review letters*, 113(5):057601, 2014.

[102] Øyvind Johansen, Hans Skarsvåg, and Arne Brataas. Spin-transfer antiferromagnetic resonance. *Physical Review B*, 97(5):054423, 2018.

[103] Sergio M Rezende, Antonio Azevedo, and Roberto L Rodríguez-Suárez. Introduction to antiferromagnetic magnons. *Journal of Applied Physics*, 126(15), 2019.

[104] KL Dudko, VV Eremenko, and LM Semenenko. Magnetostriction of antiferromagnetic cr2o3 in strong magnetic fields. *physica status solidi (b)*, 43(2):471–477, 1971.

[105] M Bialek, J Zhang, H Yu, and J-Ph Ansermet. Antiferromagnetic resonance in a-fe2o3 up to its neel temperature. *Applied Physics Letters*, 121(3):032401, 2022.

[106] QA Pankhurst, CE Johnson, and MF Thomas. A mossbauer study of magnetic phase transitions in alpha-fe2o3 crystals. *Journal of Physics C: Solid State Physics*, 19(35): 7081, 1986.

[107] PR Elliston and GJ Troup. Some antiferromagnetic resonance measurements in α-fe2o3. *Journal of Physics C: Solid State Physics*, 1(1):169, 1968.

[108] Danrong Xiong, Yuhao Jiang, Kewen Shi, Ao Du, Yuxuan Yao, Zongxia Guo, Daoqian Zhu, Kaihua Cao, Shouzhong Peng, Wenlong Cai, et al. Antiferromagnetic spintronics: An overview and outlook. *Fundamental Research*, 2(4):522–534, 2022.

[109] EV Gomonay and VM Loktev. Spintronics of antiferromagnetic systems. *Low Temperature Physics*, 40(1):17–35, 2014.

[110] R Narkowicz, D Suter, and R Stonies. Planar microresonators for epr experiments. *Journal of Magnetic Resonance*, 175(2):275–284, 2005.

[111] Ryszard Narkowicz and Dieter Suter. Tuner and radiation shield for planar electron paramagnetic resonance microresonators. *Review of Scientific Instruments*, 86(2), 2015.

[112] R Narkowicz, D Suter, and I Niemeyer. Scaling of sensitivity and efficiency in planar microresonators for electron spin resonance. *Review of Scientific Instruments*, 79(8), 2008.

[113] Ygal Twig, Ekaterina Suhovoy, and Aharon Blank. Sensitive surface loop-gap microresonators for electron spin resonance. *Review of Scientific Instruments*, 81(10), 2010.

[114] Dany Lachance-Quirion, Yutaka Tabuchi, Arnaud Gloppe, Koji Usami, and Yasunobu Nakamura. Hybrid quantum systems based on magnonics. *Applied Physics Express*, 12(7):070101, 2019.

[115] AA Clerk, KW Lehnert, P Bertet, JR Petta, and Y Nakamura. Hybrid quantum systems with circuit quantum electrodynamics. *Nature Physics*, 16(3):257–267, 2020.

[116] Yun Zhang and Xiaojie Xu. Yttrium barium copper oxide superconducting transition temperature modeling through gaussian process regression. *Computational Materials Science*, 179:109583, 2020.